UNIVERSITY COLLEGE LONDON

Department of Physics & Astronomy

Understanding the distribution of gas in the Universe

Teresita Suárez Noguez

Thesis presented for the Degree of
Doctor of Philosophy

Supervisors:
Dr Andrew Pontzen
Prof. Hiranya V. Peiris

Examiners:
Prof. Richard Ellis
Dr James Bolton

January 25, 2018

Declaration

I, Teresita Suárez Noguez , declare that the thesis entitled *Understanding the distribution of gas in the Universe* and the work presented in the thesis are both my own, and have been generated by me as the result of my own original research.
I confirm the thesis is based on work done by myself jointly with others, I have made clear exactly what was done by others and what I have contributed myself.
This work has not been submitted for any other degree at UCL or any other University.

London, January 25, 2018

Teresita Suárez Noguez

Understanding the distribution of gas in the Universe

Teresita Suárez Noguez

Abstract

The distribution of gas in the Universe can be observed in absorption in the spectra of quasars. However, interpreting the spectra requires comparison to physical models which map the distribution, temperatures and ionisation states of the gas.

First, I focused on understanding the presence of outflowing cold gas around galaxies. I performed numerical simulations to study how outflows, launched from a central galaxy undergoing starbursts, affect the circumgalactic medium. I model an outflow as a rapidly moving bubble of gas above the disk and analyse its evolution. I sampled a distribution of parameters with a grid of two-dimensional hydrodynamical simulations –with and without– radiative cooling, assuming primordial gas composition. The amount of the cool gas fraction depends strongly on the "burstiness" of energy injection; stronger bursts typically lead to a larger fraction of cool gas forming in the outflow. This suggests cool gas is formed in the outflow itself rather than entrained from the interstellar medium, emphasising the importance of cooling.

Secondly, I turn to the lower density gas known as the Lyman-α forest. This is formed from a trace of HI in a predominantly photoionised intergalactic medium. Existing radiative transfer models show that large-scale ionisation rate fluctuations can have an observable impact on the forest. I extend these models to include beaming of the quasar population. This has two effects: the physical number density of ionising sources is enhanced relative to observations and; the radiative transfer equation is altered. I studied the statistical properties of the resulting ionisation rate and neutral hydrogen density fields at redshift $z \sim$2.3. I find that both effects from beaming partially cancel each other. On very large scales ($k < 0.01$ h/Mpc) the source density renormalisation dominates; it can reduce, by an order of magnitude, the contribution of ionising shot-noise to the intergalactic HI power spectrum.

Acknowledgements

I want to thank Andrew Pontzen, my supervisor, for making me part of the two challenging projects I developed during my PhD. I greatly enjoyed collaborating with you. Thanks for your guidance, encouragement, and the many insightful scientific discussions that made this stage of my academic experience very enjoyable.

Thanks to Hiranya Peiris, my second supervisor, for plenty of useful discussions and thorough proof-reading of this thesis. To whom I'm also indebted for her strong support and advice during my PhD.

I want to specially thank Juan Hernandez for your unconditional support, extended meaningful conversations and for all the scientific/programming consultations, including proof-reading this thesis. Thanks to Alex Merson, Boris Leistedt, Will Hartley, Jonathan Braden, Daniela Saadeh, Koki Kakiichi, Martin Rey and Chris Wallis; for the many academic and non-academic exchange of ideas, for their help proof-reading fragments of this thesis and for their invaluable friendship.

I am grateful to David Weinberg, Paul Martini and Suk Sien Tie for useful discussions on possible applications of my models; and thanks to both Ohio State University and University College London for funding this collaboration.

I would like to acknowledge funding by Consejo Nacional de Ciencia y Tecnologa (CONACyT) and University College London.

Finally, I want to thank my family for their encouragement all my life and for teaching me that being a woman has no limitations. Also, thanks to Elena Provaggi, Alex Chivu and Carolina Ramos, for their support during my years living in London and for their true friendship.

Contents

List of Figures

List of Tables

Chapter 1 | *Introduction*

1.1 The Universe

Cosmology seeks to understand the origin, evolution and structure of the Universe, and provides a framework that sets the initial conditions for galaxy formation and evolution. The Universe, to a very good approximation, is homogeneous on large scales (where "large" means distances $\gtrsim 100$ Mpc), while being very far from homogeneous on small scales. The assumption that the Universe is homogeneous and isotropic on large scales is known as the "cosmological principle". This assumption is supported by observations of the *cosmic microwave background* (CMB) and the spatial distribution of galaxies on large scales. Isotropy and homogeneity provide us with basic statistical properties enforcing the assumption that physical properties (like density and pressure) must be the same at any point. This assumption is crucial for studies of the global properties of the Universe, because it means that the physics we know are valid on any small volume over the Universe.

I begin by providing some useful definitions. The scale factor $a(t)$ describes changes in the distance between any two points fixed in an expanding universe. In particular, two particles that move apart from each other in a homogeneous universe have a physical distance $r(t) = a(t)x$, where x is a fixed comoving distance. The Hubble constant $H_0 \equiv \dot{a}_0/a_0$, in which $a_0 \equiv a(t_0)$ is the scale factor evaluated at the present time t_0, and $\dot{a}_0$ represents its evolution in time. The Hubble parameter $h \cong H_0/(70\ \mathrm{km\ s^{-1}\ Mpc^{-1}})$.

The redshift parameter measures the change in the wavelength (λ) by a photon emitted at early times t. It will be observed today with a different wavelength (λ_{obs}) following

$$z \equiv \frac{\lambda_{\mathrm{obs}}}{\lambda} - 1 = \frac{a_0}{a(t)} - 1. \tag{1.1}$$

This relationship between redshift z and the scalefactor $a(t)$ arises because the wavelength of a photon is stretched by the expansion of the universe as it travels through, and constitutes a crucial observational tool.

1.1.1 Composition: mass and energy content

In modern cosmology the universe is thought to be composed mainly of baryons, dark matter and dark energy (Shull et al., 2012). Although the nature of dark matter and dark energy are still unknown there is observational evidence (summarised below) that makes us believe they are responsible for more than 95 % of the energy density in the Universe (Spergel et al., 2007; Copi et al., 1995b).

Einstein's general relativity predicts that the shape of the Universe depends on its content. In particular, if the matter and radiation density ρ equals the critical density $\rho_{\rm crit}$, which is the present-day density, the Universe will be spatially flat (Sec. 1.1.2 on FRW metric). Observations can tell us whether the Universe is spatially flat and also probe the density of its contents directly. The best constraints typically come from the CMB power spectrum and show that the cosmological parameters for a flat Universe are (Planck Collaboration et al., 2016b):

$$\begin{aligned} \Omega_0 &= 1.0 \pm 0.02; \\ \Omega_b h^2 &= 0.02222 \pm 0.00023; \\ \Omega_c h^2 &= 0.1197 \pm 0.0022; \\ \Omega_m &= 0.315 \pm 0.013; \\ h &= 0.6731 \pm 0.0096; \end{aligned} \tag{1.2}$$

Here, Ω_0 is the total density parameter, $\Omega_x = \rho_x/\rho_{\rm crit}$ corresponds to the fraction of the Universe's density provided by ($x = c$) dark matter, ($x = b$) baryons and ($x = m$) total matter respectively. We therefore see that current observations favour a flat Universe, i.e. with the critical density. I now briefly summarise the properties of the different components listed above.

1. **Baryons**

The visible Universe is made up by protons, neutrons and electrons; commonly referred to as baryonic matter[1]. Since stars are made of baryons, one method to obtain an estimate of the mass density of baryonic matter would be via the mean luminosity density of stars in galaxies. In total, however stars only account for $\sim$10% of all baryons (Blumenthal et al., 1986). In combination with estimates of cold and hot gas, the total

[1] Electrons are not baryons but leptons. However, when talking about baryonic matter it is standard practice to include electrons.

baryonic mass at lower redshift still only accounts for $\lesssim 50\%$ of the baryonic mass inferred from the CMB (McCarthy et al., 2007; Giodini et al., 2009). This would suggest that half of the expected baryonic mass at low redshift is unaccounted observationally, commonly referred to as the *missing baryon problem*. Unfortunately, detecting the intergalactic medium (IGM) at low redshift is highly challenging. Estimates of the IGM baryon content using first HI absorbers (also known as the Ly-α forest) are able to account for a fraction of baryons of $\sim 30\%$. An additional 8% of the baryons reside in the warm-hot intergalactic medium (WHIM) inferred by non-primordial elements (Bregman, 2007), via absorbers such as OVI (Danforth & Shull, 2008). A vast reservoir of hot gas ($T > 10^6$ K) in the IGM is inaccessible through far-ultraviolet absorption lines (Cen & Ostriker, 1999; Shull, 2003). These baryons are only observable in the X-ray range and detecting them remain a challenge for future sensitive X-ray spectrographs. However, new techniques such as the surface brightness of the Sunyaev-Zel'dovich (SZ) effect are promising ways to address this problem. At high redshifts ($z \lesssim 6$), most of the baryons are located in the IGM (Kim et al., 1997), being highly ionised by an ultraviolet background produced by galaxies and quasars. Observations of the Lyα forest at high redshifts are consistent with those of the CMB e.g. average hydrogen densities observed in the absorption spectra of quasars at z$\sim$3 (e.g., Hu & Dodelson, 2002).

2. **Dark matter**

Mass density in the Universe must be observed indirectly because some components do not emit radiation, with the gravitational force providing the only interaction that can be detected (Turner, 1991; Faber & Gallagher, 1979; Bahcall et al., 1999; Navarro et al., 1996). The estimation of the total matter density from the CMB is now the strongest evidence for the existence of a form of non-baryonic matter (Hu et al., 1999; Turner, 2002; Spergel et al., 2007). This invisible matter dominates the total mass density $\Omega_{m,0}$ e.g. galaxy rotation curves (Rubin et al., 1982), weak lensing (Clowe et al., 2006), the "bullet cluster" (Clowe et al., 2004). Its origin and nature is one of the greatest mysteries of contemporary astronomy. Cosmology, in conjunction with particle physics, aims to determine the nature of the dark matter component. Although the various candidates proposed by particle physics are still undetected, we know from observations that the distribution of dark matter is more extended than the luminous matter (e.g. Rubin et al., 1982; Dekel & Silk, 1986), which together with the CMB argues for a nearly collisionless, massive particle.

3. **Dark energy**

Observations of the temperature fluctuations in the CMB have revealed that the Universe is nearly flat which means that the mean energy density of the Universe is close to the critical value for flatness, $\rho_{\rm crit}$ (e.g. Spergel et al., 2007; Planck Collaboration et al., 2016b). In contrast, the matter density ρ_m has been found to be $\sim 0.3\rho_{\rm crit}$ via measurements of the kinematic properties of galaxies, which show good agreement with $\Omega_{m,0}$ from CMB experiments (e.g. Planck Collaboration et al., 2016b). Both results suggest that the dominant component of the energy/mass content of the Universe must permeate homogeneously and not follow the large-scale baryonic structure, affecting chiefly the geometry and expansion history. The discovery of the acceleration of the Universe, as observed in the redshift–distance relation of high-redshift Type Ia supernovae (Rees, 1997; Perlmutter et al., 1997), provides further evidence for such a component. Since any baryonic or non-baryonic matter would decelerate any expansion, this component must be formed of energy with an exotic equation of state, hence the term *dark energy*.

1.1.2 History

In this section I give a summary of the history of the Universe in the standard model of cosmology.

Cosmological inflation

The standard cosmological model does not provide us with an explanation for the origin of the Universe. The theory provides a consistent scenario that explains the state of the observable Universe assuming certain initial conditions. Cosmological inflation is incorporated to explain major problems with the initial conditions. It operates at very high energy scale but sufficiently below the Planck energy, so allowing gravity to be treated classically. Inflation is an accelerated expansion that arises when the Universe is dominated by an energy component with negative pressure (e.g., vacuum energy). Therefore, the solution of the Friedmann equation in this phase corresponds to an exponentially expanding Universe. This exponential expansion makes the Universe extremely uniform, i.e. homogeneous and isotropic, so resolving what is otherwise a mystery in the standard model of cosmology. However it also predicts that quantum fluctuations can be expanded to the scale of the Universe, providing a small level of residual inhomogeneities that later grow into today's structure such as galaxies. Evidence from the CMB supports this pic-

ture but does not as yet tell us much information about the real physics behind inflation (Planck Collaboration et al., 2016a).

Nucleosynthesis

As the Universe cools from the initial very high temperatures, it becomes possible first for baryons to form from quarks, and later for the baryons to fuse together into the nuclei of simple atoms (Lara, 2005). The vast majority of heavy elements are synthesised in stars, however there is a primordial abundance of light elements (Hoyle & Tayler, 1964). The determination of the primordial abundances of light elements (such as hydrogen, helium, lithium) helps us to constrain the number of species of fundamental particles in the early Universe as well as the number density of baryons through the baryon–to–photon ratio η (e.g. Copi et al., 1995a; Burles et al., 2001)

$$\eta \equiv n_b/n_\gamma \approx 2.72 \times 10^{-8}\Omega_{b,0}h^2 \tag{1.3}$$

where n_b is the number density of baryons, n_γ the number density of photons and $\Omega_{b,0}$ is the present-day baryon density. The determination of primordial abundances (e.g., ^{4}He, ^{3}He, D, ^{7}Li) requires modelling of the properties of the observed gas clouds in the spectra of quasars. Corrections must be applied in order to get primordial abundances because material we observe today has been processed through stars. Although Big Bang nucleosynthesis is currently a successful parameter-free theory, it comes with some caveats. Measurements of the CMB power spectrum give an estimate for the photon-to-baryon ratio $\eta = 6.23 \pm 0.17 \times 10^{-10}$ (e.g. Kaplinghat & Turner, 2001), taking the values shown in Eq. 1.2.

However, predictions of the light abundances under the cosmological model are not in perfect agreement with observations (Copi et al., 1995a). For instance, estimates of the abundance of ^{7}Li appear to disagree with observations (Singh et al., 2017). This might be because of difficulties with the observations or the indication of new physics in the early Universe.

Formation of the cosmic microwave background (CMB)

The early Universe was very dense, hot and ionised, with a blackbody (thermal equilibrium) distribution of photons . As the Universe expanded and cooled, protons and electrons could join to form neutral hydrogen (at a redshift of $z = 1100$), the scattering rate of photons drops very rapidly. Photons could travel freely in a straight line to the

present day (to a first approximation). Therefore, the CMB is key for our understanding of the structure formation of the Universe. Observations of the CMB show that its spectrum is today perfectly consistent with the spectrum of a blackbody, with a temperature of $T \approx 2.725$ K. The CMB temperature distribution is highly isotropic over the entire sky (on very large scales), which supports the assumption that the Universe is homogeneous and isotropic on large scales. However, there are observed temperature fluctuations on smaller scales (Spergel et al., 2007). These small temperature fluctuations are believed to be caused by density perturbations, which are thought to be responsible for the formation of structures in the Universe. These fluctuations are known as the anisotropies of the CMB, and, they are useful to infer properties of the initial conditions for the formation of structure e.g., galaxies (Cole et al., 2005).

1.1.3 The flat Universe: Friedmann–Robertson–Walker metric

For a Universe that is homogeneous and isotropic only three possible space-time geometries can exist (Weinberg, 2008; Tegmark et al., 2004). The three-dimensional surfaces for such a Universe are described by the Robertson-Walker metric

$$\begin{aligned} ds^2 &= c^2dt^2 - dl^2 \\ &= c^2dt^2 - a^2(t)\Big[\frac{dr^2}{1-Kr^2} + r^2(d\theta^2 + \sin^2\theta d\phi^2)\Big], \end{aligned} \tag{1.4}$$

where c is the speed of light, $a(t)$ is the scale factor and K is a constant which takes the values +1, 0 and -1. The coordinates (r, θ, ϕ) are the comoving coordinates for a fundamental observer. A proper distance l between two fundamental observers is defined by,

$$l = a(t)\int_0^{r_1} \frac{dr}{\sqrt{1-Kr^2}} = a(t)\chi(r_1), \tag{1.5}$$

where $\chi(r)$ is a geodesic distance defined by

$$\chi(r) = \begin{cases} \sin^{-1} r & (K=+1) \\ r & (K=0) \\ \sinh^{-1} r & (K=-1) \end{cases}$$

Our apparently flat Universe is described by $K = 0$, which corresponds to a Euclidean flat space with potentially infinite volume (de Bernardis et al., 2002; Netterfield et al., 2002)

In relativistic cosmology, the Einstein field equation (Weinberg, 2008) describes the link between the geometry of the space-time and the matter/energy content of the Universe. The solution of the Einstein equations for a homogeneous and isotropic Universe (set by the Robertson-Walker metric) is the so called Friedmann equation,

$$H^2 = \frac{8\pi G}{3}\rho - \frac{Kc^2}{R_0^2}\frac{1}{a^2(t)}, \tag{1.6}$$

where $\rho(t)$ is the total energy density and R_0 is the present value of the curvature radius. A cosmology that obeys the Friedmann equation is referred as a Friedmann-Robertson-Walker cosmology. Therefore Eq. (1.4) is also commonly known as the Friedmann-Robertson-Walker metric. It underlies nearly all modern cosmological calculations.

1.1.4 Structure growth

In the standard cosmological model, structures (such as galaxies and clusters of galaxies) arise from small initial density perturbations (potentially during an early phase of inflation) due to the action of gravity. Density perturbations $\delta(\mathbf{x})$ grow only if they are larger than a characteristic length scale (known as the Jeans' length) beyond which gravity is able to overcome the pressure gradients.

The values of $\delta(\mathbf{x})$ are well-defined in the real Universe at each location in terms of a comoving position $\mathbf{x}$. But if inflation is correct, perturbations can also be treated as random variables that define a random field. This means that the Universe can be thought of a statistically homogeneous, in the sense that the statistical properties of $\rho(\mathbf{x})$ in any volume V of given size and shape are independent of the location of its centroid. Consequently, many physical theories predict only the statistical properties of δ (such as its two-point function or power spectrum) rather than δ itself, and observations must be appropriately compared to these statistical properties to test a theory. At early times perturbations were very small $|\delta| \ll 1$, so the evolution of the density perturbations fall in the linear regime.

The distribution of matter encompasses the distribution of dark matter, stars and gas. This relationship is strongly cosmology dependent, as well as dependent on the physics of galaxy formation (Springel et al., 2006). However, galaxy formation involves highly non-linear density fluctuations, which requires replacing the linear equation by approximations in the analytic arguments and numerical simulations to investigate the formation of structure.

1.1.5 The intergalactic medium

One can classify the gas component of the Universe into three categories: the interstellar medium (ISM), which is gas associated directly with the galaxy; the halo gas (also known as the circumgalactic medium; CGM), which is gas within the galaxy's gravitational influence but outside the galaxy; and the gas not associated with dark matter halos (the intergalactic medium; IGM). As mentioned above, the majority of baryons are not in galaxies but in the intergalactic medium. Galaxies interact with the intergalactic medium exchanging mass, energy and heavy elements. On large scales, the statistical distribution of matter can be traced not only by galaxies but also by this gas lying in the space between galaxies. Absorption lines from the spectra of background quasars can be used to probe the distribution of gas and the physical properties of the IGM, as I now describe.

1.2 The spectra from background quasars

Absorption lines observed in quasar spectra (see Fig. 1.1) provide us with detailed information on the kinematics and composition of the intergalactic medium and high redshift galaxies (e.g. Dobrzycki et al., 2002; Scott et al., 2000). Quasars (QSOs) are very bright objects that are believed to be powered by accretion of material in a central supermassive black hole.

QSO absorbers are useful probes of gas at high redshift due to a quasar's smooth intrinsic spectrum and intrinsic high luminosity (Lynds, 1971), meaning they can be observed at large distances. Photons emitted by quasars encounter clumps of gas along the line-of-sight in the intergalactic space (Sargent et al., 1980), tracing the density and the physical conditions over the intervening volume.

In particular, quasar spectra allow us to study in detail the absorption of multiple elements in a wide range of ionisation states, potentially giving simultaneous information on densities, metallicities and temperatures. At ultraviolet wavelengths, the most abundant features come from the neutral hydrogen ground state transition, known as the Lyman series (Lyman, 1906). High resolution spectroscopy is necessary to correctly transform the observed equivalent widths of the absorption lines into column densities, N(HI), (Hu et al., 1995). The resolution of this technique sets a lower limit in the HI column density at $\sim 10^{12}$ cm^{-2}. When column densities reach a value of 10^{17} cm^{-2} the intervening IGM becomes optically thick to Lyman continuum photons, providing an upper limit in

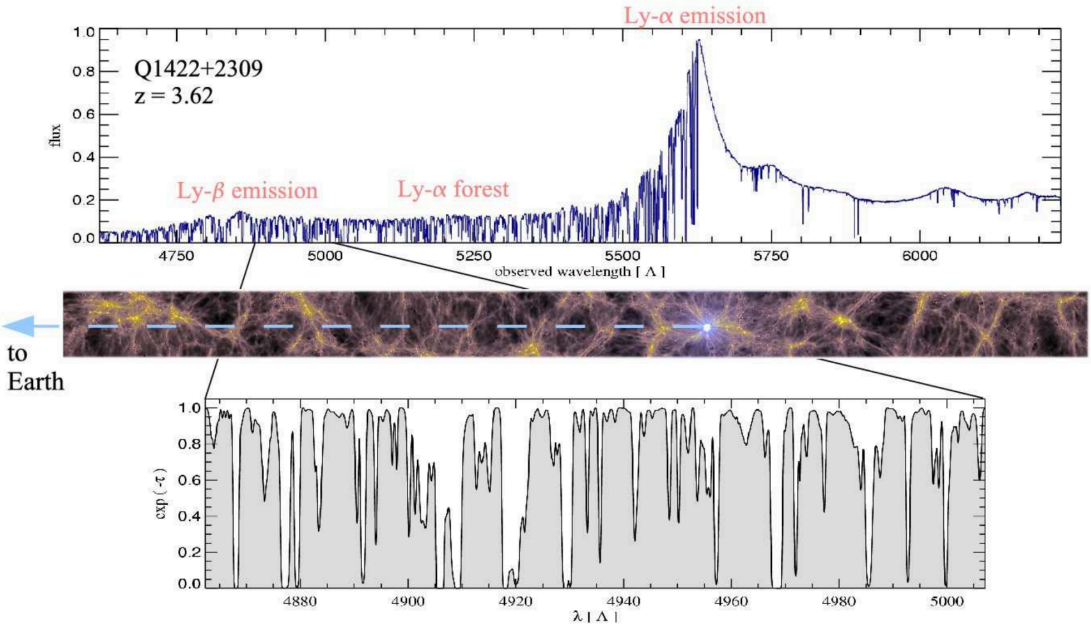

Figure 1.1: An example of a typical high-resolution spectra at redshift $z = 3.62$ (top panel) taken from Springel et al. (2006) and Rauch (1998).
The middle panel shows a sketch of the distribution of gas in a simulated universe. The bottom panel is a simulated spectrum from hydrodynamical simulations, showing that they can be reproduced with high fidelity by simulations assuming the standard cosmological model.

the HI densities, above which the physics becomes much more complex. Figure 1.2 shows a combination of observations that allow us to determine the HI column density distribution function $\mathscr{F}(N_{\rm HI}, z)$ i.e., the number of absorption lines per unit column density (Altay et al., 2011).

Thus, quasar absorption line system are divided into four categories:

- **Lyman α forest**: Intergalactic neutral hydrogen intersected by photons from background QSOs cause absorption of the QSO's Lyman-α emission line (Sargent et al., 1980).

- **Lyman-limit systems** (LLS) are optically thick systems at the Lyman limit, or in other words, systems with column densities N(HI) $> 10^{17}$ cm^{-2} (Bahcall et al., 1993). See Sec. 1.2.1.

- **Damped Lyα systems** (DLAs) are quasar absorption lines with HI column density, of N(HI) $> 2 \times 10^{20}$ cm^{-2} (Wolfe et al., 1993).

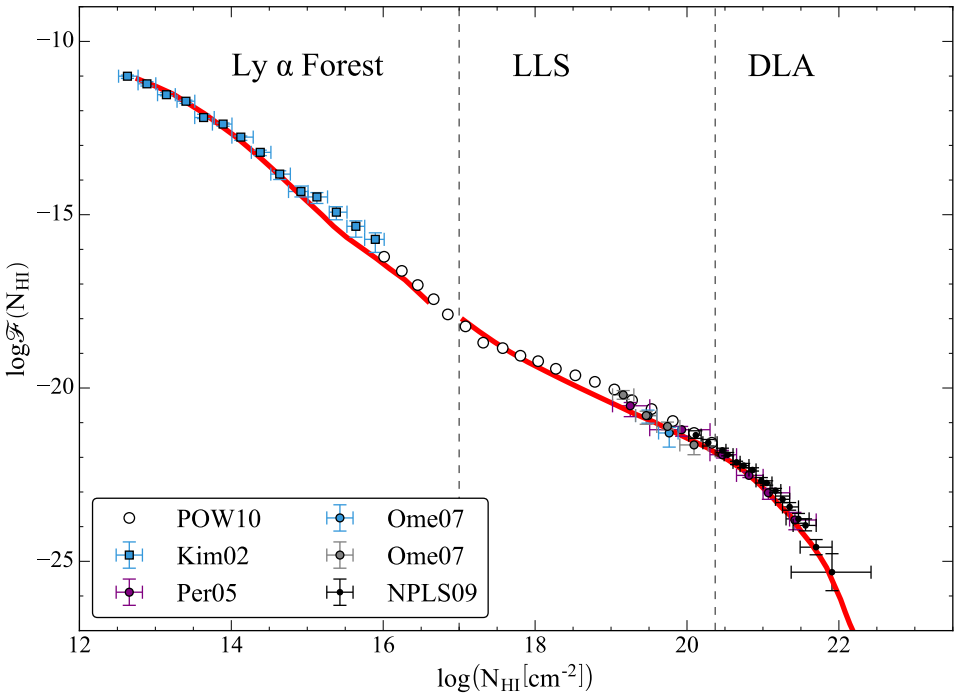

Figure 1.2: Number of absorption lines per unit column density showing the HI column density distribution of QSO absorption line systems. The solid curve shows low $N_{\rm HI}$ obtained using mock spectra, and, high $N_{\rm HI}$ obtained as a projection of a simulation box onto a plane. High-resolution observations of the Lyα forest correspond to 'Kim02' Kim et al. (2002). LLSs data are from 'Per05' Péroux et al. (2005) and 'Ome07' O'Meara et al. (2007). Analysis of SDSS DLA data is from 'NPLS09' Noterdaeme et al. (2009), and power-law constraints are in 'POW10' Prochaska et al. (2010); open circles are spaced arbitrarily along power-law segments. This plot was taken from Altay et al. (2011).

- **Metal absorption line systems**: QSO spectra also frequently show absorption lines due to metals. The best-known examples are MgII systems and CIV systems, which are caused by the strong resonance line doublets MgII and CIV respectively. Note that both doublets have rest-frame wavelengths longer than $\lambda_{\mathrm{Ly}\alpha} = 1216$ Å. Consequently, they can appear on the red side of the Lyα emission line of the QSO, which makes them easily identifiable because of the absence of confusion from the Lyα forest (e.g. Jannuzi et al., 1998; Bergeron et al., 1994).

In this work I focus on the first and last categories: the systems relevant for the Lyman alpha forest when studying the intergalactic medium on large scales; and, metal absorption line systems to study the dynamics of gas in the circumgalactic medium. LLS and DLAs are not directly considered in this thesis.

1.2.1 Lyman α forest systems

The physics of the Lyα forest.

Intergalactic neutral hydrogen intersected by photons from background QSOs cause absorption of the blueward of the QSO's Lyman-α emission line. The Lyα spectral line has a rest wavelength of wavelength $\lambda_\alpha = 1216$ Å. Photons emitted from a distant QSO (also known as the ultraviolet continuum) are redshifted to 1216 Å and can be absorbed by a cloud of neutral hydrogen. Due to redshift being a function of distance travelled, clouds of neutral hydrogen along the line-of-sight absorb photons at different wavelengths in the observed spectrum.

The Lyman-α forest refers to the resulting hundreds of distinct absorption lines observed with high resolution in the spectra of galaxies and QSOs (Weymann et al., 1981). All the lines blueward of the Lyα emission line in Fig. (1.1) make up the Lyα forest.

Even if the individual lines cannot be resolved, the presence of intergalactic neutral hydrogen, at $z > 5.5$, can be detected as a trough in the spectra of quasars (known as the Gunn–Peterson trough; Gunn & Peterson, 1965; Giallongo et al., 1994). Photons bluer than the quasar's Lyα emission are significantly absorbed, causing a substantial decrement of flux in the observed quasar spectrum at wavelengths shorter than $(1 + z_Q)\lambda_\alpha$, where z_Q is the quasar redshift (see Eq. 1.1). Because most of the absorption lines trace small density fluctuations in the IGM, these fluctuations are used to probe the underlying matter distribution on large scales. The forest is therefore sensitive to the cosmological

model (Viel et al., 2003; Norman et al., 2009) as well as the astrophysics of the individual lines.

Consequently, the optical depth $\tau(z)$ of the forest plays an important role when studying the IGM. It can be determined from the flux decrements in the quasar spectra. This quantity is closely related to the number density of neutral hydrogen atoms,

$$n_{\rm HI}(z) \sim 2.42 \times 10^{-11} \tau(z) h H(z)/H_0 \ {\rm cm}^{-3}, \tag{1.7}$$

where $H(z)$ is Hubble's constant at redshift z (Gunn & Peterson, 1965; Madau et al., 1999; Mo et al., 2010). At redshift $z \lesssim 6$, the value of τ is typically much smaller that unity, implying that the density of neutral hydrogen is very low. By comparing with the mean gas density in the Universe which is about 10^{-7} cm^{-3}, this tells us that the intergalactic medium must be highly ionised at redshifts $z \lesssim 6$.

Observational setting and key results

Models of structure formation under ΛCDM produce a filamentary IGM that is highly ionised by a UV background produced by galaxies (Viel et al., 2002). Both analytical models and hydrodynamical simulations (Rauch, 1998) have shown that the absorption blueward of the Lyman α emission line in quasars is due to the intervening gas in the IGM. Spectra obtained by these simulations are able to match the general observed properties of the Lyα forest.

Observations using high-resolution spectroscopy allow us to study the physics of the IGM. Here I mention some examples of important results from surveys and other observations.

Some of the earliest constraints on the Lyman-α forest come from samples of quasars observed individually with high resolution spectrographs (Boksenberg et al., 1978; Carswell & Ferland, 1980) In the redshift range $1.5 < z < 4$ optical telescopes are suitable for measuring the properties of the Lyman alpha forest. For example a lower limit in the HI column densities was measured by HIRES-Keck (Hu et al., 1995; Kim et al., 1997) and VLT/UVES (Kim et al., 2001)[2]. Also from Keck spectroscopy in conjunction with numerical simulations, limits on the baryon density were set using the neutral hydrogen column densities (Rauch et al., 1997).

[2]HIRES is a spectrograph on the Keck telescope and UVES is the high-resolution optical spectrograph of the VLT.

At low redshifts, one must go to space to measure the Lyman α forest. The Hubble Space Telescope (HST) made it possible to study, for example, results on the clustering and evolution of the Lyman α lines (Dobrzycki et al., 2002).

Measurements of the Lyman α opacity of the IGM combined with hydrodynamical simulations provide estimates of the photoionisation rate per hydrogen atom at high-redshift probing the ionisation history of IGM (Bolton & Haehnelt, 2007). The number of ionising photons emitted at $z = 5 - 6$ seem to be in reasonable agreement with the photoionisation rates inferred from the Lyman α forest for galaxies with a large photon escape fraction. However at lower redshifts it is unclear whether this agreement is maintained (Kollmeier et al., 2014; Nasir et al., 2017; Gurvich et al., 2017)

A significant uncertainty in these constraints is that they depend on the density and temperature of the forest. Observations from the VLT (UVES) corroborated expectations from numerical simulations on the temperature state of the low-density IGM due to adiabatic cooling and photo-heating by the UV background (Theuns et al., 2001) but significant uncertainties remain. More recent studies of the temperature in the IGM attempt to characterise its thermal history (Rorai et al., 2017; Nasir et al., 2016; Boera et al., 2016; Becker et al., 2011).

To make sense of observations, we require theoretical models. Semi-analytical models of the Lyman α forest have proved to be able to reproduce observed properties such as column density distribution function (Viel et al., 2002).

More accuracy is available from hydrodynamical simulations that can model the dependence of the Lyman α flux-power spectrum on dark matter, cosmological parameters, and, thermal history of the IGM. These simulations have been calibrated with low resolution SDSS/BOSS data (Palanque-Delabrouille et al., 2015) and intermediate resolution data from VLT/X-Shooter (Iršič et al., 2017), to help constrain the small scale power spectrum and so dark matter models and/or neutrinos (Viel et al., 2013).

At lower resolution, it is also possible to use the statistical power of large numbers of quasars to constrain the power spectrum of the underlying dark matter distribution, constrains on inflation and neutrino masses (Slosar et al., 2011).

They can also be used to fit the large-scale Lyman α forest data, leading to cosmological parameters in approximate agreement with the CMB power spectrum (Font-Ribera et al., 2014) although there is a slight parameter tension at the 2σ level which remains poorly understood. The statistical power of observations to obtain these constraints has

only become possible through large automated surveys (Font-Ribera et al., 2014).

Future of the Lyman α observations

Over the range $2 < z < 5$ large statistical samples of observed data matching the expectations from cosmological simulations (McQuinn, 2016; Hirata, 2017). The Lyman-α forest was quickly identified as a potential tool for precision cosmology and, in the last decade, all-sky surveys have provided the data to constrain cosmological parameters. In particular, the baryonic-acoustic oscillations (BAO) as observed with the Lyα forest (by the Baryon Oscillation Spectroscopic Survey; BOSS) has allowed us to measure the cosmic expansion at z $\sim$ 2.3 (Font-Ribera et al., 2014) , where little information from other methods is available (e.g. SN type Ia or galaxy clustering). It is expected that these measurements will be vastly improved in a wider range of redshifts with future facilities such as the Dark Energy Spectroscopic Instrument (DESI; DESI Collaboration 2016).

1.2.2 The circumgalactic medium (CGM): Metal absorption lines

In this section I discuss the metal contamination of the circumgalactic medium by galactic outflows. Absorption lines due to metals, also seen in the spectra of background quasars, provide us with information on the dynamics and composition of material in galactic halos.

Quasar absorption techniques show that galaxies in the local Universe are surrounded by a highly ionised plasma that extends for hundreds of kpc and that is also enriched with metals (Tumlinson et al., 2013; Werk et al., 2014). The very common species CIV, MgII and OIV observed in QSO spectra make it possible to study the distribution and physical conditions of gas around galaxies (Bordoloi et al., 2014; Tumlinson et al., 2013; Werk et al., 2013; Nielsen et al., 2013). Strong lines are associated with highly ionised and low density gas in both the IGM and the CGM. However, CIV absorption systems can be also produced by collisionally-ionised gas with high temperatures ($T \sim 10^5$ K), or produced by shocks associated with galaxy halos. This illustrates a broader point that the information in absorption lines must be decoded by comparison to a physical model, since the presence or absence of a particular ion may reflect either metallicity, density, temperature, ionising radiation intensity, or some combination of all these.

Observations show that the mass of the gas around star-forming galaxies is estimated to be comparable to their stellar mass (Werk et al., 2014), and also the amount of metal

mass in the halos is comparable to the metallicity mass in the interstellar medium (Peeples et al., 2014). This large reservoir of gas is thought to be driven or built up by galactic outflows.

The physical mechanisms that transport material into the halos are complex and non-linear. For this reason, it is common to use cosmological hydrodynamical simulations to model the observational data (Meiksin et al., 2014). The mechanisms that drive outflows and the basic parameterisation of the conditions that trigger them remain unknown. Models aim to predict how far the wind will travel, how much mass it carries, their velocities, even whether the wind will escape into the IGM or whether gravity will pull it back to the galactic disc. In some cases, multiple cosmological simulations have been used where outflows with different scaling relations have been explored and matched to observations (e.g. Oppenheimer & Davé, 2006). This gives an alternative view on the physics controlling the galaxy population, since outflows are thought to play a crucial role in regulating the star formation.

However, the nature of outflows is multi-phase (it spans several orders of magnitude in temperature) making them difficult to model without very high resolution or special techniques.

Observations

Galactic winds have been observed in galaxies from redshift $z \leq 0.1$ (Bordoloi et al., 2014) to $3 < z < 4$ (e.g. von Glasow et al., 2013) and beyond (e.g. D'Odorico et al., 2013; Becker et al., 2011). They can travel at several hundred of km s^{-1} in star-forming galaxies at all redshifts (Steidel et al., 2010).

Galaxies exhibit strong correlations between their physical properties; such as stellar mass, gas content and CGM metal content (Tumlinson et al., 2013; Peeples et al., 2014). These relations evolve with redshift, towards lower metallicity and higher gas content at higher redshift, e.g., Davé et al. (2011a). The correlation between mass and metallicity in low-mass galaxies could be due to outflows (e.g. Dekel & Silk, 1986; Erb et al., 2006). To understand better the nature of the processes in the gas one has to rely on modelling the outcome because gas is either too hot or too diffuse that it is difficult to observe directly. To study the effect of metallicity and magnetic fields some authors (Davé et al., 2011a; Wiersma et al., 2009; Finlator & Davé, 2008) have performed hydrodynamical simulations with solar metallicity finding that they produced a more efficient cooling (Scannapieco &

Brüggen, 2015; Wiersma et al., 2009).

One way to improve our understanding from observations is to correlate the CGM gas properties with the host galaxy (Tumlinson et al., 2013). For example, outflows should be able to develop in small galaxies because their smaller potential results in lower escape velocities.

Although it is very clear from observations that material is being expelled from the galaxies, it is not very clear how far this material travels (Steidel et al., 2010).

Because CIV is an accessible tracer of hot ionised gas, recent surveys use this line to systematically map the distribution of CIV gas out to their viral radii (Bordoloi et al., 2014). It has been controversial whether metals observed in the CGM belong to the galaxy potential or not. To tackle this problem a comparison of the azimuthal asymmetry of absorption line systems (e.g., CIV and MgII) would us allow to constrain the geometry of the multi phase CGM (Fig. 1.3, Bordoloi et al., 2014).

Finally, numerical simulations are an important tool to make predictions in galaxy formation and to confront them with observations. The important physics is still not well understood (Somerville & Davé, 2015; Springel et al., 2005). Currently, hydrodynamic cosmological simulations including radiative cooling and star formation, at best, coarsely reproduce the observed properties of galaxies (Schaye et al., 2015)

The importance of outflows to galaxy formation

Outflows are likely to play a central role in galaxy evolution because they occur in star-forming galaxies of all masses at all redshifts. They are thought to be caused by energetic feedback from massive stars, supernovae and accreting black holes travelling faster than the escape velocity of the host galaxy removing star-forming gas from it (Keller et al., 2014; Krause et al., 2014). It is thought that for galaxies with dynamical masses $M \lesssim 10^{12}$ $\mathrm{M}_{\odot}$ they are generated by clusters of stars that are very efficient at generating gas motions (Creasey et al., 2013; Keller et al., 2014).

They are invoked to explain correlations in low-mass galaxies, e.g., the strong correlations between mass and metals (Keller et al., 2014; Recchi & Hensler, 2013), to explain the faint end in the luminosity function (Fig. 1.4, Cole et al., 2000a) and as a probable mechanism for the enrichment of the IGM (Scannapieco et al., 2005).

Moreover outflows and galactic fountains may dynamically reshape a galaxy and its dark matter (Pontzen & Governato, 2014), meaning the properties of the CGM may ulti-

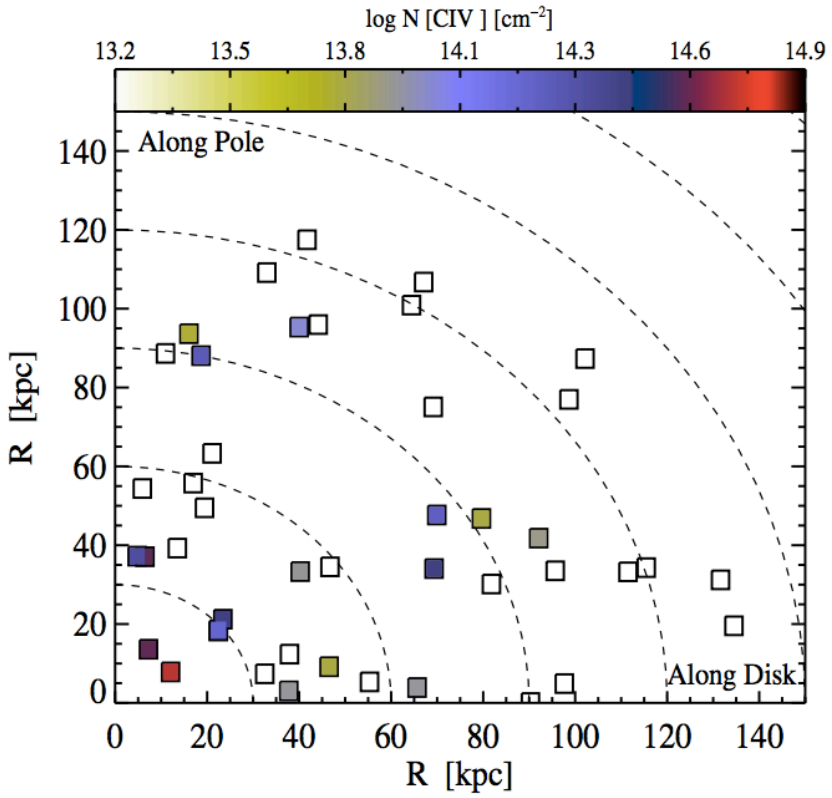

Figure 1.3: Two dimensional projection of the CIV absorption line from COS-Dwarfs survey (Bordoloi et al., 2014). The points lying along the y axis represent lines of sight passing along the projected minor axis of the galaxy and the points lying along the x axis represent lines of sight passing along the projected major axis of the galaxy. Detections are indicated with coloured filled squares and non-detections with blank squares. Colours reflect the absorption strength. Stronger absorbers tend to be aligned towards the minor axis of the galaxies. However, the trend is not statistically significant. It therefore remains unclear whether CIV absorbers are spherically distributed around galaxies, but, the measurements of CIV can be compared against the MgII absorption line systems to constrain the geometry of the multi-phase CGM.

mately serve as an essential cross-check of galaxy formation in the dark matter paradigm.

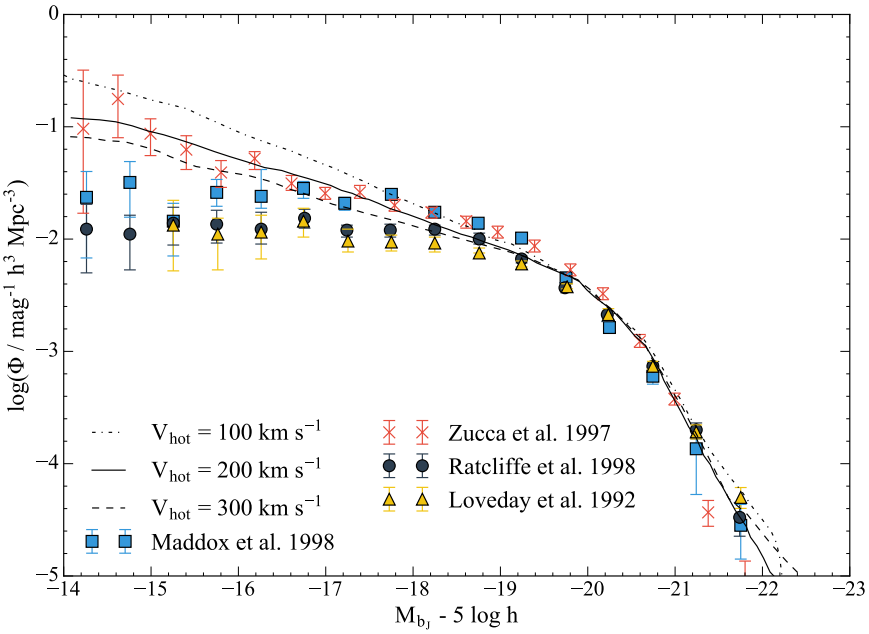

Figure 1.4: Semi-analytical models to show the effect of galactic winds parameterisation on the luminosity function. $V_{\rm hot}$ is a normalisation factor in the efficiency of stellar feedback term and has velocity units . Increasing $V_{\rm hot}$ lowers the faint end of the luminosity function illustrating the close relationship between galactic outflows and galaxy properties. The lines correspond to different models, the black line is a model which includes gas which has been cooled. For more information refer to Cole et al. (2000b).

1.3 Motivation and Outline

This thesis aims to study unresolved theoretical questions about the distribution of gas ions in the intergalactic medium and the circumgalactic medium. In this section, I present the motivation that led to this work based on the current theoretical and observational scenario and emphasize the questions that remain unanswered.

The main goal is to understand the physical processes that produce the distribution of the different gas phases, in both the CGM and IGM. In Sec. 1.2.2, I explained that based on observations, outflows are best described as a system of gas distributed in a filamentary biconical region that expands at least several kpc from the galactic disc (and possibly much further). These filaments are classified in different regions according to their tem-

perature. Detailed spectroscopic studies show a portion of gas at T$\sim 10^4$ K (also called the warm-ionised phase) that is being photoionised by the (starburst) galaxy. Kinematic studies reveal that this phase is distributed along the surface of the biconical structure and the cones are presumably filled with outflow fluid. Colder phases at $T < 10^3$, which allows the presence of molecular gas, extend far beyond the stellar disc and follows a wider biconical shape than the hot phases (as observed for instance in M82; Leroy et al., 2015).

We have learnt from multiple datasets and cosmological simulations that the multi-phase nature of outflows is complex. We want to understand the mechanisms that produce them and to explain how they can coexist. Observations show that there is a tight spatial correspondence between the hot and cold phases (see Chap. 2). While the hottest phase is the easiest to understand (but the hardest to detect), colder phases are difficult to explain. The hottest phase exceeds the escape temperature (T_e) of the galaxy explaining why there is highly ionised gas observed out of the host galaxy. However, the colder phases are observed to be ubiquitous in the galaxy (e.g. Veilleux et al., 2005), making them currently one of the main questions about outflows. They could be formed as a transformation from other phases (*in situ*), or, possibly they are clouds driven out from the galactic disc. If the latter is the case, it is not clear how they can travel so far without being disrupted. Cold clouds reach high velocities, estimated between $100 - 1000$ km s^{-1} (Heckman & Thompson, 2017). The questions is how these clouds can travel at such velocities and remain cold. Shock heating while traveling would cause them to increase their temperature. In this thesis, I address this question by performing a numerical analysis of the physical properties of small galaxies, using hydrodynamical simulations (see Chap. 4).

Additionally, spectra of galaxies indicate that material is flowing onto the galaxy (Martin et al., 2012; Chen et al., 2017). These flows potentially inject gas that will help form new stars. However, galaxies contain inflows and outflows of baryons in unknown proportion. This is an important issue to address since (theoretically) the gas accretion rate regulates the galaxy's star formation rate (e.g. van de Voort et al., 2011a), and thus, the balance between gas outflow and inflow has consequences on the determination of metallicity and stellar mass (e.g. Davé et al., 2011a). The main problem with inflows is that they are harder, than outflows, to determine observationally. The kinematics of the absorption lines imprinted on the galaxy spectra tell us whether gas is inflowing or outflowing, and this comes with a systematic error. Given the different projected velocities between them,

the inflow features are difficult to separate from rest-frame galaxy absorption and/or emission lines, thus introducing a systematic bias towards their detection (Rubin et al., 2012).
Overall, while inflows carry angular momentum that can play a role on the rotation of the galactic disc (Stewart et al., 2011) as well as helping to form new stars, outflows can remove material from the galaxy affecting its star formation rate while polluting the CGM and IGM. Since the ratio between in and out flows is highly dependent on with feedback (e.g. van de Voort et al., 2011a,b) they have important repercussions on the galaxy as a whole. New datasets of large-scale outflows, in combination with simulations, will allow us to investigate outflows at higher redshifts and to infer their role on the evolution of galaxies.

In Sec. 1.2, I have described how the Lyman-α forest probes the diffuse gas in the IGM at high redshifts; which not only allows us to study the distribution of baryons in the cosmic web, but, also contains information of the IGM thermal state, the BAO, the reionisation epoch, and more. The balance between the photo-ionisation heating and adiabatic cooling sets the thermal state of the low density IGM (e.g. Bolton et al., 2014), and, is a key aspect when modelling the Ly-α forest. The UV background and cooling rates are tightly related and are central aspects of several astrophysical problems. Particularly when modelling the density fluctuations, an implementation of the UV background is necessary as the source of ionising photons. Since these sources do not radiate isotropically, an adequate analysis considering anisotropic emission is needed in the models.
Nowadays an archive of high resolution spectra exists, mostly divided in two sets; small data sets that account for few tens of spectra (e.g. Walther et al., 2018) and the big surveys such as BOSS (Slosar et al., 2011) and SDSS (e.g., Comparat et al., 2016). These datasets have allowed the community to analyse the power spectrum of the Lyα forest.
However, accurate measurement of the Lyα power spectra requires the development of good pipelines to correct for finite resolution of the detectors and noise. They are dependent on the determination of the continuum, which requires accurate values of the mean flux (Lee et al., 2012). Accurate quasar continuum fitting is not trivial and accurate determinations of the Lyman-α power spectrum on large scales have not yet been obtained even though the raw data exists to do so. It is therefore timely to understand the theoretical predictions for what will be measured. On large scales, density of the neu-

tral hydrogen was, until recently, thought to closely trace the total mater density, and, the spectra of quasars allow us to sample the distribution of gas from on line-of-sight to another. Analytical models such as the ones presented in this thesis will help with the interpretation of the forthcoming data (see Chap. 6).

Building better theoretical models of the distribution of gas will ultimately allow us to understand the information obtained from the spectra of background quasars, although direct comparisons to data are outside the scope of the current work.

This thesis is divided in two parts: galactic outflows and the Lyman-α forest.

In Chapter 2, I summarise the basic observational properties of halos of star-forming galaxies and galactic outflows. Chapter 3 presents a brief description of the hydrodynamical code (RAMSES) which was used to study the mechanisms that drive outflows. In Chapter 4 I present the parameter study and simulations of outflows launched from central galaxies undergoing repeated starbursts that propagate through the circumgalactic medium.

The following chapters concern the Lyman alpha forest as tracer of the large scale structure. I give a brief summary of the required theory behind random Gaussian fields in Chapter 5. This provides a preamble to Chapter 6, where I model the post-reionisation neutral hydrogen density in the IGM to understand the consequences of beamed sources in a non-uniform ultraviolet background. Finally, Chapter 7 presents the main conclusions and future directions.

This thesis includes material from the two papers:

- *Bursty star formation feedback and cooling outflows*
  Suarez, T., Pontzen, A., Peiris, H.V., Slyz, A. and Devriendt, J., Mon. Not. R. Astron. Soc. 462, 1 (2016)

- *Large-scale fluctuations in the cosmic ionising background: the impact of beamed source emission*
  Suarez, T. and Pontzen, A., Mon. Not. R. Astron. Soc. 472, 3 (2017)

Chapter 2 | *Galactic winds*

"Truth is ever to be found in simplicity, and not in the multiplicity and confusion of things "

- Isaac Newton

Galaxies are open systems that expel and accrete gas. A percentage of the gas in galaxies is turned into stars (Chisholm et al., 2016; Leroy et al., 2008). A fraction of these new stars are high-mass stars that eventually will explode as supernovae (Veilleux et al., 2005). Supernovae explosions carry enough energy to push part of the gas from star forming regions out of the galaxy, which make SNe explosions one of the main candidates for mechanisms that are able to drive galactic outflows.

Material outflowing from galaxies show a wide distribution of velocities and temperatures (Erb, 2015). Part of the gas travels with high velocity and escapes the galaxy potential. The portion with lower velocities fall down to the galactic disk in form of galactic fountains (Chisholm et al., 2016), enriching the next generation of stars. The transportation of gas from massive stars to the galactic halo enriches the circum-galactic medium (CGM) with metals from the star- forming regions (Tumlinson et al., 2011; Werk et al., 2014).

The accretion of gas from the CGM helps to explain why galaxies do not consume all their gas. Outflows from feedback have important consequences for the regulation of star formation. Gas depletion timescales are short (less than the Hubble time). Therefore, gas fractions and star formation rates are determined by the amount of gas that is being accreted and stellar feedback (Genzel et al., 2010). Without the balance between these two processes, star formation would consume all gas. Accretion or mergers are required to explain the replenishment of gas.

Outflows' properties help us to understand the mechanisms behind feedback. In this chapter I will revise the main characteristics of galactic winds. I will also discuss constrains from both observational and theoretical work.

2.1 General observable properties of outflows

To understand the general properties of outflows, it is common in the literature to start by pointing out the prototypical starburst-driven outflow: M82.

M82 is a starburst disk galaxy in the local Universe with a biconical outflow emerging from its central starburst (see Fig. 2.1). It is in interaction with the companion M81 galaxy, which is thought to have activated the central starburst in M82 (Yun et al., 1993). Located at only $\sim 3.6Mpc$ (Sakai & Madore, 1999), M82 is the best example to explain outflows and its multi-phase nature.

M82 summarises the characteristics of outflows present in other star forming galaxies. Star formation heats the gas to high temperatures and propels a portion of this gas to velocities larger that the escape velocity of the galaxy. Such outflows have important consequences in the evolution of the galaxy. Most of the gas in it is entrained by a hot wind fluid. The wind propagates outward from the disk making unclear how cold clouds survive in the hot flow (Strickland & Stevens, 2000). The amount of gas entrained in the wind is comparable to the amount of gas that is being formed into stars (Rupke et al., 2005). Assuming a standard Chabrier initial mass function, the SFR is inferred to be $SFR \approx 10$ $M_\odot$ year^{-1} (Heckman & Thompson, 2017). The starburst radius of ≈ 500 pc gives a SFR per unit area is about 15-20 $M_\odot$ year^{-1} kpc^{-2} (Chisholm & Matsushita, 2016). The escape velocity of M82 is around ≈ 500 km s^{-1} (Strickland & Heckman, 2009), so at least some of the observed outflows has sufficient energy to escape its potential.

Starbursts at $z \approx 0$ are relatively rare, but, star-forming galaxies at higher redshifts show similar characteristics to M82 and the existence of outflows in most of them is now well established (Erb, 2015). Observations are more challenging at higher redshifts. For instance, gas emitting in X-rays is only detectable in the nearby Universe(Strickland et al., 2004). However, at high redshift colder phases are easier to observe as absorption features in quasar spectra (George et al., 2014) . And, although it is important to understand the connection between the motion of cold gas and the X-ray emitting gas, it is unknown how they form and where the cloud of cold gas originates.

The general picture that stands from observations is that energy and momentum injected from massive stars and supernova (or active galactic nuclei - AGN) into the interstellar medium (ISM) of galaxies is the mechanism behind galactic outflows (Heckman &

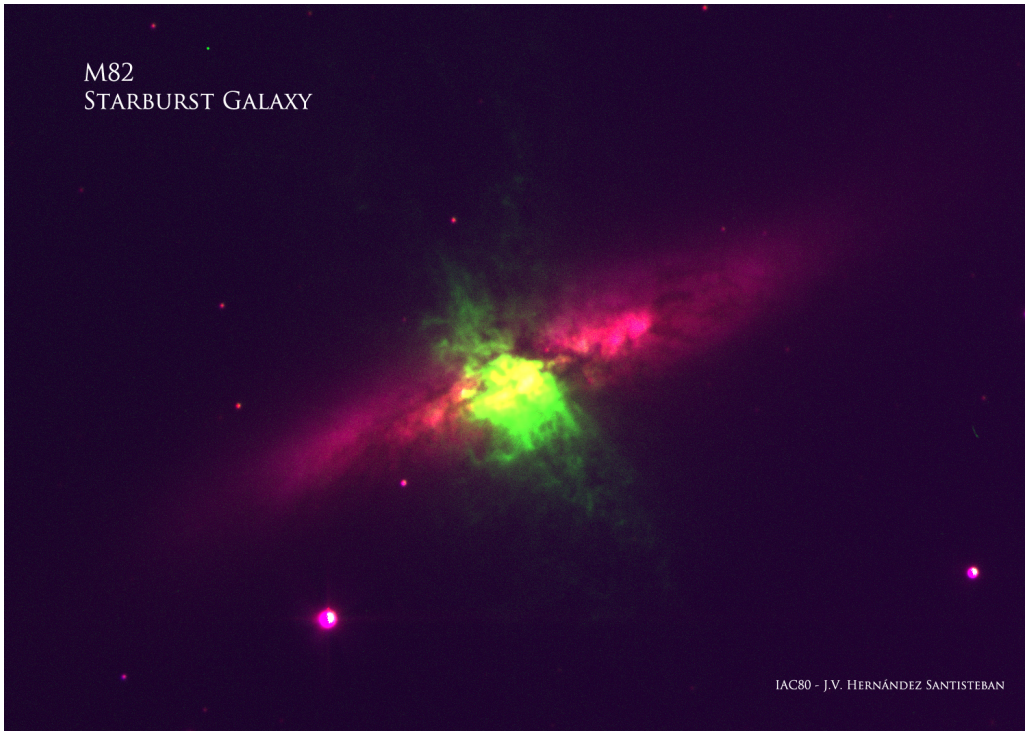

Figure 2.1: M82 through the filters Hα (green) and Johnson-R (red) band. The prototypical example for a starburst galaxy and evidence of outflows.
Image Credit: J.V. Hernández Santisteban

Thompson, 2017; Sell et al., 2014). Metals from supernova are expelled from galaxies into the CGM, potentially entraining significant amounts of cool gas (10^4 K) in the process (Heckman & Thompson, 2017).

When decomposing the multi-wavelength observations of the gas we can classify the different phases of the outflow in four categories (Lehnert et al., 1999; Walter et al., 2002; Strickland & Heckman, 2009; Erb, 2015),

- Hot gas traced by X-rays, $T \approx 10^7$ K -10^8 K, is best to probe feedback on the galactic scale (Strickland et al., 2004; Zhang et al., 2014).

- Hot ionised gas, $T \approx 10^5$ K, seen via soft X-rays and optical emission lines such as Hα (Strickland, 2002). This gas travels at velocities of 600 - 800 km s^{-1} and suggests the presence of shocks.

- Neutral gas probed by low ionisation absorption lines (warm ionised phase), $T \approx 10^4$, is detected as an optical emission line and ultraviolet (e.g. Martin, 2005). The spatial distribution and kinematics of this gas is controlled by radiative feedback

or feedback from supernovae (Strickland et al., 2004). Gas in this phase is detected several kpc from the central starburst along the minor axis.

- Molecular gas observed at radio wavelengths, $T \approx 10 - 10^3$ K (Walter et al., 2002). Observations of CO emission show outflows with $\approx 3 \times 10^8 \mathrm{M}_\odot$.

Another promising technique for detecting hot diffuse gas (although not the same outflows) is the **thermal Sunyaev-Zel'dovich** (tSZ; Sunyaev & Zeldovich, 1980), which is used to find gas around clusters. The tSZ effect happens when photons from the CMB travel through clusters of galaxies being scattered (Compton scattering) by electrons in the hot intergalactic gas of such clusters. The warm-hot gas phase in the intra-cluster medium can also be observed with X-ray emission or absorption in the spectra of QSOs (Penton et al., 2004). However, attempts show inconclusive results when accounting for baryons (Shull et al., 2012), mostly because this phase is difficult to observe. The tSZ technique makes ionised gas accesible with observations (Sunyaev & Zeldovich, 1980; de Graaff et al., 2017), establishing the presence of ionised gas in large-scale filaments $\sim 15\ h^{-1}$ Mpc (de Graaff et al., 2017; Colberg et al., 2005).It works as a probe of baryonic gas at low and intermediate redshifts i.e., $z \lesssim 2$ (Tanimura et al., 2017).

2.1.1 Scaling relations

General properties of outflows from observational constraints (e.g., velocity as a function of radius and the mass outflow rate) and the determination of scaling relations of outflow properties with galaxy mass and star formation are essential to understand the physics behind outflows and the underlying mechanisms that drive outflow.

Observations show that properties of outflows are closely linked to the properties of galaxies. For instance, massive star forming galaxies with high star formation rate tend to drive faster outflows e.g., Heckman et al. (2011). Measurements from the spectra of ultraluminous infrared galaxies (ULIRGs) show that the relation between the velocity of the outflow and SFR indicate that more luminous starbursts accelerate gas from the ISM to higher speeds $v \propto \mathrm{SFR}^\alpha$ where $0.1 < \alpha < 0.35$ (Martin, 2005; Erb, 2015) .

Velocities

Studies of the kinematics show that there is a tight correlation between the outflow velocity and the outflow temperature (Veilleux et al., 2005). It is essential to know the

gas distribution of the outflow component to be able to infer the observed velocities. For instance, molecular gas is ejected at ~ 230 km s^{-1} out of M82 (Walter et al., 2002) whereas warm ionised gas travels at ~ 600 km s^{-1} (Shopbell & Bland-Hawthorn, 1998).

Outflow velocities are inferred via absorption lines by comparing the redshift of the absorber to that of the host galaxy (Fox & Richter, 2016). It is now well established that warm/hot gas in the CGM is present around galaxies at low (Prochaska et al., 2006) and high redshift (Simcoe, 2006). The relative motion between this warm/hot phase causes velocity offsets between the weakly and highly ionised gas (Fox & Richter, 2016).

Typical outflow velocities lie in the range 10 km s^{-1} $< v_{\rm outflow} <$500 km s^{-1}. The outflowing component maximum velocities, usually defined by the most-blue-shifted bit in the line, are typically $300 \ {\rm km \ s^{-1}} \lesssim v_{\rm max} \lesssim 1500 \ {\rm s^{-1}}$ (Chisholm et al., 2015; Veilleux et al., 2005).

Rates of mass, momentum, and kinetic energy

Often absorption lines are found in quasar spectra without a known host. At high redshifts, the host galaxy of quasars is small and dim, and usually unresolved (Steidel et al., 2010). Thus, difficult to separate the absorption features from the quasar spectra. This problem is vastly overcome at lower redshift, where galaxies tend to be relatively bright.

Gas in the CGM is similar in nature to the intracluster medium detected with X-rays. The CGM is less dense with lower temperatures (Werk et al., 2013) so it cannot be traced by X-ray. Therefore, observations of the CGM are taken via UV absorption lines. Systematic efforts to map outflows around galaxies are taken in order to characterise the CGM at low redshift $z \lesssim 0.2$, specifically searching for absorption near known hosts e.g. COS-HALOS survey (Werk et al., 2014) and at lower mass COS-Dwarfs survey (Bordoloi et al., 2014).

In the distant universe, metal lines redward of Ly-α can be analysed when the forest is saturated. Profile analysis (such as Voigt decomposition) of the Ly-α forest have allowed to quantitatively measure the distribution, column density, kinematics, and absorber line widths of neutral hydrogen (H I) at $z \sim 2$ (Rudie et al., 2012). Furthermore, spectroscopic analyses of Ly-α emitters at $z \sim 6$ show evidence for CIV absorption associated with outflows (Díaz et al., 2015), implying that outflows can enrich large volumes at large redshifts.

At redshifts $1 < z < 4$, the sample of galaxies that have been observed to detect outflows lie in the masses values of $\sim 10^{12} M_{\odot}$ (Adelberger et al., 2005) . While in the local

Universe properties such as mass, SFR and metallicity are tightly related (Mannucci et al., 2010), at high redshifts this mass-metallicity seems not to evolve (Mannucci et al., 2010) when comparing with the local case. Estimations of metallicities and SFR at high redshift are still uncertain, but relations such as mass-metallicity and mass-SFR seem to evolve with redshift (Mannucci et al., 2009).

In the future, it may be possible to carry out blind searches for the galaxies hosting a metal absorption line using wide integral field spectroscopy (e.g. from the MUSE spectrograph, Bacon et al., 2010)

2.2 Modelling outflows

Models have explored mostly two approaches to the description of wind-driving mechanisms: feedback from thermal energy and from kinetic energy (Oppenheimer & Davé, 2008). Driving outflows by injection of thermal energy from supernovae was successful in driving fast outflows into the galactic halo or beyond (Kobayashi, 2004). Due to limited resolution, previous studies using simulations had to consider other techiques to avoid overcooling (Chisholm et al., 2017). It seemed that only thermal energy was not to enough due to the high energy required by SNe. For example, in the real galaxies only a small fraction of the energy from supernovae is transferred to galactic winds. Other models addressed momentum-driven galactic winds that provide some scaling relations compatible with observations, with the advantage that momentum cannot be radiated away, in comparison to thermal energy (Murray et al., 2005).

It is clear that different feedback processes dominate in different environments and how they are implemented in the simulations results in complex and non-linear interactions. In all environments, outflowing gas shows in observations a broad distribution in temperature and velocity.

In particular, both ionised gas and neutral atomic gas reaches high velocities in many systems. Velocities range from 100 -1000 km/s (Heckman & Thompson, 2017).

A key physical problem in the theory of galactic winds is how to accelerate clouds of cool gas (i.e., atomic and warm ionised) to the observed velocities (many hundreds of km/s) without being disrupted by shocks, as it is seen in emission and absorption.

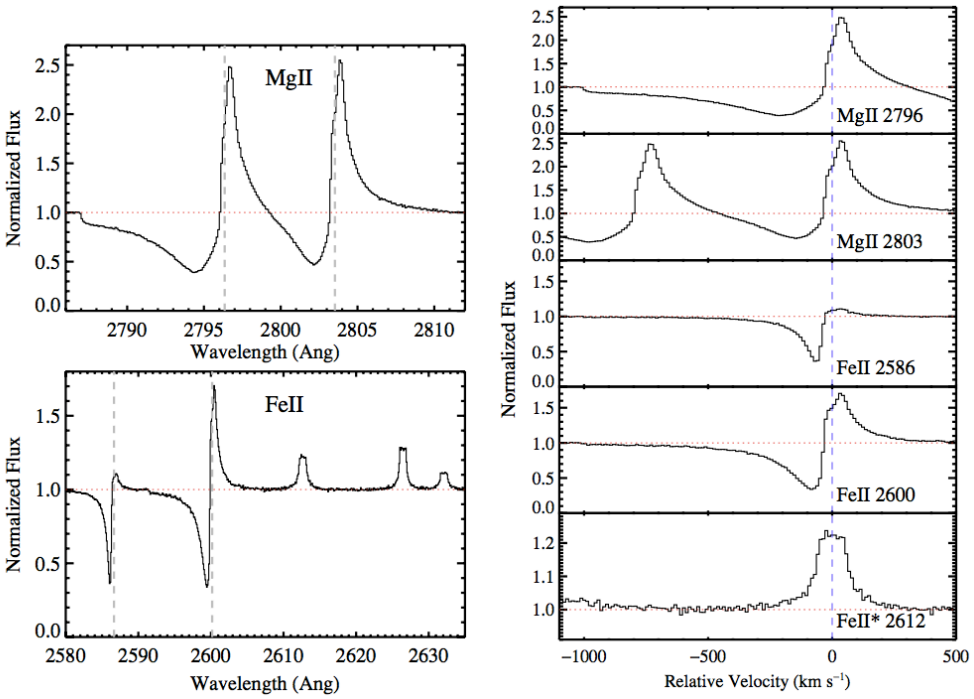

Figure 2.2: MgII $\lambda\lambda$2796,2803 and Fe II $\lambda\lambda$2586, 2600 profiles for the wind models described in Prochaska et al. (2011). The doublet shows the P-Cygni profiles characteristic of an outflow with significant absorption blueward of line center (dashed vertical lines) with velocities extending to v =-1000 km s^{-1}.

2.2.1 Simulating outflows

Implementing feedback prescriptions in a cosmological context is limited by the computational resources available at the moment. The range of scales that encompasses all the processes involved go from cosmological scales to molecular clouds and the details of the physical processes involved are also poorly understood. As a consequence, small-scale processes are typically not resolved by the simulation.

Nonetheless, with the improved computational resources and more detailed physics, simulations are now able to reproduce a wide variety of observed relations, while providing us with valuable insights of the physics governing outflows. We know now that outflows have a strong impact on galaxies (on their stellar, gas and metal content). In fact, insights from simulations have motivated arguments about galactic outflows being essential to moderate the stellar content, SFR, gas and metallicity in galaxies and their evolution at all epochs.

When studying galactic outflows in a cosmological scenario, authors have explored

mass, metal and energy feedback from galactic winds.

Simulations can be useful to explore global energy and enrichment properties of the IGM with and without feedback from SN (type 1a) and massive stars (e.g. AGB). Also, it is possible to explore particular feedback prescriptions over the history of the Universe (Richardson et al., 2016; Kimm et al., 2015) and over a large dynamic range in galaxy mass (from cosmological scales to the scale of individual stars or at least molecular clouds).

Detailed physics in simulations.

When adding the physics of these processes to simulations, typically an approximate feedback is modelled by adding **thermal** or **kinetic energy** to the surrounding gas particles(Springel & Hernquist, 2003). Kinetic feedback usually assumes that all the energy from supernova is transformed into kinetic winds (Mihos & Hernquist, 1994) with constant velocity in order to match the observed enriched IGM as well as the star formation history of the Universe (Cen & Ostriker, 2006). One of the problems with the kinetic energy wind is that even transforming all the energy from SNe, it seems not to be sufficient to drive galactic winds, being more problematic at lower redshifts (Oppenheimer & Davé, 2006).

Other mechanisms can also cause or enhance outflows like **radiation pressure** from young stars acting on dust (Hopkins et al., 2011), self-gravitating disks and turbulence (Sur et al., 2016), among others. Feedback from radiation pressure provides us with useful scaling outflow properties that have been explored using a variety of wind models. The most relevant scaling is that wind speed scales with circular velocity (Chisholm et al., 2015) while the total mass ejected per star formation unit (mass-loading factor η) scales with the inverse velocity (Heckman & Thompson, 2017). In the resulting **momentum-driven large-scale galactic winds** model (Murray et al., 2005) dust is collisionally coupled to gas, and UV radiation from massive stars accelerates dust to drive galactic winds. One theoretical advantage of doing this is that the available energy budget is higher than the supernovae driven wind model.

In the EAGLE cosmological hydrodynamical simulations (Schaye et al., 2015), both feedback from massive stars and AGN are implemented by injecting thermal energy (Crain et al., 2015). This allows the simulation to form outflows via pressure gradients avoiding the need of specifying their velocity, v, and mass loading η, with respect to the star formation rate, which in summary says that there's no need to add extra parameters.

A similar approach is taken by many "zoom" simulations which model a small number of galaxies at higher resolution (Christensen et al., 2016). However the resulting outflows are then strongly resolution-dependent (Pontzen & Governato, 2014) showing that this approach, while attractive, does not solve the fundamental difficulties with modelling outflows.

The novel hydrodynamic algorithm AREPO (Springel, 2010) models stellar feedback with the kinetic wind scheme. This model requires a velocity scaling and a mass loading value from energy conservation, with the assumption that this energy is generated by Type II supernova. Additionally, for the metal-loading scheme they regulate the enrichment such that 40% of the local interstellar medium metals are ejected by supernova-driven galactic winds. The Illustris simulation employ the AREPO code which evolves the equations of continuum hydrodynamics coupled with self-gravity (Nelson et al., 2015). In Torrey et al. (2015) the mock spectra and images at $z = 0$ from the Illustris simulation are able to reflect stellar metallicity and SFR history of the galaxies. The Illustris simulation (Vogelsberger et al., 2014) provides a framework that allow galaxies to regulate their stellar mass. Then, it is possible to use that framework on large-scale hydrodynamical simulations. The feedback prescription corresponds to a model for star formation and AGN driven winds. This feedback model is able to regulate galaxy populations (Torrey et al., 2014) that match a wide range of observable properties.

Overall, cosmological simulations that study the cosmic metal distribution do not focus on the exact wind-driving mechanism because it is never fully resolved. The most relevant outcome is therefore how the wind properties scale with properties of the host galaxy, regardless of the assumed underlying mechanism (Torrey et al., 2014).

Matching observations with simulations

One of the main aims when simulating galaxies with outflows is to be able to match the properties of stellar, gas and metal content since they are observable quantities (Oppenheimer & Davé, 2008). For instance, some useful results from simulating outflows, with the momentum-driven outflow model (Davé et al., 2011a), show that the production of metal tracers (e.g. C, O, Si, Fe) comes from SNe (Type II) at all redshifts. At redshift *zero*, massive stars (type AGB) moderately contribute to enriching the IGM supplying fresh enriched gas (Cen & Ostriker, 2006). This fraction of gas helps recycling gas into stars which in turn increases star-formation at later epochs. At low-redshift ($z < 1$), enrichment of the intracluster gas seem to be originated by SNe (Type I). Scalings predicted by

this model actually fit a variety of observed quasar absorption lines in the IGM (Murray et al., 2005) while reproducing the observed cosmic star formation history at redshift $1.5 < z < 6$ (Oppenheimer & Davé, 2006). It is broadly consistent with direct observations and seems to match observations of large- scale enrichment. Outflows with similar scalings are able to match the mass-metallicity relation at $z = 2$, to reproduce qualitatively the stellar mass function below M^* at $z = 0$, the kinematics of damped Lyα absorber-Mannucci et al. (2010)., and others. The wind velocity ($v_{\rm wind}$) generated by this model scales with the velocity dispersion of a galaxy (σ), $v_{\rm wind} \propto \sigma$, and with the mass loading factor (η) (i.e. the mass loss rate in winds relative to the star formation rate), $\eta \propto \sigma^{-1}$. Observations (Martin, 2005; Rupke et al., 2005) show that the circular velocity (and therefore the velocity dispersion as $v_{\rm circ} \sim \sigma$) of the galaxy scales with the velocity of the wind over a wide range of galaxies.

A general result from simulations is that wind recycling dominates over expelling gas permanently (Christensen et al., 2016). This result could work to explain galactic fountains where galaxies at low redshift constantly expel ISM gas into the halo but no further. Material from fountains typically returns to the disk on timescales of ≤ 1 Gyr (Fraternali, 2017). Overall, this ejection and accretion of gas between the galaxy and the IGM suggest that they might evolve together continually exchanging mass, energy and metals.

It is possible to estimate the distance that outflows travel out of the host galaxy (R $\approx$ 100 kpc). This distance is dependant on the galaxy mass and redshift, but approximately matches constrains from e.g. Bordoloi et al. (2014).

Outstanding problems in understanding outflows

Estimations of the total outflow mass is difficult to obtain due to its multi-phase nature. In particular, estimates of the mass of the cool gas fraction (usually traced by Na lines in the spectra of star-forming galaxies) present large uncertainties. Surveys show that the momentum of the cold gas is less than the momentum of the hot gas (Rupke et al., 2005), which also leads to kinetic energies much smaller than the energy released from SNe. This means that only a small fraction of the energy released from SNe and massive stars is transferred to galactic winds (Fujita et al., 2009).

Outflows are necessary in simulations to avoid excess of stellar masses (M_*) and very high star formation rates. Davé et al. (2011b) examine the stellar content of galaxies in the presence of outflows with cosmological simulations. These simulations fail at matching key properties (e.g. stellar, gas and metal content) of galaxies at high and low masses.

This indicates that although models are able to reproduce some of the observations, there is additional physics required even for the most successful model. However, they are consistent with the key observations of the scaling relations between stars, gas and metals for star-forming galaxies (Davé et al., 2011a), which dominate cosmic star formation. The main problem when modelling galactic outflows in a cosmological context is that even when computational power has improved in the past years, the resolution limit needed to model outflows feedback energy from supernovae and massive stars is still out of the actual computational possibilities. In simulations like the Eagle simulations, galactic winds appear ubiquitous in all galaxies, and, it is still hard to correlate the outflowing activity with the galaxy properties when comparing to observations.

It has been very challenging to model the highly efficient cooling within the interstellar medium (ISM). Usually, to model supernova in simulations thermal energy is added to the medium. Direct modelling of supernova within a galaxy scale simulation is impossible with the current computational resources (Cen & Chisari, 2011; Creasey et al., 2015).

Material at 10^4 K entrained in a hot outflow is the most difficult to model theoretically. It is not very clear whether they are cold clouds accelerated by hot winds or if they are formed directly from the cooling of hot gas in the halo. Simulations show that the picture of a cloud travelling along the direction of flow is very unstable. Interaction of the gas with the surrounds cause them to shred before they are significantly accelerated (Scannapieco & Brüggen, 2015).

Chapter 3 | *Computational methods*

"It's not good enough to imitate the models proposed for us that are answers to circumstances other than our own. It isn't even enough to discover who we are. We have to invent ourselves."

- Rosario Castellanos, *Mexican poet and author*

Numerical simulations are often the only tool to study theoretical predictions in cosmology. Direct simulation of the physical processes involved in the formation of structure implies intricate integrations that are time-consuming because astrophysical phenomena involve a wide range of scales and highly non-linear physics.

Physical properties such as density and temperatures in the intergalactic gas, in galaxy clusters, superclusters and voids are hard to determine directly from observations. Therefore simulations are crucial tools to compare predictions from theories of formation structure with observations of the local and high-redshift Universe. The mechanisms that cool gas and allow it to form stars, among other processes, must be included when modelling the Universe for this purpose.

3.1 The underlying physics

In general, numerical studies solve the equations of gravity, gas dynamics and radiative processes in a system. The gas component (typically approximated as an ideal fluid) is modelled as a continuum medium by solving the fluid equations using finite difference methods. In this section I present the equations of physics that any code will solve to model astrophysics phenomena.

Basic equations

The motion of fluids is described by the hydrodynamic equations; which arise from the conservation of mass, momentum and energy:

$$\frac{\partial \rho}{\partial t} + \nabla \cdot (\rho u) = 0, \tag{3.1}$$

$$\frac{\partial u}{\partial t} + (u \cdot \nabla)u = -\Big(\nabla\Phi + \frac{\nabla P}{\rho}\Big), \tag{3.2}$$

$$\frac{\partial}{\partial t}\left[\rho\Big(\frac{u^2}{2} + e\Big)\right] + \nabla \cdot \left[\rho\Big(\frac{u^2}{2} + \frac{P}{\rho} + e\Big)u\right] - \rho u \cdot \nabla\Phi = \mathscr{H} - \mathscr{C}, \tag{3.3}$$

where u, ρ, e, P are velocity, density, specific internal energy and pressure respectively and $\mathscr{H} - \mathscr{C}$ are the heating and cooling rates per unit volume (Clarke & Carswell, 2014; Mo et al., 2010).

The gravitational potential, Φ, is a solution to the Poisson equation

$$\nabla^2\Phi = 4\pi G\rho_{\rm tot}, \tag{3.4}$$

where G is the gravitational constant and $\rho_{\rm tot}$ is the total mass density.

Radiative cooling

Radiative cooling occurs due to two-body processes. i.e., the system loses energy through radiation due to two-body interactions such as free-free emissivity, collisional ionisation, recombination, collisional excitation. In general, the cooling rate is the sum over all ion species whether it arises from primordial gas or other ion species. However, due to their abundance, hydrogen and helium often dominate except at high metallicities. These radiative processes depend strongly on temperature, with temperatures in the range 10^2 K $< T < 10^8$ K (Mo et al., 2010; Katz et al., 1996):

- At high temperatures, gas is highly ionised making electrons decelerate when encountering atomic nuclei. In this regime, gas is optically thin and the radiative cooling is dominated by free-free emissivity (also known as "bremsstrahlung").
- When temperatures are somewhat lower, in the temperature range 10^4 K $< T_{\rm vir} < 10^6$ K, radiative cooling is dominated by collisional excitation. Atoms can be excited by a collision with another particle.
- A subdominant contribution at all temperatures comes from recombination; an electron combines with an ion, emitting a photon.
- At lower temperatures still, the main channel is collisional excitation; collisions from electrons excite atoms and then decay radiatively to the ground state.

Since the gas is typically optically thin, most simulations assume that the emitted photons in this cooling process can escape easily. Given the temperature T of a gas, the cooling rates can be represented as

$$\Lambda(T) \equiv \frac{\dot{Q}_{\rm cool}}{n_{\rm H}^2}, \tag{3.5}$$

where $\dot{Q}_{\rm cool}$ is the cooling rate per unit volume and $n_{\rm H}$ is the hydrogen density atoms in both neutral and ionised states.

Ionisation balance and heating

To calculate cooling rates quantitatively requires knowing the ionisation state of the gas. Atoms can be ionised by collisions at sufficiently high temperatures, or by the presence of a UV background of photons from galaxies and quasars (Haardt & Madau, 1996). Establishing ionisation equilibrium is normally very fast compared to cooling and gravitational timescales. Thus the cooling functions are calculated assuming ionisation equilibrium i.e. the densities of all ions are equal to their equilibrium values. When photoionisation takes place, the electrons released have kinetic energy from the incoming photon and hence provide the heating term ($\mathscr{H}$) in Eq. (3.3).

3.1.1 Cooling and heating rates

In this thesis we use primordial radiative cooling modelled with cooling curves from Katz et al. (1996). When gas shocks and heats, it converts kinetic energy into thermal energy. Then, gas cools by expansion.

As mentioned above, radiative cooling of primordial composition is computed using two-body processes. Figure 3.1 shows the cooling and heating curves in the presence of a photoionising background consistent with a density of quasars at redshift $z \sim 2$ (Katz et al., 1996). Both panels show the net cooling rate (heavy solid line) and contribution from other processes such as recombination (long dashed line), free-free (thin solid line), collisional excitation (short dashed line) and collisional ionisation (dotted line). The two panels have different gas densities; on the left panel $n_{\rm H} = 2.89 \times 10^{-6}$ cm^{-3} and the right panel $n_{\rm H} = 2.89 \times 10^{-3}$ cm^{-3}. In this system, H and He are completely photoionised at all temperatures.

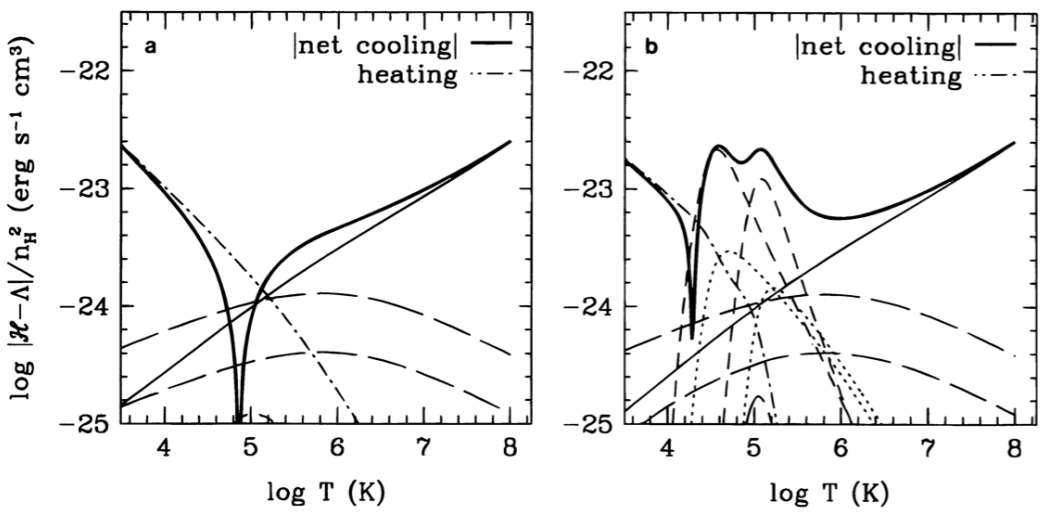

Figure 3.1: Cooling rates for a primordial composition gas (Katz et al., 1996). The cooling curves are shown as a function of temperature with a UV radiation background. Gas density $n_{\rm H} = 2.89 \times 10^{-6}$ cm^{-3} (left) and $n_{\rm H} = 2.89 \times 10^{-3}$ cm^{-3} (right). The dot-dashed line shows the heating rate by photoionisation. The plot shows how heating dominates at low temperatures and cooling at high temperatures. The black solid line shows the absolute value of the net cooling rates. Other processes are denoted as follows: recombination (long-dashed line), free-free (thin solid line), collisional excitation (short-dashed line) and collisional ionisation (dotted line). More details about these cooling curves are found in Katz et al. (1996).

For the purpose of this thesis, cooling effects will be included as they change the gas state in the galaxy haloes when modelling its dynamics as shocks traverse.

3.2 Structure

In this section, I summarise the basic principles of the main schemes that are used in typical simulation codes such as RAMSES (Teyssier, 2002), GADGET (Springel, 2005) and ENZO (Bryan et al., 2014). Computational methods must be implemented both to solve the dynamics of continuum media and to determine the gravitational forces in a system

of N particles. Codes used to solve astrophysical systems will evolve three-dimensional self-gravitating fluids both with and without additional collisionless matter (Hernquist & Katz, 1989), contributed by stars and dark matter.

3.2.1 Hydrodynamical methods

Cosmological codes currently available generally use hydrodynamical methods that are divided into Eulerian and Lagrangian categories. The difference between the two methods lies in the conceptual approach. Eulerian and Lagrangian formulations (Clarke & Carswell, 2014) are two entirely different ways of simulating fluid dynamical problems on a computer with advantages and disadvantages to each, as I will now describe.

Eulerian schemes

Methods on the Eulerian description set up a grid of stationary boxes to represent the spatial position, then compute the changes of all measurable quantities (i.e. ρ, P, T, etc) in each box as a function of time using finite-difference approximations to derivatives. Mesh-based codes may include algorithms with a fixed mesh or adaptive mesh. The advantage of Eulerian simulations is that they naturally capture many fluid phenomena such as instabilities and, especially, shocks. However, the fact that the grid is fixed in space implies that the resulting simulation is not "Galilean-invariant" i.e. the effects of resolution will be different depending on the speed that the fluid flows relative to the grid.

Cosmological simulations require us to model high dynamic ranges for which static meshes are poorly suited. For instance, individual galaxies would be poorly resolved even with very large meshes, and including internal structure such as star and galaxy formation represents a big challenge (Kang et al., 2005). Adaptive Mesh Refinement (AMR, Berger & Oliger, 1984) is an Eulerian hydrodynamics scheme that dynamically adjusts the grid to overcome this limitation. It locally refines patches of the domain in space and time in order to resolve with high-resolution regions of particular interest such as a galaxy or other high density feature.

Lagrangian schemes

Lagrangian codes offer a different set of resolution limitations compared to grid-based codes. They represent fluid elements with a system of particles to follow their trajectories

in the flow.

Smoothed-particle hydrodynamics (SPH; Gingold & Monaghan, 1977) is a Lagrangian representation that models the dynamics of continuum media as a collection of N fluid elements. Fluid elements are typically represented by fixed-mass particles, meaning that the particle number density is proportional to the mass density of the fluid ρ. Almost all currently available Lagrangian codes employ SPH (Weinberg et al., 1997; Springel, 2005) but they are not the only option. One main disadvantage for using SPH is that shocks are represented with an artificial viscosity which impose restrictions on the local spatial resolution.

Since this thesis is largely concerned with shocks and instabilities, AMR is a more natural choice and will be used in Chapter 4. SPH is described here only for completeness.

Intermediate schemes attempt to combine the best of Lagrangian and Eulerian techniques e.g. AREPO (Springel, 2010), which is a cosmological hydrodynamical simulation code on a fully dynamic unstructured mesh. However, these are relatively new and do not offer advantages over AMR for the work in this thesis.

3.2.2 Gravity solving methods

Gravitational interactions are computed with N-body methods divided into four methods (Anninos et al., 1994):

- Particle-Particle (PP; e.g. Aarseth & Fall, 1980)
  PP methods are algorithms that compute the interaction of each particle with every other particle. This method is very accurate for a limited number of particles. It computes the gravitational attraction, in which the acceleration is determined by the direct sum $\mathbf{F}_i = \sum_j Gm_i m_j(\vec{\mathbf{r}_j} - \mathbf{r}_i)/|\mathbf{r}_j - \mathbf{r}_i|^3$. This leads to unphysical two-body scattering when supposedly collisionless tracers (e.g. dark matter or star particles) approach each other closely. Removing this unphysical effect requires "softening" the force law; but since this thesis does not involve collisionless dynamics, we do not consider this issue further.

- Particle-mesh (PM; e.g. Bouchet & Kandrup, 1985)
  PM methods determine the forces of a system of particles by converting the system into a mesh of density values. This method works well even for a large number

of particles. The potential is solved for the density grid and forces applied to individual particles will depend on what cell the particle is in. Typically there must be smaller number of grid cells than number of particles to obtain significant speed improvements over PP. However, PM algorithms consequently have limited resolution since forces on any particle are interpolated from the density grid.

- Particle-Particle-Particle-Mesh (P^3M; e.g. Efstathiou et al., 1985)
  P^3M combines the PM method for interactions of particles separated by long distances and PP for interactions of particles close to each other. In the best case scenario, this is both fast and accurate. However, in practice the algorithm can be time expensive because in the case of extreme clustering PP interactions will dominate the calculations. RAMSES nonetheless uses P^3M because its mesh is naturally adaptive (see below).

- Tree codes (the Barnes-Hut method; Barnes & Hut, 1986)
  Tree algorithms reduce the number of computations resulting in faster algorithms. They do not require a discrete mesh but instead work on hierarchical subdivision of space. Each volume is subdivided in equal volume subunits (in three dimensions it would be eight subunits, i.e., oct-tree) then each volume will be divided recursively until each subcell contains either one or none particles. To calculate the force on each particle, close particles will be accounted for and far away cells (quadrants/octants) will be approximated by the centre of mass. The force on a given particle is determined by going down the tree starting from the largest volume. This allows the forces from distant regions to be approximated while forces from nearby regions are progressively more accurate until, for the nearest particles, they are again calculated by PP evaluation. In this way a tree solver is rather like a P^3M solver but without a fixed resolution, which avoids the difficulties arising when clustering is strong.

3.2.3 TreeSPH: Hydrodynamics + Gravity

The TreeSPH method (Hernquist & Katz, 1989) comes as a natural algorithm that pairs up a tree gravity with SPH hydrodynamics, it is used e.g. by GADGET (Springel, 2005). It works as a general-purpose code for evolving three-dimensional self-gravitating fluids, both with and without collisionless matter. Tree algorithms are a gridless method,

to approximate the potential of distant groups of particles, that can be paired with a Lagrangian framework such as SPH. The pairing is natural because the way data is structured in the gravity tree can be applied directly to aspects of the SPH hydrodynamics, specifically to efficiently finding neighbour particles to calculate densities and pressures.

3.2.4 P^3M + AMR: RAMSES overview

Conversely it is natural when using AMR simulations to use a mesh based (i.e., a P^3M-type) gravity solver, since grids already exist. When the grids are adaptively refined, the worst problems of P^3M are avoided because the grid spacing is naturally adapted to the level of clustering. In this respect, RAMSES operates slightly like a tree-based algorithm, but fundamentally the gravity solution is still calculated on grids.

In this thesis, I used the package RAMSES, to study the gas dynamics of outflows traveling the halo in small-size galaxies. In the remainder of this chapter, I describe relevant details of the code. RAMSES is a tree-based Eulerian AMR hydrodynamics code (Teyssier, 2002). It is highly flexible in allowing customised initial and boundary conditions to set the computational domain. The Poisson equation is solved using a multigrid method to solve for the potential Φ, although in our case we also add a fixed external potential as discussed in Chap. 4. The Euler equations 3.1 – 3.3 are integrated using a Riemann solver (Toro et al., 1994).

Initial and boundary conditions

Initial conditions in RAMSES are defined by providing a user routine that evaluates the starting properties, such as ρ, P and T, as a function of position. Boundary conditions in RAMSES are defined in a temporary buffer region surrounding the computational domain (ghost regions). The default setting corresponds to a periodic box (variables must be chosen to specify in order the effect of the type of boundary: periodic, reflexive, outflow, inflow). However this can be easily changed by passing suitable parameters to the code. Both customisations are essential for the work in Chap. 4.

Chapter 4

Bursty star formation feedback and cooling outflows

"The underlying physical laws necessary for the mathematical theory of a large part of physics and the whole of chemistry are thus completely known, and the difficulty is only that the exact application of these laws leads to equations much too complicated to be soluble."

- Paul Dirac

The content in this chapter have been published in Monthly Notices of the Royal Astronomical Society (MNRAS) as Suarez et al. (2016).

4.1 Introduction

Star-forming galaxies are surrounded by gas (known as the circumgalactic medium, CGM) with a comparable total mass to their stellar mass (Werk et al., 2014). This gas is enriched by metals that were almost certainly ejected from the galaxy; outflows, carrying a mass comparable to the mass of star-forming regions, are ubiquitously observed in star forming galaxies in the local universe (Erb, 2015), at intermediate redshifts $z \sim 0.5$ (Rubin et al., 2010; Nielsen et al., 2013; Bordoloi et al., 2014) and at high redshifts of $z \sim 6$ (Ajiki et al., 2002; Martin, 2005). The interrelationship between inflow and outflow is critical to the behaviour of galaxies as a whole, as it reshapes quantities such as the stellar mass function (Dekel & Silk, 1986; Oppenheimer et al., 2010) and mass-metallicity relation (Finlator & Davé, 2008). Baryon cycling through the CGM likely also plays a role in controlling the distribution of dark matter (Pontzen et al., 2015).

The mechanism behind outflows is uncertain and may relate to some combination of supernova feedback (Governato et al., 2010), winds of high-mass stars (Martin, 1999; Dalla Vecchia & Schaye, 2008) and active galactic nuclei (AGN) (Nesvadba et al., 2008). Dwarf galaxies are of particular interest since their small black hole masses makes AGN feedback ineffective, so that the outflows are almost certainly linked directly to star formation feedback. Additionally the higher gas-to-stellar-mass fraction combined with the shallow gravitational potential allow outflows to easily release material to the CGM (Peeples et al., 2014). Observations in this low-mass regime have shown evidence of C IV absorption in the CGM out to 100 kpc. Therefore, these galaxies are useful case studies of the connection between the CGM and the host galaxy.

Galactic outflows seem to possess a multi-phase nature, spanning several orders of magnitude in temperature (Werk et al., 2014). There is a particular puzzle over how cold gas material could survive in galactic outflows if they are entrained in a hot flow (e.g., Veilleux et al., 2005; Scannapieco & Brüggen, 2015; Zhang et al., 2017). Perhaps this implies that cold gas can be directly accelerated using radiation pressure (Murray et al., 2005; Hopkins et al., 2012). The lifetime of cold clouds is, however, dependent on physical assumptions and simulation methods meaning that robust conclusions are difficult to draw. Another scenario is that the cooler phases of the outflow are actually formed in situ by radiative cooling (e.g., Efstathiou, 2000; Martin et al., 2015); recently, detailed analytic discussions in support of this possibility have been given by Thompson et al. (2016) and Bustard et al. (2016).

In this paper, we study the formation of cool gas in outflows in a different way. Instead of developing analytic solutions to the outflow problem we inject hot gas into a idealised galaxy halo with a fixed potential. The numerical setup is similar to that of Mac Low & Ferrara (1999) but introduces a simple prescription to deliver the outflow in discrete bursts. While our setup is highly simplified, we use it to argue that the balance between hot and cooler gas will be affected by the duty cycle of star formation. Such a link introduces a new dimension to the relationship between outflows and the evolution of a galaxy, raising the possibility that the relative abundance of different observed ions reflects information about the detailed star formation history. Since it is specifically *bursty* star formation that can have a profound impact on dark matter and stellar dynamics (Pontzen & Governato, 2014), cross-checking typical star formation patterns in the observed universe would be a valuable additional benefit to studies of the CGM. The

simulations are two-dimensional, allowing us to run a much larger parameter study than would be possible in a three-dimensional study.

This paper is organised as follows. In Sec. 4.2 we explain the initial and boundary conditions to simulate outflows in galaxies using RAMSES (Teyssier, 2002). We discuss the results in Sec. 4.3. Finally, we summarise in Sec. 6.5.

4.2 Hydrodynamical Simulations

Our aim is to run a series of simulations that track how gas ejected from the disk of a galaxy interacts with halo gas out to the virial radius using RAMSES, a tree-based adaptive mesh refinement (AMR) hydrodynamical code. We set up an idealised equilibrium halo, then inject hot outflows at the bottom of the computational box according to different models. To allow us to probe a large number of different scenarios we use 2-dimensional simulations.

In Fig. 4.1 we show a schematic representation of the CGM box in RAMSES. The galaxy is notionally positioned $d_{\rm gal} = 1\,{\rm kpc}$ below the bottom of the box and it is not part of our simulations. Instead, we assume hot gas from supernovae and other stellar feedback processes is expelled by the galaxy according to parameters that are described in Sec. 4.2.2. The lateral and top sides of the box are chosen to satisfy *outflow* conditions, meaning that RAMSES sets gradients across them to zero. This way we allow gas to flow outside the box into the intergalactic medium (IGM).

For simplicity of setting up an equilibrium halo (which we discuss further in Sec. 4.2.1), we assume a plane-parallel configuration so that the gravity is everywhere in a downwards direction. We assume a fixed gravitational field g corresponding to that of a Navarro−Frenk−White (NFW) dark matter halo, but directed along the $\hat{\vec{y}}$ direction. This gives us a force law

$$g = -\frac{4\pi G\rho_0 r_s^3}{y^2}\left[\log\left(\frac{y+r_s}{r_s}\right) - \frac{y}{y+r_s}\right], \tag{4.1}$$

where ρ_0 and r_s are the scale density and radius of the NFW profile respectively. It will help to define the virial radius r_{200} which is the radius containing a mean density 200 times that of the cosmological critical value. Our focus is on dwarf galaxies for the reasons outlined in the introduction; accordingly we use a halo with virial velocity $v_{200} = 50\,{\rm km\,s^{-1}}$, giving a virial radius $r_{200} \simeq 140(1+z)^{-3/2}\,{\rm kpc}$ and virial mass

$M_{200} \simeq 8 \times 10^{10}\,(1+z)^{-3/2}\,\mathrm{M}_\odot$. We adopt the scale radius $r_s = 5$ kpc from the fit given by Macciò et al. (2007).

The mesh in RAMSES is defined on a recursively refined spatial tree. We set the maximum level of refinement to 10, which means that the regular Cartesian grid is continuously refined in the course of the simulation by a factor of up to $2^{10} = 1024$; our box size of $80\,\mathrm{kpc}$ therefore allows for a maximum resolution of $80\,\mathrm{pc}$. We ran a convergence test with higher resolution on one case, reaching $40\,\mathrm{pc}$ by increasing the maximum refinement to 11, finding that the results that we describe below did not change. The refinement strategy opens a new cell if the discontinuity in density or pressure is above 5 per cent; for time stepping we adopted a Courant number of 0.6.

4.2.1 Initial conditions: equilibrium inflow

We modified the RAMSES code in order to set up equilibrium, inflowing (or hydrostatic) gas in our fixed potential to represent the halo and to inject hot gas in the bottom. Here we discuss the initial equilibrium, then discuss the injection method in Sec. 4.2.2.

We ran simulations both with and without cooling. While a hydrostatic solution is an attractive initial stable state in terms of its simplicity, there are no such solutions when cooling is enabled. Therefore we always consider inflowing gas. The first fluid motion equation enforces mass conservation so that for any region the rate of change of its mass is the net flow of mass into it:

$$\frac{\partial \rho}{\partial t} + \rho \frac{\partial u}{\partial y} + u \frac{\partial \rho}{\partial y} = 0, \tag{4.2}$$

where $\rho(y)$ is the density, $u(y)$ is the velocity in the y direction, and t denotes time. The momentum-conservation equation ensures the rate of change of momentum is balanced by momentum flow and net force:

$$\rho \frac{\partial u}{\partial t} + \rho u \frac{\partial u}{\partial y} = -\frac{\partial p}{\partial y} - \rho g, \tag{4.3}$$

where p is the pressure. Finally we have the energy conservation equation:

$$\frac{\partial E}{\partial t} + \frac{\partial}{\partial y}[(E+p)u] = -\rho \dot{Q}_{\mathrm{cool}} + \rho \frac{\partial \Phi}{\partial t}, \tag{4.4}$$

where $E = \rho(\epsilon + u^2/2 + \Phi)$ refers to the energy per unit volume, ϵ is the internal energy per unit mass, Φ is the potential implied by Eq. (4.1), and the cooling function is defined by $\dot{Q}_{\mathrm{cool}}(\rho, T)$ per unit mass. We substitute for the internal energy

$$\epsilon = \frac{3kT}{2\mu m_p}, \tag{4.5}$$

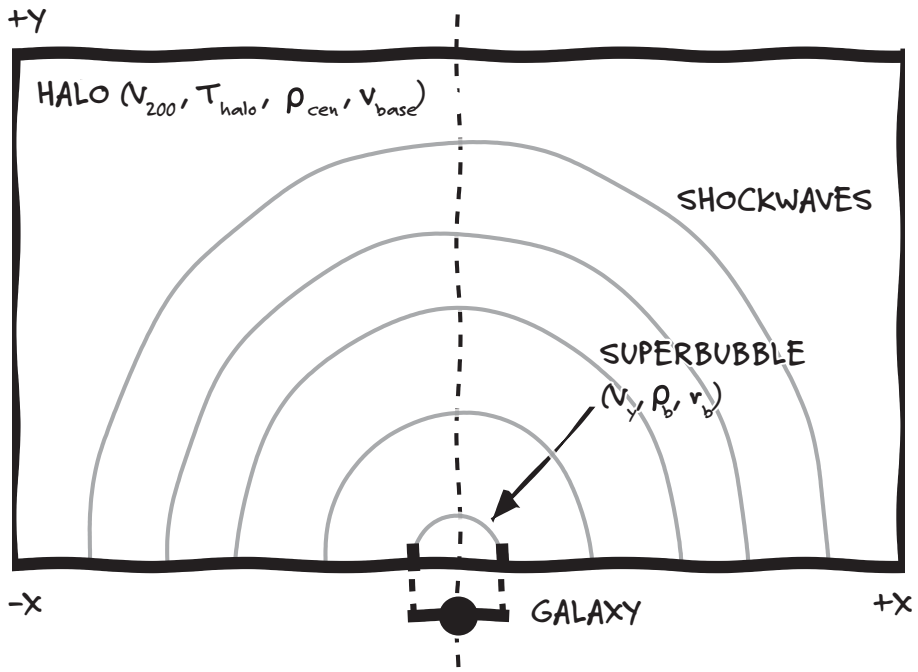

Figure 4.1: A schematic representation of the two-dimensional set-up of our simulation. In our model, gas is assumed to flow into the box along the lower edge i.e., at $\mathrm{y} = 0$, and flow out of the box along each of the remaining three edges. We model half the halo with a radius of approximately $100\ \mathrm{kpc}$. The superbubble is referred to a starburst-type galaxy that is not part of the simulation. The physical properties of the gas expelled by the galaxy determine the boundary conditions in our simulations such as $\mathrm{r_b} \sim 4\ \mathrm{kpc}$, $\mathrm{v_y} \sim 400\ \mathrm{km\,s^{-1}}$, and a density $\rho_\mathrm{b} \sim 0.05\rho_\mathrm{cen}$, as well as the ghost regions that delimit the box. The physical properties of the halo such as $\mathrm{v_{200}}$, $\mathrm{T_{halo}}$, ρ_cen and $\mathrm{v_{base}}$ determine the initial conditions.

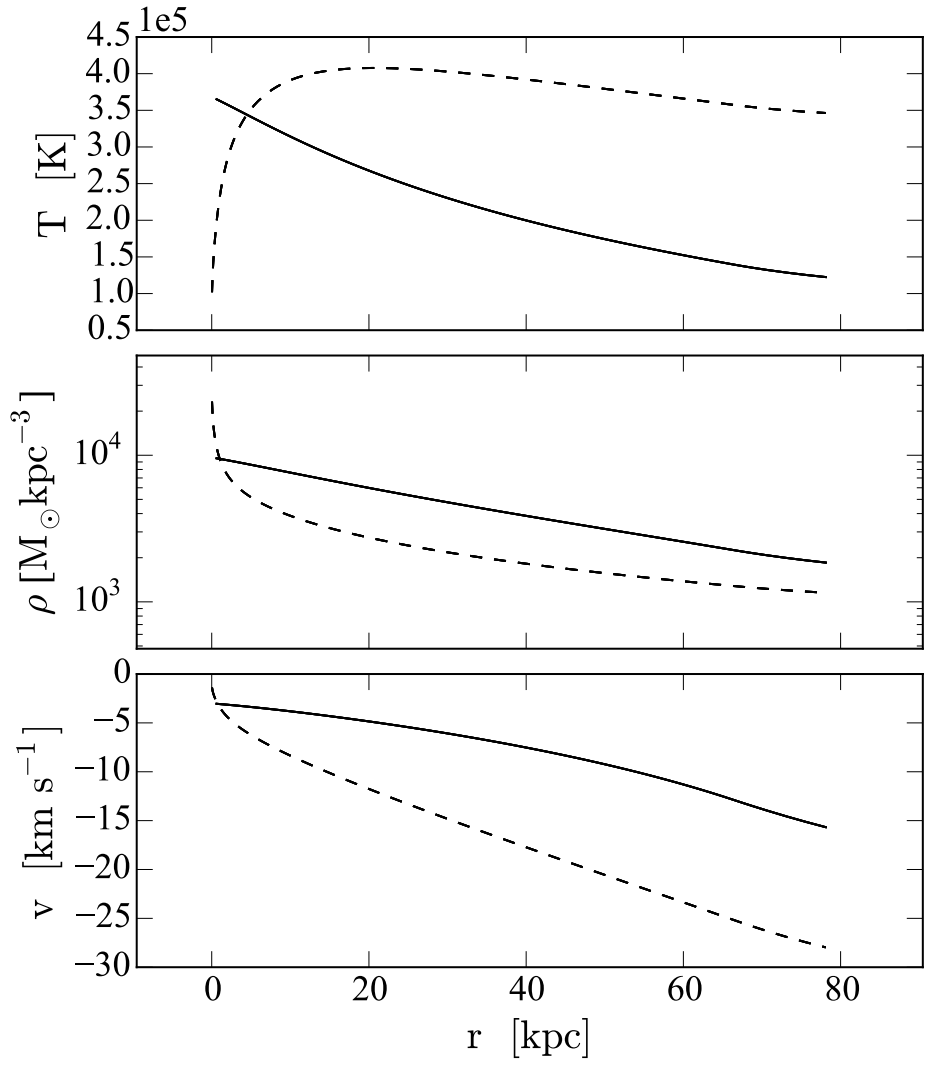

Figure 4.2: Equilibrium inflow conditions that we adopted as a function of height. These are obtained by solving Eqs. (4.7), (4.8) and (4.9). The solid line represents the adopted solution for adiabatic runs (i.e., $\dot{Q}_{\rm cool} = 0$). The solution when cooling is activated is represented by the dashed lines.

where k is the Boltzmann constant, m_p is the proton mass, and μ is the mean molecular weight of the gas constituents. We assume a primordial gas for our background solution, and furthermore that μ is constant (i.e., the ionisation is fixed), and check that this assumption holds by ensuring the resulting initial conditions are stable over many sound-crossing times.

To obtain the equilibrium halo solution, we then set all partial derivatives with respect to t to be zero. Overall, once simplified using Eq. (4.2), the energy equation, Eq. (4.4),

becomes

$$u\frac{\partial u}{\partial y}+\frac{5k}{2\mu m_p}\frac{\partial T}{\partial y}=g-\frac{\dot{Q}_{\rm cool}}{u}. \tag{4.6}$$

Finally we solve the three equations above for $\partial u/\partial y,\ \partial\rho/\partial y$ and $\partial T/\partial y$:

$$\frac{\partial u}{\partial y}=\frac{-2\dot{Q}_{\rm cool}+3gu}{-5\tilde{R}T+3u^2}\,, \tag{4.7}$$

$$\frac{\partial \rho}{\partial y}=-\frac{\rho}{u}\frac{\partial u}{\partial y} \quad \text{and} \tag{4.8}$$

$$\frac{\partial T}{\partial y}=2\,\frac{(\dot{Q}_{\rm cool}/u)\tilde{R}T+g\tilde{R}T-\dot{Q}_{\rm cool}u}{k(-5\tilde{R}T+3u^2)}, \tag{4.9}$$

where $\tilde{R}=k/\mu m_p$. Note that the denominator can cross zero, corresponding to a shock in the inflow solution, but by studying only low mass galaxies we do not suffer from this potential problem (Rees & Ostriker, 1977). We used Eqs. (4.7) – (4.9) in conjunction with a numerical Runge-Kutta integrator to obtain initial conditions.

We required two solutions: one for the adiabatic case when we set $\dot{Q}_{\rm cool}=0$ and the other for cooling simulations. In the latter case we obtain $\dot{Q}_{\rm cool}$ from the RAMSES cooling function assuming primordial gas composition and a UV background fixed to the Haardt & Madau (2012) normalisation at $z=2$. At lower redshifts, metal enrichment and a reduced UV background would lead to faster cooling. Therefore our results will give a lower bracket for the amounts of cool gas that can be generated in outflows.

We have freedom in imposing conditions $\rho(0)$, $u(0)$ and $T(0)$ (i.e., the density, velocity and temperature $1\,\mathrm{kpc}$ above the notional galaxy). Our primary criteria for choosing these was to obtain a circumgalactic medium with (i) a density of around $10^4\ M_\odot\,\mathrm{kpc}^{-3}$ at $y=0$ reducing to around $10^3\ M_\odot\,\mathrm{kpc}^{-3}$ at the virial radius; (ii) an overall temperature of around 3×10^5 K; (iii) a small inflow velocity $\lesssim 5\ \mathrm{km\,s^{-1}}$ at the base of the box. These choices were motivated by the inflowing component of the circumgalactic medium of the cosmological zoom simulation DG1 from Pontzen & Governato (2012).

Achieving these goals requires a different solution for the adiabatic and cooling cases. Figure 4.2 shows the two solutions as respectively a dashed and solid line, illustrating (from top to bottom) the temperature (T), density (ρ) and velocity (u). Both solutions have similar, but not identical, initial conditions in these three physical properties. We tuned the initial conditions by hand to find solutions as similar as possible between the two cases.

For instance, the initial gas temperature in the adiabatic case is ~ 3 times hotter at the

Quantity	Values (cooling)	Values (adiabatic)
$T_{\rm base}$	6×10^4 K	3×10^5 K
$\rho_{\rm base}$	10^{-3} amu cm^{-3}	3×10^{-4} amu cm^{-3}
	= 2.5×10^4 M$_\odot$ kpc^{-3}	= 7.4×10^3 M$_\odot$ kpc^{-3}
$v_{\rm base}$	2 km s^{-1}	3 km s^{-1}
$r_{\rm b}$	4 kpc	
$\rho_{\rm b}/\rho_{\rm base}$	$0.02/f_{\rm cyc}$ (maintaining $\dot{M}_{\rm av}$)	
$v_{\rm y}$	400 km s^{-1}	
$t_{\rm cyc}$	Vary between 100 and 3000 Myr	
$f_{\rm cyc}$	Vary between 0.033 and 1	

Table 4.1: Parameters describing initial and boundary conditions for the models, motivated by matching onto existing ab initio galaxy simulations as explained in the text. The steady-state background inflow solutions are determined by the first three parameters and vary between cooling and non-cooling simulations to better match the mean properties of the halos. Instantaneous properties of the "bubble" emerging into the bottom of our box are given by the next three parameters. The final two parameters, $f_{\rm cyc}$ and $t_{\rm cyc}$, describe the cycle of outflow activity. To keep the time-averaged outflow rate $\dot{M}_{\rm av}$ the same between simulations, ρ_b is allowed to depend on $f_{\rm cyc}$.

bottom of the box but 2 times cooler at higher radii than in the cooling case. However this is an acceptable compromise, given the non-linear nature of these equations, we do not expect to find solutions that closely match each other in all three parameters. The biggest difference between solutions is observed in the temperature, which drops rapidly as inflowing gas nears the bottom of the box when cooling is enabled. Overall we found two solutions with similar parameters for the undisturbed CGM, and were able to verify that these were indeed stable by running them for several Gyr in RAMSES.

4.2.2 Outflow characterisation

In the previous section we described the physical properties of inflowing gas, setting our initial conditions. We now consider the boundary conditions which include the properties of the "superbubble" emerging from the galaxy, assuming a single phase outflow

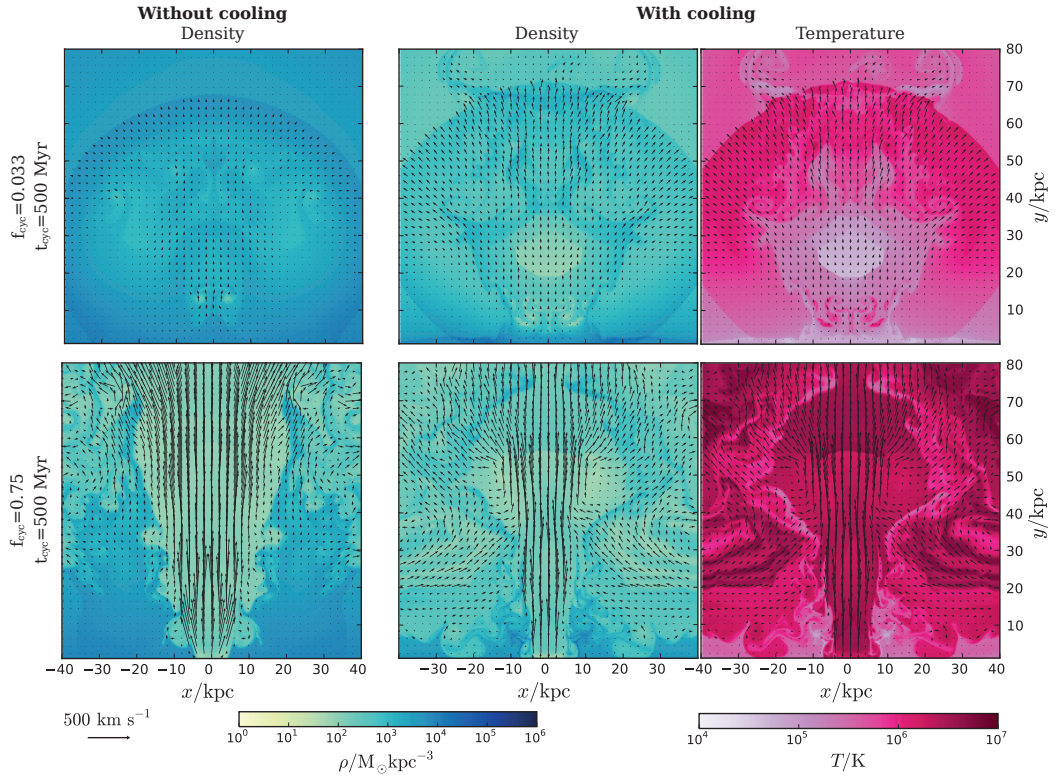

Figure 4.3: Example renderings of our simulations after several Gyr. The top row shows a short duty cycle example with $t_{\rm cyc} = 500$ Myr and $f_{\rm cyc} = 0.033$. The bottom row shows a long duty cycle example with $t_{\rm cyc} = 500$ Myr and $f_{\rm cyc} = 0.75$. From left to right the panels show the density in the non-cooling (adiabatic) simulations, the density with cooling enabled, and the temperature with cooling enabled.

uniformly distributed across a radius of $r_{\rm b}$. The properties of the new hot material are characterised by the radius, the density of the new gas (ρ_b) and its upwards velocity (v_y). The temperature of the superbubble is set for pressure equilibrium so that $p_{\rm b} = p_{\rm base}$, otherwise pressure would cause it to rapidly expand. Since $p \propto \rho T$, the temperature and density of the bubble and inflow are interrelated by $T_{\rm bub}/T_{\rm base} = \rho_{\rm base}/\rho_b$. We assume that the outflow is dominated by a hot phase with $T_{\rm bub} \gg T_{\rm base}$, ignoring any colder material that may have been transported from the disk. While it may be possible to accelerate cold clouds, preventing their disruption over a few scale-lengths is challenging (Scannapieco & Brüggen, 2015) and consequently on large scales, in situ cooling is likely to be a strongly dominant source of cool outflows (Thompson et al., 2016).

The main aim of the current paper is to investigate how in situ cooling changes as the nature of the star formation cycle in the galaxy is altered. To allow us to parameterise this and investigate systematic changes, we define a *cycle length* $t_{\rm cyc}$ and *duty cycle* $f_{\rm cyc}$. The cycle length is the overall time periodicity of the galactic star formation. The duration of the whole simulation is always set for at least five times the cycle length, which means that multiple bubbles are injected. The duty cycle is the fraction of time that the bubble actually spends pumping gas into the halo, so that $f_{\rm cyc} = 0$ implies no bubble is created whereas $f_{\rm cyc} = 1$ means that the galaxy expels gas at all times. Our cycle is deterministic; in this work we have not investigated the modifications that randomness within the duty cycle could introduce.

The two parameters $t_{\rm cyc}$ and $f_{\rm cyc}$ are of particular interest because they characterise a "burstiness" for the star formation; bursts of star formation are also important to determine whether dark matter cusp/core transformations are generated by the outflows (Pontzen & Governato, 2014). In galaxy formation simulations, the burstiness of star formation is strongly affected by the feedback prescription (e.g., Le Bret et al., 2015; Oñorbe et al., 2015). We allow $t_{\rm cyc}$ and $f_{\rm cyc}$ to vary independently in respectively 8 and 5 steps, making a grid of 40 models. The values vary between 100 and 3000 Myr for $t_{\rm cyc}$ and between 0.033 and 1.0 for $f_{\rm cyc}$.

When outflows are being generated, the amount of gas produced per unit time ($\dot{M}_{\rm on}$) is determined by the velocity, the density and the radius of the bubble as

$$\dot{M}_{\rm on} = 2(\pi r_b^2) v_y \rho_b \ , \tag{4.10}$$

where the factor of two arises from assuming outflows to occur in both directions from the disk. In our scheme, the overall outflow rate is also dependent on the time that the

galaxy is expelling gas, i.e., the averaged outflow rate is set by $\dot{M}_{\rm av} = \dot{M}_{\rm on} f_{\rm cyc}$. The total amount of gas expelled by such galaxies is very uncertain, and, because it is too diffuse, halo gas is extremely difficult to observe directly (Werk et al., 2014). We enforce in all our simulations that $\dot{M}_{\rm av} \simeq 0.01\,{\rm M}_\odot\,{\rm yr}^{-1}$, motivated by mass-loading factors of order unity, coupled to low average star formation rates expected for systems of this size (Governato et al., 2010; Christensen et al., 2016). Consequently $\dot{M}_{\rm on}$ must vary as $f_{\rm cyc}$ changes in our simulations. Specifically there is the following relationship between our parameters:

$$\frac{\dot{M}_{\rm av}}{0.01\,{\rm M}_\odot\,{\rm yr}^{-1}} = \frac{v_y}{400\,{\rm km\,s}^{-1}} \frac{\rho_b}{490\ {\rm M}_\odot\,{\rm kpc}^{-3}} \left(\frac{r_b}{4\,{\rm kpc}}\right)^2 f_{\rm cyc}. \tag{4.11}$$

The default parameters here have again been motivated by a study of DG1. We fix the left-hand-side of this relationship but vary $f_{\rm cyc}$, so are forced to change other parameters of the outflow. While there is no unique prescription for this, we chose to fix v_y (so that the outflows are always strongly supersonic) and r_b (because this is limited by the size of the disk), allowing ρ_b to change $\propto f_{\rm cyc}^{-1}$ in compensation. In our most extreme case of $f_{\rm cyc} = 0.033$, $\rho_b \simeq 1.7 \times 10^4\ M_\odot\ kpc^{-3} \simeq 7{\times}10^{-4}\,{\rm amu\,cm}^3 \simeq 0.7\rho_{\rm base}$. Note that there is no dependency on $t_{\rm cyc}$, so that our models at fixed $f_{\rm cyc}$ have identical outflow parameters.

Because the velocities are quite substantial, most of the energy of our bubbles is tied up in kinetic form (even though in the disk, where pressures are substantially higher, the energy may have been thermal). The total energy available from supernova (SN) explosions is dependent on the stellar initial mass function, but is approximately $10^{49}\,{\rm ergs}$ per solar mass of stars formed. The velocity of a wind driven by this energy source is

$$v_y \simeq \sqrt{\epsilon/0.1\eta} \times 300\,{\rm km\,s}^{-1}, \tag{4.12}$$

where ϵ is the fraction of $10^{49}\,{\rm ergs\,M}_\odot^{-1}$ that actually couples and η is the mass-loading factor of the wind, i.e., $\eta = \dot{M}_{av}/\dot{M}_\star$ where $\dot{M}_\star$ is the star formation rate. Our chosen parameters are consistent in the sense that recent simulations find order-unity mass loading η, while adopting values of ϵ that are at least 0.1 and often considerably more (Governato et al., 2010; Hopkins et al., 2014). As we will see in the next section, the typical outflow velocities that would be observed along a random sightline through the halo is normally considerably less than the imposed outflow velocity at the bottom of our box, since the energy is rapidly dispersed in the halo.

We summarise the values of both the initial and bubble conditions in Table 4.1.

4.3 Results

As we explained in Sec. 4.2 and Table 4.1 above, our exploration is based on a 8×5 grid of parameters $t_{\rm cyc}$ and $f_{\rm cyc}$. Note that when $f_{\rm cyc} = 1$, the $t_{\rm cyc}$ parameter has no effect, so we can eliminate seven of the simulations from the grid. We allow each simulation to run for > 12 Gyr so that the behaviour is not sensitive to the precise details of the initial conditions, even in the cases with a long $t_{\rm cyc}$.

We made an initial visual inspection to classify the morphology of the outflow, finding that the duty cycle causes the adiabatic runs to fall into distinct regimes. Some example outputs are illustrated in Fig. 4.3. The top row shows the simulation with $f_{\rm cyc} = 0.033$, $t_{\rm cyc} = 0.5\,{\rm Gyr}$ whereas the lower row is generated from simulations with $f_{\rm cyc} = 0.75$, $t_{\rm cyc} = 0.5$ Gyr. The simulations are pictured at $t = 5.9$ Gyr, after a repeatable cycle has been established (see below).

In each row, the two left panels show the logarithm of gas density ρ over the range

$$10\,M_\odot\ {\rm kpc}^{-3} \leq \rho \leq 10^6\ M_\odot\,{\rm kpc}^{-3}$$

for the non-cooling and the cooling simulation. The final panel shows the temperature in the cooling case, scaled between $10^4\ {\rm K} \leq T \leq 10^7\ {\rm K}$. Arrows indicate the velocity vectors of gas cells in the halo.

At any given time the morphology of all our simulations roughly falls into one of three categories:

- *Shock-dominated*, where the morphology of the density and temperature maps is dominated by roughly spherical, discontinuous fluid flows (see e.g., top-left panel of Fig. 4.3). These predominantly occur when $t_{\rm cyc}$ is long and/or $f_{\rm cyc}$ is small; the halo is able to settle down between each "burst" of wind injection which therefore triggers a significant shock wave.

- *Chimney-dominated*, with a morphology which is more dominated by a classic chimney- or funnel-shaped, relatively smooth flow of gas (see e.g., bottom-left panel of Fig. 4.3). These can only be seen in our simulations with large $f_{\rm cyc}$ or $t_{\rm cyc}$, which allows the prolonged outflows to "punch through" the inflowing material. The halo material outside the main outflow often ends up being very turbulent in these cases.

- *Intermediate* outflows have morphologies that share characteristics of the two types.

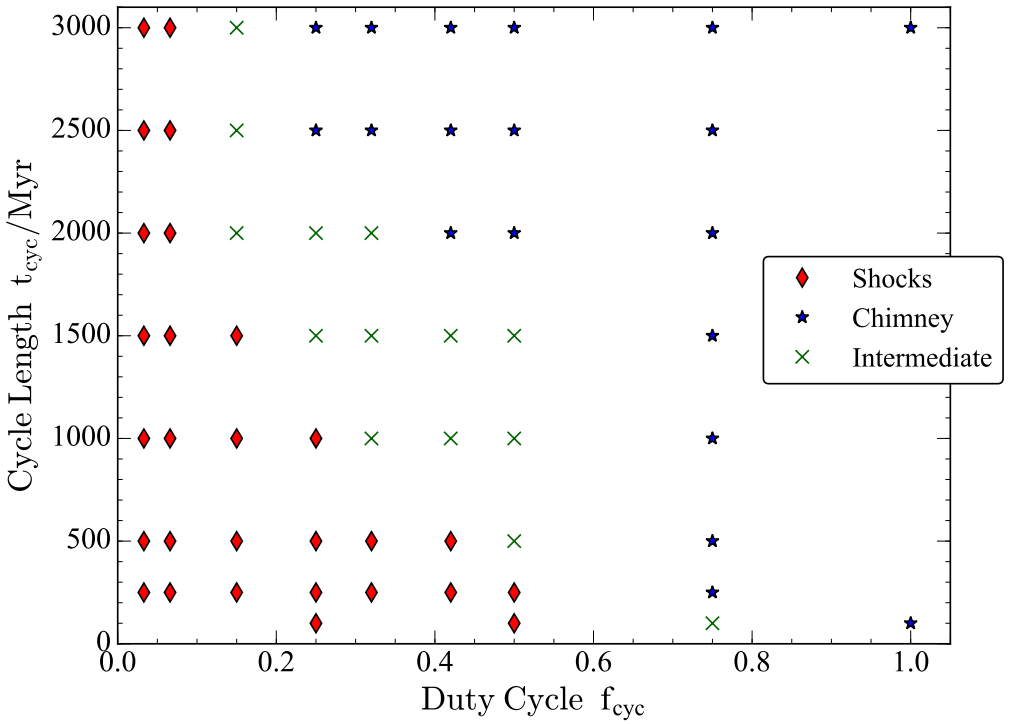

Figure 4.4: Distribution of shock-dominated and chimney-dominated outflow type with the variations of duty cycle and cycle length parameters. We make this classification by visual inspection of the outflows as described in the text. Red diamonds, blue stars and green crosses indicate the shock-dominated, chimney-dominated and intermediate cases. We have used the simulations with cooling enabled, but found that the differences in the case without cooling were minor. To maintain the average mass-loading, the density of the bubble scales in inverse proportion to the duty cycle, ranging from $1.7 \times 10^4\,\mathrm{M}_\odot\,\mathrm{kpc}^{-3}$ for $f_{\rm cyc} = 0.033$ to $6.1 \times 10^2\,\mathrm{M}_\odot\,\mathrm{kpc}^{-3}$ for $f_{\rm cyc} = 1.0$.

A single simulation can switch between the three phases above during its evolution. However typically shocks can only dominate for a limited time after the outflow switches on, after which it sweeps out of the halo into the IGM beyond our box. When $f_{\rm cyc}$ is small (such as in the top row of Fig. 4.3), the entire outflow consists of a series of outgoing shocks and a chimney never establishes itself. Conversely when $f_{\rm cyc}$ is large, the outflow normally looks like a classic chimney pattern. Cases with intermediate $f_{\rm cyc}$ values and large $t_{\rm cyc}$ can switch between the two morphologies depending on the time of observation.

As a rough illustration of this point, Fig. 4.4 shows our classification for the dominant morphology of each simulation. Shock-dominated outflows are represented with red diamonds and chimney-dominated cases with blue stars. Green crosses indicate the intermediate type where no clear classification can be decided on because it is strongly time-dependent.

Comparing the upper-left panel and upper-mid panels of Fig. 4.3, we can see that once cooling is enabled, the shocks have a different structure. The shell of dense material caused by the initial shock is able to cool efficiently and so the highest densities are formed behind the shock-front. In the illustrated snapshot, the shock from the most recent episode has reached around $70\ \mathrm{kpc}$ above the galaxy; above this are the remains of the previous shock sweeping through the halo. Behind the shock front, the dense gas reaches a regime where its radiative cooling time is short. The typical outflow speeds in the illustrated halo are $\sim 70\ \mathrm{km\,s^{-1}}$; because the bursts of high-velocity outflows are so short, the initial energy is rapidly spread across a greater mass of gas, making for high mass loadings but lower velocities in the halo.

Conversely high-velocity cold gas is typically not generated in large quantities in simulations with a large $f_{\rm cyc}$, where the chimney is the dominant morphology. The lower panels of Fig. 4.3 show how the gas establishes a direct route out of the halo and so maintains its high initial outflow speed once the initial resistance of the cooling inflow has been cleared away. This high speed, high temperature, relatively low-density flow rarely reaches a regime where it cools efficiently.

To make a more quantitative comparison between the cases and their ability to generate cool outflows, we quantified the fraction of the outflowing mass that is cool in each case. We defined outflowing gas as having an upwards vertical velocity $> 20\,\mathrm{km\,s^{-1}}$ and "cool" gas to be at temperatures $T < 5 \times 10^4\,\mathrm{K}$. For each snapshot we then measured the cool

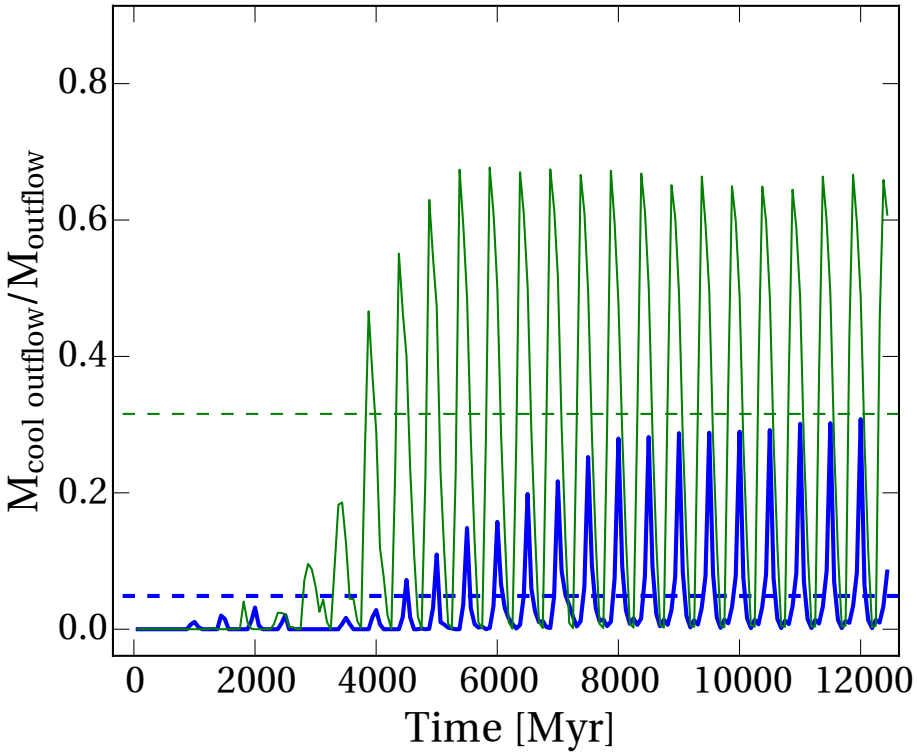

Figure 4.5: Cool gas fraction comparison between the galaxies illustrated in Fig. 4.3. For each timestep, the cool gas fraction is calculated as a mass fraction of outflowing gas ($v_y > 20\,\mathrm{km\,s^{-1}}$) that has temperatures satisfying $T < 5 \times 10^4\,\mathrm{K}$. The thinner, green line shows the case $f_{\mathrm{cyc}} = 0.033$ whereas the thicker blue line shows the case $f_{\mathrm{cyc}} = 0.75$. The time-averaged value for the two cases is shown by corresponding dashed horizontal lines and is 32 per cent and 5 per cent for the two respective cases.

outflow fraction by mass. The results for the two simulations that we have discussed so far are shown in Fig. 4.5; the thicker and thinner lines respectively are generated from the chimney-dominated $f_{\rm cyc} = 0.75$ and shock-dominated $f_{\rm cyc} = 0.033$ cases.

Over the first few cycles, the amount of cold gas forming in both cases grows. Eventually a repeating cycle is established. Each cycle starts when the galaxy (below the box) starts injecting gas; at this point the amount of cool gas becomes small as the injected material is hot and compresses any cold material. Once the outflow shuts off, the fraction of cool gas tends to grow as the shock expands outwards and radiative effects become significant behind the shock front. Short $f_{\rm cyc}$ values switch off the heating source earlier in the cycle and thus allow larger cool mass fractions to build up before the next cycle begins. This is reflected in the average, taken over the penultimate two cycles, of the cool mass fraction which is 32 per cent and 5 per cent in the $f_{\rm cyc} = 0.033$ and $f_{\rm cyc} = 0.75$ cases. These averages are shown by the horizontal dashed lines.

In Fig. 4.6 we show this average cool-mass-fraction of outflows calculated for each simulation. The position on the plot shows the duty cycle and cycle length, and the size of the plotted dot is in proportion to the cool-mass-fraction. The average is taken over gas outflowing at speeds greater than $50\ {\rm km\ s^{-2}}$ after $9\ {\rm Gyr}$, when the cycle has become stable. Our summary statistic of the total cool mass fraction gives a sense of how observable the cool phase is likely to be, but we emphasise that the cool gas often occupies a relatively small volume and is only present in large quantities during certain parts of the cycle.

Outflows with our smallest duty cycle (i.e., on the left edge of the figure) are able to generate cool mass almost irrespective of the cycle length, although for $t_{\rm cyc} \leq 100\ {\rm Myr}$ we find that the individual shocks occur so regularly that they prevent the gas from cooling. For long cycle lengths $t_{\rm cyc} \geq 2000\,{\rm Myr}$ we also find a slight decline in our cool mass fraction which is caused by the cool outflows being slower in this regime (so that a smaller proportion pass the velocity cut).

We can also generate large cool-gas fractions in a few cases that we classified as chimneys (middle-top part of Fig. 4.6) at $f_{\rm cyc} = 0.5$, with $t_{\rm cyc} = 3000$ or 2500. In these cases, galaxies spend half their time injecting hot gas into the halo. This means that the halo is left undisturbed for a period of time $> 1\ {\rm Gyr}$ which is long enough for even relatively diffuse gas at $\sim 10^4\,{\rm M_\odot\,kpc^{-3}}$ to cool. As seen in Fig. 4.3, there is gas at this density in the regions around our chimneys. However for the cases where the cycle fraction reaches $f_{\rm cyc} = 0.75$ (towards the top right of the figure), the period for which the halo is undis-

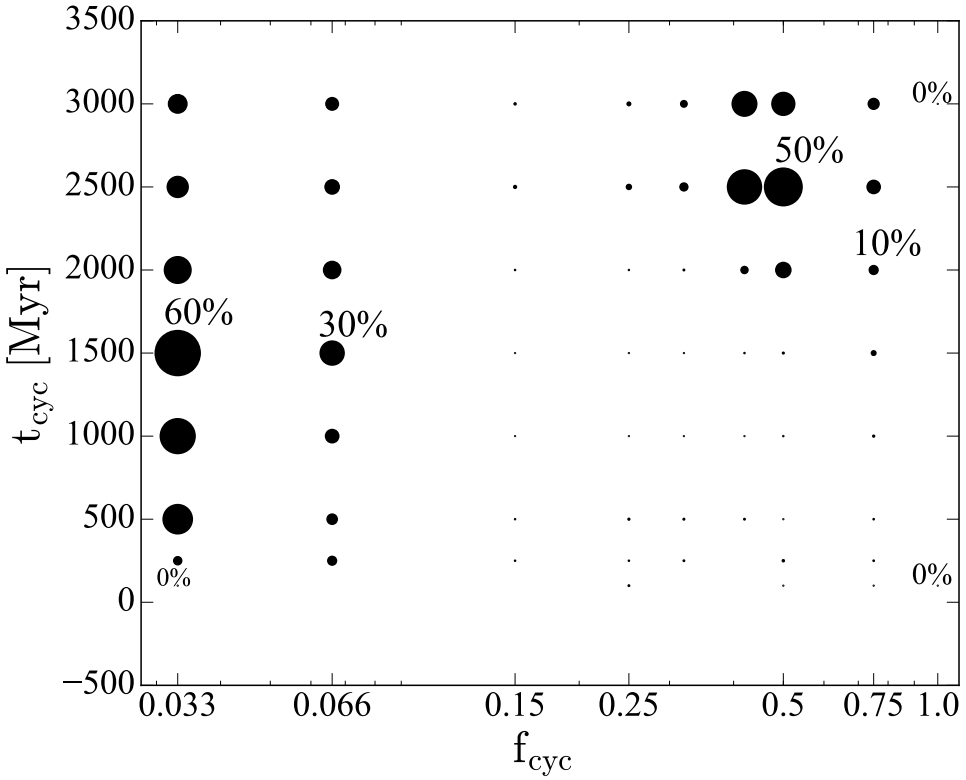

Figure 4.6: Duty cycle $f_{\rm cyc}$ distribution with the cycle length, $t_{\rm cyc}$ as shown in Fig. 4.4 , but now the size of the circles show the amount of cool gas in the outflow and the percentages show the numeric value for a selection of models. Our results highlight two regimes in which cool gas is easiest to form; either a small duty fraction is required, giving relatively high outflow densities and so allowing gas to cool in between bursts, or the total cycle time must be long, yielding long time periods during which denser regions of the turbulent halo can cool.

turbed by incoming material becomes less than the cooling time of approximately 1 Gyr, and the cool gas fraction declines.

By contrast in the low-$f_{\rm cyc}$ regime, the regular shock fronts between new gas and the existing halo always reach high densities ($\gg 10^4\ {\rm M}_\odot\,{\rm kpc}^{-3}$), bringing the cooling time down to a few hundred Myr (depending on the exact temperature and density) and so allowing efficient cold gas formation.

Figure 6 highlights the existence of a transition between $f_{\rm cyc} = 0.15$ and 0.25 which falls in between these cases and is unable to efficiently produce cool gas. In these cases, gas behind the shock is hotter and denser than its environment. In fact we find that, during the "off", relatively undisturbed phase, a portion of the halo does cool; however, it is slow-moving and starts to infall; it is therefore not counted since we made a cut to include only gas particles travelling faster than 50 km ${\rm s}^{-1}$. The gas that is outflowing in these cases remains hot (10^5 K) and with low density ($\sim 80\ {\rm M}_\odot\,{\rm kpc}^{-3}$).

4.4 Conclusions

We have discussed whether supernova-driven winds can account for cool gas in observed galactic outflows. Previous works have explored the scenario where feedback from supernovae drive outflows (Dekel & Silk, 1986). The general picture is that of SNe explosions combining into larger bubbles that sweep-up ISM gas that develops into an outflow (Veilleux et al., 2005), with wind speeds increasing with distance. This scenario has proved an effective feedback implementation for simulations to produce realistic disc galaxies (Scannapieco et al., 2012). Then, the energy released into the interstellar medium could potentially drive galactic winds. To understand in detail the galactic disc in a full cosmological scenario is currently not yet possible because the scales involved span several orders of magnitude in temperature, density and time-scales (see Chap. 2). This motivates the development of hydrodynamic numerical experiments to identify and understand the physics involved in outflows. These studies account for turbulence in the disk (e.g., Scannapieco & Brüggen, 2010) or model the ISM varying properties such as gas surface density, gas fraction and star-formation rate (Creasey et al., 2013), as inputs to drive a global outflow. While these studies focus on the hydrodynamics in the ISM, they do not follow this material as it interacts with the galactic halo.

In this paper we have considered the possibility that the cool gas material observed in

outflows in the circumgalactic medium is a consequence of in situ cooling (Thompson et al., 2016), using the RAMSES code. We do not simulate the disk in our galaxies; instead we manually inject gas moving into the base of a box representing the halo (see also Mac Low & Ferrara, 1999). We started by finding and testing equilibrium inflows to be sure that the effects we observe are a result of outflows rather than the choice of initial conditions; see Eqs. (4.7) – (4.9). We used a fixed potential corresponding to a $50\ \mathrm{km\,s^{-1}}$ virial velocity dwarf galaxy. The cooling function $\dot{Q}_{\mathrm{cool}}$ we adopt is suitable for primordial gas as implemented by RAMSES, which underestimates the true cooling rates and so leads us to conservative conclusions.

We modified RAMSES to inject a time-varying flow into the bottom of the computational domain, according to a set of parameters summarised in Table 4.1. Our particular focus was on the role that varying star formation rates in the galaxy could have on the evolution of outflows as they traverse the halo. From the complete set of parameters characterising outflows we therefore varied two: the overall star formation cycle length, t_{cyc}, and the fraction of that time spent pumping gas into the CGM, f_{cyc}. We varied these while keeping the total energy injection and mass loading constant. We found a close connection between the parameters and the overall nature of the outflows' traversal of the CGM (Fig. 4.4). This in turn has a strong effect on the multiphase nature of the outflows.

The amount of cooler $T < 5 \times 10^4\,\mathrm{K}$ gas present in the outflow varies strongly over the course of a cycle (Fig. 4.5). Cool material is typically able to form as a shock propagates outwards provided that no hot material is being injected behind the shock. This leads to the time-averaged cool mass fraction depending on both t_{cyc} and f_{cyc} (Fig. 4.6). There are two regimes in which we obtain large cool mass fractions: the first has a small f_{cyc}, corresponding to a rapidly fluctuating star formation rate. Provided t_{cyc} is greater than a few hundred Myr, the successive shocks do not join up into a coherent flow and the strong time variability triggers waves of effective cooling that travel through the CGM. The second approach is to leave a long period $\gtrsim 1\ \mathrm{Gyr}$ between successive star formation epochs; in this case cool gas is able to form in the turbulent halo left behind when ejection from the disk shuts off. Our results suggest that steady flow or single-burst solutions with cooling (Thompson et al., 2016) form a lower bound on the amount of in situ cooling to be expected in realistic galaxies with time-varying feedback.

Our interest in cool gas is motivated by observational results that show the presence of a cool phase even at large distances from galactic centres (e.g., Nielsen et al., 2013),

which is hard to explain in entrainment scenarios (Zhang et al., 2017). However it would be premature to compare our highly idealised study directly to observations. To enable our large parameter study, we had to restrict ourselves to two-dimensional solutions; the detailed behaviour in three dimensions could differ significantly. Other neglected aspects of the problem include the enhanced cooling rates from metal enrichment and the effects of thermal conduction and magnetic fields. Furthermore a realistic cosmological environment is far more complex than the uniform inflow solution that forms our initial conditions. In terms of the cooling rates, neglecting metals leads to a conservative bound; i.e., more realistic simulations may be able to form cold clouds more easily than our work suggests.

We hope to use our results to interpret the CGM around ab initio cosmological galaxy formation simulations. Some feedback algorithms enforce relatively steady-state star formation (e.g., Dalla Vecchia & Schaye, 2008; Oppenheimer & Davé, 2008; Vogelsberger et al., 2014; Schaye et al., 2015) whereas others lead to strong bursts (e.g., Hopkins et al., 2014; Keller et al., 2015) and the importance of this distinction for galactic dynamics has already been established (Pontzen & Governato, 2014). In future work we will study what role in situ cooling plays in these different scenarios, and make the link to observational constraints on the rich phenomenology of the CGM.

Chapter 5

Gaussian fields, power spectrum and correlation function of the Lyman α forest

"Nothing takes place in the world whose meaning is not that of some maximum or minimum. "

- Leonhard Euler

In this chapter I provide an overview of the statistical tools required to study large scale structure and the distribution of matter using the Lyman-α forest.

5.1 Gaussian Random Fields

The distribution of galaxies is clearly not random (see Fig. 5.1). As mentioned in the Introduction, the large scale structure forms a cosmic web where galaxies gather into sheets and filaments. The smoothed picture on large scales ($\sim$ 100 Mpc) starts to look more homogeneous, and this is why in cosmology the Universe on the largest scales is considered to be homogeneous and isotropic. Further evidence for large-scale homogeneity and isotropy is provided by the uniformity of the cosmic microwave background (CMB).

Gaussian random fields are important in cosmology to be able to describe analytically the statistical properties of inhomogeneities in the universe. I start by providing with some useful definitions.

Consider a random field $f(\boldsymbol{x})$ with zero mean, $\langle f(\boldsymbol{x})\rangle = 0$. The probability of realising some field configuration i.e., the probability distribution for a Gaussian random field, is the functional Pr[$f(\boldsymbol{x})$],

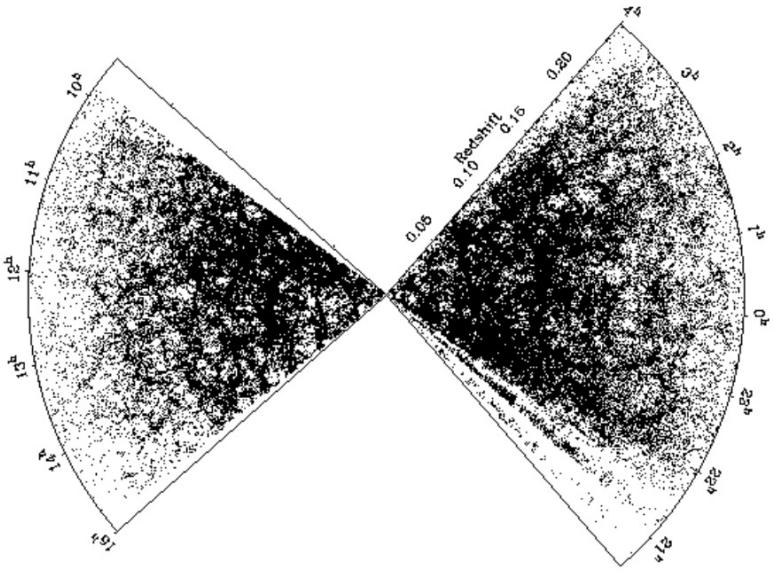

Figure 5.1: 2dF Galaxy Redshift Survey (Colless et al., 2001). The projected distribution of galaxies as a function of redshift. The slice highlights the large-scale structure of the Universe that can be probed with galaxy redshift surveys.

$$\Pr(f_1, \cdots, f_n) = \frac{\sqrt{\mathrm{Det} C_{ij}^{-1}}}{(2\pi)^{n/2}} \exp\left[-\frac{1}{2}\sum_{ij} f_i C_{ij}^{-1} f_j\right] \tag{5.1}$$

where $f_i \equiv f(\mathbf{x}_i)$ with $i = 1, ..., N$ and $N \to \infty$, and the correlation matrix $C_{ij}^{-1} = \langle f_i f_j \rangle$. The permitted forms for C_{ij} are strongly constrained by the requirement for statistical isotropy and homogeneity [1]. A density fluctuation (also known as the overdensity) can be defined in general as

$$\delta(\boldsymbol{x}) \equiv \frac{\rho(\mathbf{x})}{\langle \rho(\mathbf{x}) \rangle} - 1 \tag{5.2}$$

where $\langle \rho(\mathbf{x}) \rangle$ is the average of the matter density across the entire Universe. In the limit of small amplitude fluctuations, the distribution of density fluctuations δ becomes approximately Gaussian reflecting its likely quantum mechanical origin.

It is often helpful to consider the properties of δ in Fourier space rather than real space.Therefore, the Fourier transform of the overdensity field δ is defined as,

$$\tilde{\delta}(\mathbf{k}) = A \int d^3x \exp[-i\boldsymbol{k} \cdot \boldsymbol{x}] \delta(\boldsymbol{x}), \tag{5.3}$$

[1] note that not all random fields have these properties

with an inverse

$$\delta(\boldsymbol{x}) = B \int d^3k \tilde{\delta}(\boldsymbol{k}) \exp[i\boldsymbol{k} \cdot \boldsymbol{x}], \tag{5.4}$$

where A and B are the adopted constant $(2\pi)^{-3/2}$.

The Fourier transform of a Gaussian field is still Gaussian. This is an important property because when the overdensity field is written as a spatial Fourier decomposition its Fourier coefficients F_k are statistically independent and have the same Gaussian distribution (Bardeen et al., 1986a). I review the Fourier series formalism in the next section.

Additionally, when the density field has large scale variations but is also composed of individual, countable small objects such as galaxies or quasars, it can be approximated as the smooth field (on large scales) plus a *shot noise* term that accounts for the small scale Poisson statistics. In the limit of large numbers of objects, the Poisson statistics limit to Gaussian so the overall field can still be approximated as Gaussian, with a power spectrum composed of a cosmological and shot-noise term (see below).

5.2 Power Spectrum

The amplitude of fluctuations on the different length scales are described by the power spectrum. The power spectrum is a statistical description of a signal, giving the amplitude of fluctuations as a function of frequency.

Temporarily considering the 1D case, for any integrable function $f(t)$, its Fourier transform, FT (denoted by the circumflex $\tilde{f}(k)$), is defined by

$$\tilde{f}(k) = \lim_{T\to\infty} \frac{1}{\sqrt{2\pi}} \int_{-\frac{T}{2}}^{\frac{T}{2}} f(t) \exp[-ikt] dt. \tag{5.5}$$

Formal results are normally obtained for the limit that the interval is actually infinite, but for practical calculations (including simulations) it is often necessary to have a finite window where, for example, t runs from $-T/2$ to $T/2$. Using a finite window in this way leads to a "smearing" of the signal in Fourier space, or more technically, a convolution with the window function. Nonetheless the basic properties of the Fourier transform and the power spectrum remain unchanged.

The power spectrum is, up to a convention-dependent normalisation, given by the absolute value of the squared Fourier amplitudes in equation (5.5): $P(k) \propto |\tilde{f}|^2$.

Consider the following example, a periodic function $f(t)$,

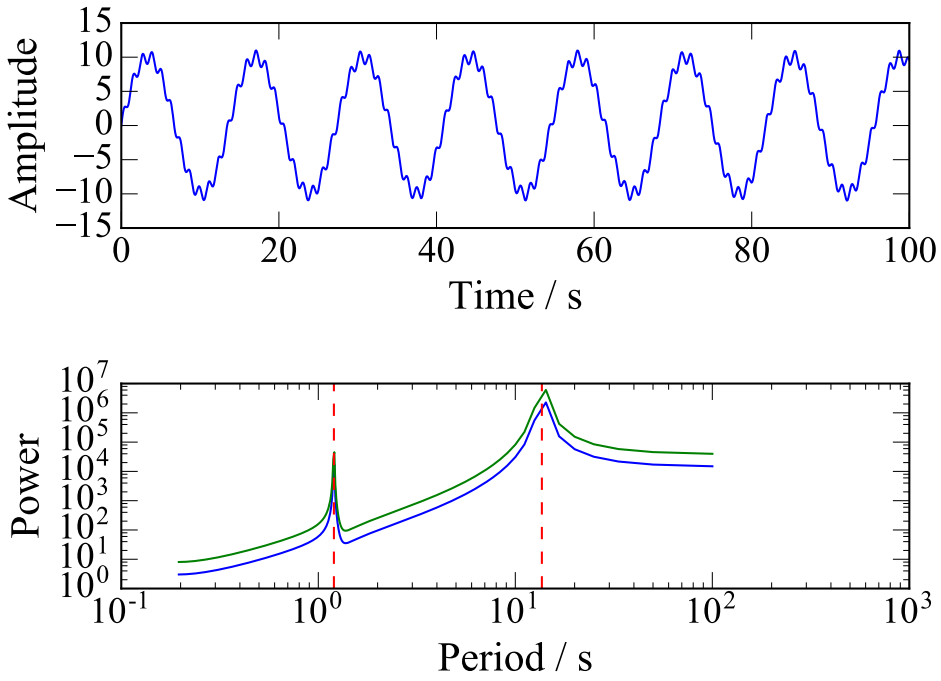

Figure 5.2: Upper panel: Mathematical function $f(t)$ from Eq. (5.6) in time. Bottom panel: Power spectrum: the square of the Fourier coefficients ($|\tilde{f}|^2$) from the Fourier transform of $f(t)$.

$$f(t) = \sin(2\pi t/T_1) + 10\sin(2\pi t/T_2), \tag{5.6}$$

where T is the period and is related to the frequency as $f_{\rm rec} = 1/T$. The form of the function $f(t)$ is plotted in Fig. (5.2). For this particular example I chose the following values for the two periods $T_1 = 1.2$ and $T_2 = 13.64$. When plugging Eq. (5.6) into the Fourier transform definition we end up with a long combination of exponential functions in terms of t and x, but these can be evaluated numerically and then we are more interested in the form that $|\tilde{f}|^2$ takes.

In my example, this specific power spectrum is shown in the bottom panel of Fig. 5.2. The power spectrum plot shows that the two characteristic frequencies of the input function are recovered in the power spectrum, despite this spectrum being calculated from a finite window. The highest peak in the power spectrum refers to the dominant frequency, $f_{\rm rec} = 1/T_2 = 1/13.64$. The peak is at the frequency which contributes the most to the signal. We can see from the power spectrum that there is another frequency embedded in the signal: small wiggles with high frequency, or, as we see from the power

spectrum, smaller period T_1.

Thus, in general, the power spectrum describes the contribution of different frequencies to a signal and can be estimated from a finite window. This is especially important in cosmology where we only ever measure a portion of the Universe.

In **cosmology**, these concepts also apply for the characteristic fluctuations in the density field. A lot of the information in the density fluctuations is captured in their power spectrum. To remind the reader, the density at any point $\mathbf{x}$ is denoted by $\rho(\mathbf{x})$ and the mean density as $\langle\rho\rangle$ in a given volume V. The overdensity $\delta(\mathbf{x})$ is then defined by Eq. (5.2).

The power spectrum is therefore expressed by,

$$\langle\delta(\boldsymbol{k})\hat{\delta}(\boldsymbol{k}')\rangle = (2\pi)^3\delta(\boldsymbol{k}-\boldsymbol{k}')P(k), \tag{5.7}$$

where $\delta_{\rm D}(\boldsymbol{k}-\boldsymbol{k}')$ is Dirac delta given by,

$$\delta_{\rm D}(\boldsymbol{k}-\boldsymbol{k}') = \int d^3x \exp[\pm i(\boldsymbol{k}-\boldsymbol{k}')\cdot\boldsymbol{x}]. \tag{5.8}$$

Because $\delta(\mathbf{x})$ is a random field with zero mean $\langle\delta(\mathbf{x})\rangle = 0$, the power spectrum $P(k)$ in Eq.(5.7) is the only quantity required to define a homogeneous, isotropic, Gaussian random field. This is important because both (statistical) homogeneity and isotropy mean that the statistical properties are the same as the original field under translation and rotation.

In summary, the power spectrum yields a complete statistical description of the fluctuations from a Gaussian distribution. In particular it describes the amplitude of the fluctuations as a function of scale.

The power spectrum has been predicted directly from inflation combined with the "transfer function" which describes the impact of early-universe physics (including baryon acoustic oscillations, see Chapter 1). It has been compared to a variety of observations; for instance, measurements of the fluctuations in the temperature of the CMB; the clustering of galaxies and the distribution of these clusters; gravitational lensing, the Lyman-α forest, etc. Each of these measurements carries a different bias that must be understood in order to study the implications for the underlying power spectrum.

In the next section I give a brief explanation of the bias in general, as well as, the type of bias that is relevant for this thesis.

5.3 Bias

The notion of bias describes the relation between tracers such as galaxies and the underlying dark matter. It is the statistical connection (on large scales) between tracers and the dark matter field.

The case of galaxies as tracers is worth mentioning since they represent the first example of probing the underlying matter power spectrum with a biased tracer, observed in sky surveys e.g. SDSS (Stoughton et al., 2002), 2dF Galaxy Redshift Survey (Colless et al., 2003). The relation between the density of galaxies (or clusters of galaxies), n_g, and the density matter, ρ_m, at a fixed time follows (Desjacques et al., 2016; McDonald, 2006; Fry & Gaztanaga, 1993),

$$\begin{aligned}\delta_g(\mathbf{x}) \equiv & \frac{n_g(\mathbf{x})}{\bar{n}_g} - 1 \\ = & b_1 \delta(\mathbf{x}) \\ = & b_1 \Big[\frac{\rho_m(\mathbf{x})}{\bar{\rho}_m} - 1 \Big],\end{aligned} \tag{5.9}$$

in which b_1 is the bias, $\bar{n}_g$ is the mean comoving number density of galaxies and ρ_m is the comoving background matter density.

Equation (5.9) represents an ansatz that the physics of the galaxy formation process results in a population of galaxies whose number density field traces the mass density field in an imperfect way which can nonetheless be represented by a single parameter. This is motivated by studies of the clustering of peaks in a Gaussian random field (Bardeen et al., 1986a; Lumsden et al., 1989).

In practice, large-scale hydrodynamical simulations find that the relation of density fields between galaxies and mass, as well as gas temperature, is not only biased but can also be scale-dependent and non-linear (Blanton et al., 1999; Iliev et al., 2003; Gao et al., 2005; Jose et al., 2016). Only on the largest scales do biases typically become independent of scale, and can therefore be described by a single number (as in Eq. 5.9).

Scale dependent bias

At the beginning of Sec. 5.1, I showed how the overdensity $\delta(\boldsymbol{x})$ is periodic and it can be expanded as a Fourier of series providing us with the transformed $\tilde{\delta}(\boldsymbol{k})$, where $\boldsymbol{k}$ is the Fourier wavevector. Equations (5.4) and (5.3) tell us that if we have a density as a function

of position this corresponds to a density as a function of wavelength (or the equivalent wavevector), which in turn is related to the bias and the galaxy density variations because the transform is linear

$$\tilde{\delta}_g(k) = b_1 \tilde{\delta}(k). \tag{5.10}$$

Because the power spectrum of galaxies $P_g(k)$ is proportional to $|\tilde{\delta_g}(k)|^2$, in the case of constant bias the measured power spectrum relates to the underlying matter power spectrum via $P_g(k) = b_1^2 P(k)$. But if we find a tracer where the final power spectrum is not directly proportional to the underlying $P(k)$, we can think of the bias as being scale-dependent, i.e. $P_g(k) = b_1(k)^2 P(k)$.

In the case of radiation the physics implies that such scale-dependent bias is inevitable. Photons spread out from their origin, and, if we want to know where are the photons we also need to consider how photons spread. So, their final distribution must reflect this.

For example, Pontzen (2014) considers the photoionisation rate fluctuations $\delta_\Gamma(x)$. These are effectively composed of the convolution of sources with a function which describes how photons spread from their origins until they are absorbed. Consequently in Fourier space the convolution theorem implies that $\delta_\Gamma(k)$ is equal to the product of $\delta_{\rm sources}(k)$ with the Fourier transform of the photon spreading function. In turn, that means the final power spectrum P_Γ is also a scale-dependent function times the underlying source power spectrum. This can be interpreted as a scale-dependent bias. While P_Γ cannot be measured directly, it can have an effect on other measured quantities as we shall see.

5.4 Lyman-alpha power spectrum

For the purpose of this thesis, I will now focus on the power spectrum of the Lyman-α forest transmitted flux. From observational studies and the comparison of these with simulations (e.g. Vogt et al., 1994; Cen et al., 1994), there is substantial evidence that tell us that the neutral gas in the filaments connects strongly with the underlying dark matter.

On large scales, the gas density is strongly connected to the dark matter density and is one of the prime tracers of the large-scale structure in the Universe [2] (Bautista et al., 2017; White et al., 2010; Slosar et al., 2009; Zaldarriaga et al., 2001). But the small-scale giving

[2] On small scales other effects have to be taken into account. For example Jeans smoothing: on smaller scales $\lesssim$ 100 kpc gas pressure counteracts gravitational collapse. This relation is dependent on the finite temperature of the gas. Baryonic fluctuations are suppressed relative to the pressureless dark matter, yielding to a filtered power spectrum on small scales. See more details in Rorai et al. (2013).

rise to this connection is complex (Arinyo-i-Prats et al., 2015; Doux et al., 2016). Absorption in neutral gas is highly dependent on the gas density (Machacek et al., 2000); and, neutral hydrogen in the intervening medium responsible for the Lyman-α absorption has low density (Hu et al., 1995).

The gas temperature and density are tightly correlated by two processes: cooling due to expansion and recombination, and heating from photoionisation (e.g., Theuns et al., 1998). There are two processes playing an important role in the physics of the neutral fraction gas: the temperature of the gas producing a recombination rate and the ionisation caused by photons coming from an ultraviolet background (Madau et al., 1999).

The absorption of redshifted Lyman-α photons is measured by the observed transmission spectra in the continuum of quasars, which provides a map along the line-of-sight of the absorbing material between us and the quasar. This observable transmitted flux fraction F is defined by the ratio between the photon number observed and the source of emitted photons (e.g., Machacek et al., 2000; Hui et al., 1997),

$$F = f/f_c = e^{-\tau}, \tag{5.11}$$

where τ is the optical depth to the Lyman α absorption, f is the observed flux and f_c is the continuum flux where there is no intervening absorption. In terms of any observed angle $\mathbf{n}$ and redshift z, the fluctuation in the transmission is defined as

$$\delta_F(\mathbf{n}, z) = \frac{F(\mathbf{n}, z)}{\langle F(\mathbf{n}, z)\rangle} - 1, \tag{5.12}$$

where $\langle F(\mathbf{n}, z)\rangle$ is the mean value of the transmission.

More explicitly, in terms of the spectral wavelength λ the fluctuations in the Lyman α forest flux are given by

$$\delta_F(\lambda) = \exp[-\tau(\lambda)]/\langle\exp[-\tau]\rangle - 1, \tag{5.13}$$

where $\tau = \tau(\lambda)$ is the optical depth to the Lyman-α absorption (McDonald et al., 2006). The wavelength observed from the absorption spectrum allows the determination of the redshift of the intervening gas, responsible for scattering.

In ionising equilibrium, the optical depth τ can be approximately related to the gas density as $\tau \propto (1+\delta)^{\alpha}$ (e.g. Seljak, 2012), where δ is the gas overdensity from Eqs. (5.4) and (5.3), and the value of α can be estimated from simulations. It is also possible to estimate the value of α analytically using the Fluctuating Gunn-Peterson Approximation (FGPA) as shown in Becker et al. (2015).

The transmission fraction F is a function of redshift as in Eq. (5.12). As a consequence, the power spectrum $P_F(\mathbf{k})$ depends on the angle between $\mathbf{k}$ and the direction of observation in redshift space [3]. The relation in Eq. (5.13) is a non-linear transformation of the density, making the relation between the Lyman-α power spectrum and the density power spectrum non-trivial. On small scales, the relation of the physical properties of the gas (such as temperature, velocity gradient and the underlying density field with the flux transmission fraction) is non-linear and the values of δ_F follow the non-linear evolution of the gas density in the IGM. On large enough distances, the average of δ_F relates to the mass density (Arinyo-i-Prats et al., 2015) according to a linear expression written as some constant (the bias) times the density plus the velocity gradients,

$$\delta_F = b_{F_\delta}\delta + b_{F_\eta}\eta, \tag{5.14}$$

where δ is the mass density fluctuation, b_{F_δ} and b_{F_η} are bias factors which I define below. The factor η is the dimensionless gradient of the peculiar velocity v_p with the coming coordinate x_p, both along the line-of-sight, defined as

$$\eta = -\frac{1}{aH}\frac{\partial v_p}{\partial x_p}, \tag{5.15}$$

where a the scale factor and H is the Hubble constant. In summary, on the large scale regime the transmission power spectrum is proportional to the power spectrum of the mass fluctuations as established by Eq. (5.14). However, because of the dependence on η as well as δ, the observed power spectrum of Lyman-α is actually anisotropic (different along the redshift direction), even when the underlying density field δ is statistically isotropic. These so-called "redshift space distortions" are discussed further in Sec. 5.6.

5.5 Correlation function

Another important measurement for the description of statistical fields is the correlation function. If the density field is continuous, the values that the overdensity δ continuous function take at two nearby points $\mathbf{x'}$ and $\mathbf{x'+x}$ must be correlated. The value of $\delta(\mathbf{x'})$ is known, and the uncertainty in $\delta(\mathbf{x'+x})$ decreases as $\mathbf{x}$ approaches to 0. The functions

[3] Note, that Arinyo-i-Prats et al. (2015) defines the power spectrum as P_F where μ is the cosine of the angle between k (the Fourier wave vector from the line-of-sight) and the observed source.

δ(**x′+x**) and δ(**x′**) are mutually dependent, and the degree of this dependency is quantified by the correlation function.

The definition of the two point *correlation function* is

$$\xi(x) = \langle \delta(\mathbf{x'})\delta(\mathbf{x'+x}) \rangle = \int \langle \delta_{\mathbf{k}} \delta_{\mathbf{k'}} \rangle e^{i\mathbf{k}\cdot\mathbf{x'}} e^{i\mathbf{k'}\cdot(\mathbf{x'+x})} \, d^3k d^3k', \tag{5.16}$$

where **k** and **k′** are in Fourier space.

The probability density function for a N-dimensional vector f_j is a multi-variate Gaussian fully specified by the correlation function

$$\langle f_i f_j \rangle = \xi(|\mathbf{x}_i - \mathbf{x}_j|) \equiv \xi_{ij}, \tag{5.17}$$

where $f_i \equiv f(\mathbf{x}_i)$, and the indices i and j range from 1,...,N and they refer to sample values of the field at different locations.

Because of isotropy, $\xi(x)$ depends only on the distance between the two points x_1 and x_2, but not on orientation. If statistical isotropy is broken, one may want to keep the orientation information e.g. redshift distortions (explained below in Sec. 5.6), which affect clustering only along the line-of sight.

By substituting the Fourier expansion of the field into Eq. 5.16, the power spectrum can also be expressed in terms of $\xi(x)$ as

$$\xi(x) = \langle \delta(x_1)\delta(x_2) \rangle = \int \frac{d^3k}{(2\pi)^3} e^{ik\cdot x} P(k). \tag{5.18}$$

and, therefore carry the same amount of information because they are Fourier transform pairs,

$$P(k) = \int \xi(x) e^{-ikx} d^3x. \tag{5.19}$$

In this thesis I work exclusively with the power spectrum, but the results could be re-expressed in terms of a correlation function using this result. To do so and compare to observations would, however, also require taking into account the redshift space distortions as described below.

5.6 Redshift space distortions (RSD)

The redshift space distortion, RSD (Peebles, 1980; Cole et al., 1994; Scoccimarro, 2004), is an observational effect in cosmology in which the distribution of galaxies seem to be distorted e.g. normally an elongated distribution along the redshift dimension (Hamilton,

1998; Ballinger et al., 1996; Kaiser, 1987) or flattening (Hamilton, 1998). The distortion effect is caused by the peculiar velocities of the galaxies, when positions of galaxies are plotted as a function of their redshift rather than as a function of their actual distance. In redshift space, the observed position is a sum of the radial distance in velocity units; and, the radial velocity, and the velocity gradients are the perturbations better known as RSD.

RSD are important to predict (Percival et al., 2004; Hamilton, 1998). If we consider that on large scales the velocity of any tracer follows the dark matter it would mean that it is not necessary to have a velocity bias. But, if the field is transformed by a mapping of the RSD, then the transformed field acquires a velocity bias (Seljak, 2012).

An example of this is the Lyman-α forest (Zaldarriaga et al., 2003). The observable transmission flux F of the Ly-α is dependent on the optical depth because the observable of the transmitted flux F is dependent on τ, and the RSD act on it. Therefore, a derivation of both the density bias b_{F_δ} and the velocity bias b_{F_η} are necessary, although sometimes this is quoted as a single bias b with the parameter β (the RSD parameter), which is the ratio between the two biases.

The power spectrum then follows the linear theory model of RSD (Cole et al., 1994; Slosar et al., 2011)

$$P_F(k,\mu) = b^2 P_L(k)(1+\beta\mu^2)^2 \tag{5.20}$$

where b is the bias factor of the forest, $P_L(k)$ is the real-space linear power spectrum, μ is the cosine of the angle between k and the line-of-sight and β is the RSD parameter.

In the work developed and presented in this thesis I do not consider the RSD explicitly, because it only goes as far as calculating HI. But, it would ultimately have to be included in any observational study. The results of this thesis could be straightforwardly treated with the formalism of Pontzen et al. (2014) to generate power spectra or correlation functions with redshift-space distortions following Eq. 5.20.

Chapter 6

Large-scale fluctuations in the cosmic ionising background: the impact of beamed source emission

"Nothing is more practical than a good theory. "

- Ludwig Boltzmann

The content in this chapter have been published in Monthly Notices of the Royal Astronomical Society (MNRAS) as Suarez & Pontzen (2017).

6.1 Introduction

Intergalactic neutral hydrogen can be detected in the spectra of background quasars; absorption at the rest-frame Lyman-α transition gives rise to a "forest" with hundreds of distinct absorption lines corresponding to neutral hydrogen at different redshifts (Weymann et al., 1981). On small scales, between 1 and $40\ h^{-1}$ Mpc comoving, the forest can be used as a statistical tracer of the distribution of matter (Viel et al., 2005).

In fact hydrogen in the intergalactic medium (IGM) at $z < 5$ is highly ionised by ultraviolet (UV) background radiation produced by stars and quasars (Croft, 2004; Viel et al., 2005), leaving only a trace of HI. This UV background is therefore an essential element in simulations of the forest (Cen et al., 1994). When modelling Lyman-α absorption, the neutral hydrogen density is assumed to be in ionisation equilibrium with a uniform ionising

background (e.g. Katz et al., 1996; McDonald, 2003; Haehnelt et al., 2001; Croft, 2004). Theoretical and observational arguments both show that this assumption can fail in various limits and a fluctuating UV background ought at least in principle to be included in analyses of the forest (Maselli & Ferrara, 2005).

Recently some attention has been devoted to understanding HI fluctuations on scales approaching the mean-free-path of an ionising photon (Pontzen, 2014; Gontcho A Gontcho et al., 2014; Pontzen et al., 2014; Bautista et al., 2017). In this large-scale limit, the correlation of HI with cosmological density progressively weakens and eventually reverses sign because the clustering of the radiation field becomes stronger than the clustering of intergalactic hydrogen. Additionally, if quasars contribute significantly to the photon production budget, an uncorrelated shot-noise component is added to the power due to their intrinsic rarity.

A number of factors have been neglected from radiative transfer calculations to date, however. These include beaming of sources, variable heating from high-frequency photons, and time dependence. In this paper we tackle the first of these simplifications and explore the effect of quasar beaming on the shot-noise contribution to the large-scale diffuse HI power spectrum. We estimate the correction to the radiation fluctuations when emission is not isotropic but beamed for a random distribution of quasars.

The plan for the remainder of this paper is as follows. In Sec. 2 we derive the emissivity power spectrum accounting for a population of sources with fixed beam widths but random orientations. In Sec. 3 we discuss the radiation transfer equation appropriate for this distribution (with further detail in Appendix A). We present the resulting power spectrum of the radiation and HI fluctuations in Sec. 4 and summarise in Sec. 5.

6.2 Fluctuations in the emissivity

6.2.1 Correcting the number density of sources $\bar{n}$

The simplest effect of source beaming is that the underlying number density $\bar{n}$ is no longer directly measured by observations. The observed number density $\bar{n}_{\rm obs}$ must be corrected for the probability of being detected. This probability is given by the area of the emission (the beam) divided by the total area of a sphere, assuming a random orientation. We assume a hard-edged beam with opening angle $2\theta_1$; see Fig. 6.1. The chance of

any given quasar to be seen is then

$$p(\text{seen}) = \frac{(A_1 + A_2)}{4\pi r^2} = 1 - \cos\theta_1. \tag{6.1}$$

in which A_1 and A_2 are the areas of two axisymmetric beams. The isotropic case is recovered when the angle θ_1 is equal to $\pi/2$. In the limit that θ_1 approaches zero, the emission becomes a pencil-beam and the likelihood of observation becomes extremely small.

The number of density sources we detect, $\bar{n}_{\rm obs}$, is the true mean density $\bar{n}$ times the probability for observing each one:

$$\bar{n}_{\rm obs} = \bar{n}(1 - \cos\theta_1). \tag{6.2}$$

In Pontzen (2014; henceforth P14), it was assumed these two densities are equal; for the results in this work, we fix $\bar{n}_{\rm obs}$ at the value estimated by P14, meaning that the underlying density $\bar{n}$ varies. We emphasise that $\bar{n}_{\rm obs}$ is itself highly uncertain, but that for the purposes of understanding the effects of beaming it is simplest to keep it fixed.

6.2.2 Definitions required for the emissivity derivation

In the remainder of Section 2 we will calculate the effects of beaming on the emissivity power spectrum from discrete sources. A fraction of photons comes from recombination of the IGM, but following the approach of P14 we account for those through an appropriate additional term in the radiative transfer equation (see Section 6.3). Here, we can therefore focus on the discrete sources alone.

We start from a rate of emission of photons in a narrow band at frequency ν, in a small volume around comoving position $\boldsymbol{x}$ and in an interval around the direction vector $\boldsymbol{n}$; this is denoted $j_\nu(\vec{x}, \vec{n})$. As in P14, we simplify to a frequency-averaged quantity $j(\vec{x}, \vec{n})$ where

$$j(\vec{x}, \vec{n}) = \int j_\nu(\vec{x}, \vec{n}) \sigma_{\rm HI}(\nu) {\rm d}\nu\,, \tag{6.3}$$

and where $\sigma_{\rm HI}$ is the photo-ionisation cross section. The goal is to model fractional variations of j around its mean value $\langle j \rangle$, motivating the definition

$$\delta_j(\vec{x}, \vec{n}) = \frac{j(\vec{x}, \vec{n})}{\langle j \rangle} - 1. \tag{6.4}$$

We assume that variations on sufficiently large scales can be related to the cosmological matter overdensity δ_ρ multiplied by a constant bias b_j, plus a Gaussian white-noise

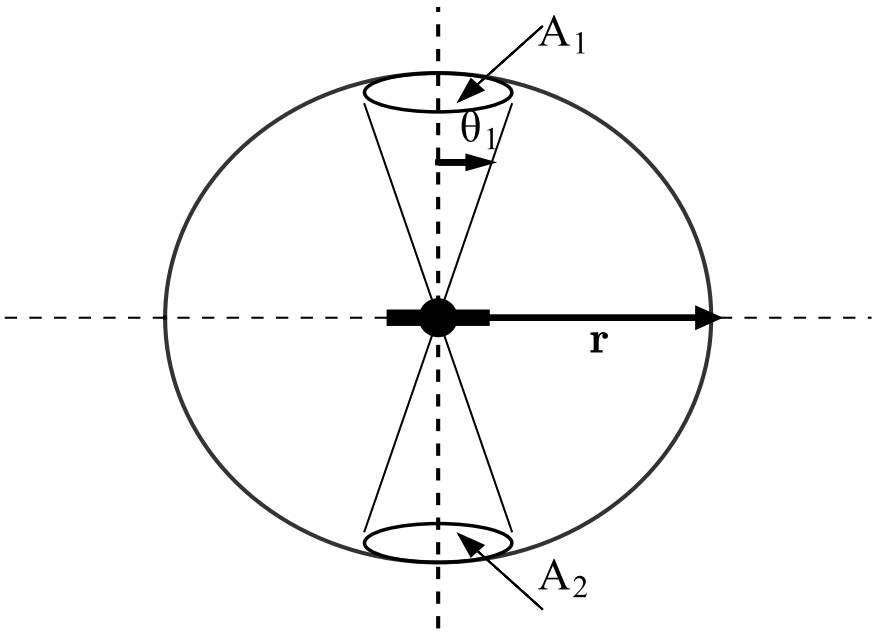

Figure 6.1: Geometry of our source model, which represents a quasar with variable beam width. The probability of detecting a quasar is proportional to the beam area A_1 and A_2. These in turn are determined by the opening angle, here parameterised by θ_1 with $0 < \theta_1 \leq \pi/2$. The isotropic case is recovered when $\theta_1 = \pi/2$.

field to represent shot-noise from the the rarity of sources. The validity of the assumption has not been tested in our work. It is a standard assumption strongly motivated by computing the clustering of the peaks where galaxies are expected to form (e.g., Bardeen et al., 1986b). While it is beyond the scope of our work to test its validity other authors have verified that it works well on large scales (Coles, 1993; Suginohara & Suto, 1991). Note that the shot-noise arises from the Gaussian limit of the Poisson statistics for a finite number of sources whereas the bias term comes from the underlying clustering.

The variations of the emissivity, δ_j, on large-scales is therefore written:

$$\delta_j(\vec{x}, \vec{n}) = b_j \delta_\rho(\vec{x}) + \delta_{j,\mathrm{SN}}(\vec{x}, \vec{n}), \tag{6.5}$$

where δ_ρ is the fractional matter overdensity at position $\boldsymbol{x}$. According to Eq. (6.5), we need only consider the component $\delta_{j,\mathrm{SN}}$ in the present work; by construction all angle-dependence arises in the shot-noise term and the radiation fluctuations that correlate with the cosmological density field will not be altered by beaming. As a final simplifica-

tion, P14 section II.C argues that the shot-noise contribution from galaxies is negligible (owing to their very high number density) and we can assume all contributions to $\delta_{j,\mathrm{SN}}$ arise from quasars.

In the remainder of this paper we will often need to work with Fourier-transformed and spherical harmonic representations of functions. For any function $F(\vec{x},\vec{n})$, these are defined respectively as

$$\tilde{F}(\vec{k},\vec{n}) \equiv \frac{1}{(2\pi)^{3/2}} \int \mathrm{d}^3\vec{x}\, e^{-i\vec{k}\cdot\vec{x}}\, F(\vec{x},\vec{n}) \text{ and} \tag{6.6}$$

$$F^{\ell m}(\vec{x}) \equiv \int \mathrm{d}^2\vec{n}\, Y^*_{\ell m}(\vec{n}) F(\vec{x},\vec{n})\,, \tag{6.7}$$

where $Y^*_{\ell m}(\vec{n})$ is the complex conjugate spherical harmonic basis function as defined in Varshalovich et al. (1988). The spherical harmonic Fourier modes $\tilde{F}^{\ell m}(\vec{k})$ follow by Fourier transforming Eq. (6.7) or, equivalently, taking spherical harmonics of Eq. (6.6).

6.2.3 Emission of one quasar with a preferred alignment

We want to understand the statistical properties of the $j(\mathbf{x},\mathbf{n})$ field accounting for anisotropic emission from the sources. To start, consider a single quasar of luminosity L inside a fixed volume V. Adopting at first an aligned coordinate system such that θ gives the angle to the symmetry axis, and using the geometry of Sec. 6.2.1, we have

$$j_{\mathrm{aligned}}(\theta,\phi) = J \begin{cases} 1 & 0 < \theta < \theta_1 \\ 0 & \theta_1 < \theta < \pi - \theta_1 \\ 1 & \pi - \theta_1 < \theta < \pi \end{cases}, \tag{6.8}$$

where $j_{\mathrm{aligned}}(\theta,\phi)$ indicates the emissivity for the single quasar in our preferred coordinate system, the constant J is defined by $J = L/(4\pi V(1-\cos\theta_1))$, and θ_1 is the angle described in Section 6.2.1 and can have any value in the interval $[0,\pi/2]$.

To proceed further, we decompose the function $j_{\mathrm{aligned}}(\theta,\phi)$ into spherical harmonics $j^{\ell m}_{\mathrm{aligned}}$ according to Eq. (6.7). For our aligned choice of coordinates, we only need to consider $m = 0$ terms because of the cylindrical symmetry around the $\hat{z}$ axis. In this case the spherical harmonic $Y_{\ell 0}(\theta,\phi)$ can be written in terms of a Legendre polynomial, $Y_{\ell 0}(\theta,\phi) = \sqrt{(2l+1)/(4\pi)}P_\ell(\cos\theta)$. Using this result and the recursion relations for P_ℓ, we can express the emissivity variations as

$$J_\ell \equiv j^{\ell 0}_{\mathrm{aligned}} = J \begin{cases} \sqrt{4\pi}(1-\cos\theta_1) & \ell = 0; \\ \sqrt{\frac{\pi}{2\ell+1}}\Big[1-(-1)^{\ell+1}\Big]\Big[P_{\ell-1} - P_{\ell+1}\Big] & \ell > 0, \end{cases} \tag{6.9}$$

where for brevity we have written the Legendre polynomials evaluated at $\cos\theta_1$, i.e. $P_{l-1} \equiv P_{l-1}(\cos\theta_1)$ and $P_{l+1} \equiv P_{l+1}(\cos\theta_1)$.

6.2.4 Emission of N quasars with no preferred alignment

So far we have derived the emissivity for a single quasar in a volume V in terms of the spherical harmonics coefficients. However, we now need to look at the realistic case of N quasars, each with a beam pointing in an independent random direction. To achieve this we first need to drop the assumption of a preferred coordinate system, even for the single-quasar case $N = 1$.

The spherical harmonic coefficients $j^{\ell m}_{N=1}$ for a single quasar pointing in an arbitrary direction are related to the aligned spherical harmonics via the Wigner D matrix, which expresses a rotation by Euler angles ϕ, θ, ψ:

$$\begin{aligned} j^{\ell m}_{N=1} &= \sum_{m'} D^{\ell}_{mm'}(\phi,\theta,\psi)\; j^{\ell m'}_{\rm aligned} \\ &= D^{\ell}_{m0}(\phi,\theta,\psi)\; J_\ell. \end{aligned} \tag{6.10}$$

We are thus only interested in the value of the D matrix when $m' = 0$, for which case we have the identity (Varshalovich et al., 1988):

$$D^{\ell}_{m0}(\phi,\theta,\psi) = \sqrt{\frac{4\pi}{2\ell+1}} Y^*_{\ell m}(\theta,\phi). \tag{6.11}$$

The average emissivity over all possible beam alignment Euler angles is now given by

$$\begin{aligned} \langle j^{\ell m}_{N=1}\rangle_{\phi,\theta,\psi} &\equiv \frac{1}{8\pi^2}\iiint {\rm d}\theta{\rm d}\phi{\rm d}\psi \sin\theta\, D^{\ell}_{m0}(\theta,\phi,\psi)\, J_\ell \\ &= \begin{cases} J_0 & \ell = 0\,; \\ 0 & \ell \neq 0\,. \end{cases} \end{aligned} \tag{6.12}$$

Next we need to calculate the two-point statistic $\langle j^{\ell m}_{N=1} j^{*\ell' m'}_{N=1}\rangle$. Still using a single quasar averaged over all possible directions we obtain

$$\langle j^{\ell m}_{N=1} j^{*\ell' m'}_{N=1}\rangle_{\phi,\theta,\psi} = \frac{1}{2\ell+1} \begin{cases} J^2_\ell & \ell = \ell',\ m = m'\,; \\ 0 & \text{otherwise,} \end{cases} \tag{6.13}$$

where we used the orthogonality properties of the spherical harmonics.

If N sources contribute, the angle-averaged emissivity (6.12) is simply scaled up by a factor N. However the generalisation of the two-point function requires a more careful

analysis. The total emissivity $j_N^{\ell m}$ in this case can be decomposed as the sum of emissivity due to the individual sources,

$$j_N^{\ell m} = \sum_{i=1}^{N} j_{(i)}^{\ell m} \,, \tag{6.14}$$

where $j_{(i)}^{\ell m}$ represents the emission due to the ith source. When taking an average over all possible orientations, each now has its own Euler angles ϕ_i, θ_i, ψ_i. Considering the two-point function,

$$\langle j_N^{\ell m} j_N^{*\ell' m'} \rangle_{\{\phi_i,\theta_i,\psi_i\}} = \sum_{a=1}^{N}\sum_{b=1}^{N} \langle j_{(a)}^{\ell m} j_{(b)}^{\ell' m'} \rangle_{\{\phi_i,\theta_i,\psi_i\}} \,, \tag{6.15}$$

there are now two types of term. First, there are the single-source terms where $a = b$. In these cases, the average over Euler angles is no different from the $N = 1$ case. Since there are N such terms with $a = b$, they contribute N times the result in Eq. (6.13). Second, there are cross-quasar terms where $a \neq b$. These terms involve separately integrating over the Euler angles for both a and b. The decoupled integrals are individually of the form (6.12); each cross-term (of which there are $N^2 - N$ in total) therefore contributes J_0^2 when $\ell = 0$ and zero otherwise. Putting together the results above we find that

$$\langle j_N^{\ell m} j_N^{*\ell' m'} \rangle_{\{\phi_i,\theta_i,\psi_i\}} = \frac{1}{2\ell+1} \begin{cases} N^2 J_0^2 & \ell = \ell' = m = m' = 0 \,; \\ N J_\ell^2 & \ell = \ell' \neq 0, \ m = m' \,; \\ 0 & \text{otherwise.} \end{cases} \tag{6.16}$$

This is the final result for the case of a fixed number of N quasars inside a volume V.

6.2.5 Putting it together: emissivity shot-noise power spectrum

So far we have considered a case where the emissivity inside a fixed volume V with a known number of quasars N is calculated. We now need to introduce fluctuations in N. We expect to have $\langle N \rangle = \bar{n}V$ quasars, where the average is over all possible values of N and $\bar{n}$ is the number density. In the Gaussian limit of Poisson statistics (which should be appropriate on large scales), we also know that the variance in N is given by the relation $\langle N^2 \rangle - \langle N \rangle^2 = \bar{n}V$. Consequently, the statistics for the emissivity j_V in a fixed volume but with varying N are specified by

$$\langle j_V^{\ell m} j_V^{*\ell' m'} \rangle = \frac{1}{2\ell+1} \begin{cases} \left[\bar{n}V + (\bar{n}V)^2\right] J_0^2 & \ell = \ell' = m = m' = 0 \,; \\ \bar{n}V J_\ell^2 & \ell = \ell' \neq 0, \ m = m' \,; \\ 0 & \text{otherwise,} \end{cases} \tag{6.17}$$

where the average is now over all values of N, as well as over the Euler angles ϕ_i, θ_i, ψ_i for each quasar.

To make the connection with the statistics of the $\delta_{j,\mathrm{SN}}$ field introduced in Eq. (6.5), we now define the fractional variations in j in a volume V as $\delta_{j,V}$ where

$$\delta_{j,V}(\vec{n}) \equiv \frac{j_V(\vec{n}) - \langle j_V \rangle}{\langle j_V \rangle}, \tag{6.18}$$

which implies the spherical harmonic expansion is given by

$$\delta_{j,V}^{\ell m} = \frac{j_V^{\ell m} - \langle j_V^{\ell m} \rangle}{\langle j_V^{00} \rangle} \sqrt{4\pi}. \tag{6.19}$$

Using this result alongside Eq. (6.17) we find that $\langle \delta_{j,V}^{\ell m} \rangle = 0$ and

$$\langle \delta_{j,V}^{\ell m} \delta_{j,V}^{*\ell' m'} \rangle = \frac{1}{\bar{n} V} \frac{4\pi}{2\ell + 1} \begin{cases} (J_\ell / J_0)^2 & \ell = \ell',\ m = m'; \\ 0 & \text{otherwise.} \end{cases} \tag{6.20}$$

Finally, the expression for the statistics averaged over a volume V need to be related to the power spectrum of $\delta_{j,\mathrm{SN}}$. We define the source shot-noise power spectrum $P_{j,\mathrm{SN},\ell}(\boldsymbol{k})$ via

$$\langle \tilde{\delta}_{j,\mathrm{SN}}^{\ell m}(\vec{k}) \tilde{\delta}_{j,\mathrm{SN}}^{*\ell' m'}(\vec{k}') \rangle = P_{j,\mathrm{SN},\ell}(\boldsymbol{k}) \delta_{\mathrm{D}}(\boldsymbol{k} - \boldsymbol{k}') \delta_{\ell\ell'} \delta_{mm'}, \tag{6.21}$$

where δ_{D} is the Dirac delta function. To make contact between this required form and the derivation so far, one calculates the fluctuation averaged over a volume V:

$$\begin{aligned} \delta_{j,V}^{\ell m} &\equiv \frac{1}{V} \int_V \mathrm{d}^3 x\, \delta_{j,\mathrm{SN}}^{\ell,m}(\vec{x}) \\ &= \frac{1}{(2\pi)^{3/2} V} \int_V \mathrm{d}^3 x \int \mathrm{d}^3 k\, e^{i\vec{k}\cdot\vec{x}} \tilde{\delta}_{j,\mathrm{SN}}^{\ell,m}(\vec{k}) \delta_{j,\mathrm{SN}}^{\ell,m}(\vec{x}). \end{aligned} \tag{6.22}$$

Making the ansatz that $P_{j,\mathrm{SN},\ell}(k)$ is in fact independent of k (as expected for shot-noise), we find that

$$\langle \delta_{j,V}^{\ell m} \delta_{j,V}^{*\ell' m'} \rangle = \frac{1}{V} P_{j,\mathrm{SN},\ell} \delta_{\ell\ell'} \delta_{mm'}. \tag{6.23}$$

By comparing with Eq. (6.20) one obtains the final result:

$$P_{j,\mathrm{SN},\ell}(k) = \frac{4\pi}{\bar{n}} \frac{(J_\ell / J_0)^2}{2\ell + 1}\,. \tag{6.24}$$

In the case of isotropic emission, $J_\ell = 0$ for $\ell > 0$ and the result (6.24) agrees with that from P14. Note that the shot-noise always scales with the inverse of the mean density $\bar{n}$ (whether or not the emission is isotropic).

6.3 Radiative transfer method

In this Section we expand the P14 linearised radiative transfer equation into a spherical harmonic Boltzmann hierarchy so that we can use the directional source statistics derived in Sec. 6.2. Starting from the physical number density of photons $f(\vec{x}, \vec{n}, \nu)$ at co-moving position $\vec{x}$ traveling in direction $\vec{n}$ with frequency ν, P14 integrates over the frequency dependence ν by defining

$$f_{\rm LL}(\vec{x}, \vec{n}) = \int \mathrm{d}\nu \, f(\vec{x}, \vec{n}, \nu)\sigma_{\rm HI}(\nu), \tag{6.25}$$

analogous to Eq. (6.3). We approximate the radiation and ionisation to be in equilibrium; this is a good approximation at redshift $z \sim 2.3$ (e.g. Busca et al., 2013). The fractional variations around the mean value of $f_{\rm LL}$ are denoted $\delta_{f_{\rm LL}}$; by linearising the Boltzmann equation, P14 obtained

$$\begin{aligned}\left[i(a\,\kappa_{\rm tot,0})^{-1}(\mathbf{n}\cdot\mathbf{k})+1\right]\tilde{\delta}_{f_{\rm LL}}(\mathbf{k},\mathbf{n}) = (1-\beta_{\rm HI}\beta_{\rm r})\tilde{\delta}_j(\mathbf{k},\mathbf{n}) \\ + \beta_{\rm HI}\beta_{\rm r}[\tilde{\delta}_{n_{\rm HI}} + \tilde{\delta}_\Gamma(\vec{k})] - \tilde{\delta}_{\kappa_{\rm tot}}.\end{aligned} \tag{6.26}$$

Here, a is the cosmological scalefactor and $\kappa_{\rm tot}$ an effective opacity to ionising photons (comprised of both physical absorption and corrections from effects such as redshifting). The mean effective opacity is given by $\kappa_{\rm tot,0} \equiv \langle\kappa_{\rm tot}\rangle$ while its fractional fluctuations are specified by $\delta_{\kappa_{\rm tot}}$. The inverse of $a\,\kappa_{\rm tot,0}$ gives the effective comoving mean free path of an ionising photon, which can be estimated to be 350 Mpc at $z = 2.3$ (see P14 Eq. 16). The dimensionless quantities $\beta_{\rm HI}$ and β_r quantify respectively the fraction of effective opacity resulting from physical absorption in the IGM, and the fraction of HI recombinations that result in an emission of a new ionising photon. The appearance of β_r is in fact accounting for ionising photons re-emitted (isotropically) from the IGM itself as mentioned at the start of Section 6.2.2. For full details see P14.

In the same way that Eq. (6.5) decomposes the emissivity into shot-noise and cosmological terms, we can decompose the radiation density fluctuations:

$$\tilde{\delta}_{f_{\rm LL}}(\vec{k}, \vec{n}) = \tilde{\delta}_{f_{\rm LL},\rm SN}(\vec{k}, \vec{n}) + b_{f_{\rm LL}}(\hat{\vec{k}}\cdot\vec{n})\tilde{\delta}_\rho(\vec{k})\,, \tag{6.27}$$

where $b_{f_{\rm LL}}$ is a scale- and direction-dependent bias. At linear order, $\tilde{\delta}_{f_{\rm LL},\rm SN}$ depends only on $\tilde{\delta}_{j,\rm SN}$, not on the cosmological density $\tilde{\delta}_\rho$. In the present analysis we revise only the shot-noise component.

P14 assumes that $\delta_{j,\mathrm{SN}}$ is independent of $\vec{n}$. In our case, we can no longer make this assumption. Instead we write the direction vector $\vec{n} = (\sin\theta\cos\phi, \sin\theta\sin\phi, \cos\theta)$ and, to simplify the analysis, rotate the coordinate system[1] such that the wavevector $\vec{k}$ lies along the $\hat{z}$ axis, i.e. $\vec{k} = (0, 0, k)$. The product $\vec{n}\cdot\vec{k}$ appearing in the radiative transfer equation then expands to

$$\vec{n}\cdot\vec{k} = k\,\cos\theta = \sqrt{\frac{4\pi}{3}}\,k\,Y_{10}(\theta,\phi). \tag{6.28}$$

Using this result in Eq. (6.26) we obtain (see Appendix A.1 for a detailed derivation):

$$\begin{aligned}&\tilde{\delta}^{\ell m}_{f_{\mathrm{LL}},\mathrm{SN}} - \beta_{\mathrm{HI}}\delta^{00}_{f_{\mathrm{LL}},\mathrm{SN}}\delta_{0\ell}\delta_{0m} + \frac{ik}{a\,\kappa_{\mathrm{tot},0}}\times \\ &\left\{\tilde{\delta}^{\ell-1,m}_{f_{\mathrm{LL}},\mathrm{SN}}\sqrt{\frac{(\ell+m)(\ell-m)}{(2\ell-1)(2\ell+1)}} + \tilde{\delta}^{\ell+1,m}_{f_{\mathrm{LL}},\mathrm{SN}}\sqrt{\frac{(\ell+m+1)(\ell-m+1)}{(2\ell+1)(2\ell+3)}}\right\} \\ &\qquad = (1-\beta_{\mathrm{HI}}\beta_{\mathrm{r}})\tilde{\delta}^{\ell m}_{j,\mathrm{SN}}(\vec{k}),\end{aligned} \tag{6.29}$$

where the explicit $\vec{k}$-dependence of $\tilde{\delta}^{\ell m}_{f_{\mathrm{LL}}}$ has been omitted from the expression for brevity. The expression can be rewritten schematically as

$$\sum_{\ell'} M_{m\ell\ell'}(\vec{k})\delta^{\ell' m}_{f_{LL},\mathrm{SN}}(\vec{k}) = (1-\beta_{\mathrm{HI}}\beta_r)\delta^{\ell m}_{j,\mathrm{SN}}(\vec{k}), \tag{6.30}$$

where $M_{m\ell\ell'}(\vec{k})$ contains the appropriate equilibrium radiation transfer coefficients from the left-hand-side of (6.29). We can invert the linear relationship:

$$\tilde{\delta}^{\ell m}_{f_{\mathrm{LL}},\mathrm{SN}}(\vec{k}) = (1-\beta_{\mathrm{HI}}\beta_{\mathrm{r}})\sum_{\ell'} M^{-1}_{m\ell\ell'}(\vec{k})\tilde{\delta}^{\ell' m}_{j,\mathrm{SN}}(\vec{k}), \tag{6.31}$$

where the inverse matrix M^{-1}_m satisfies

$$\sum_{\ell'} M^{-1}_{m\ell\ell'}M_{m\ell'\ell''} = \delta_{\ell\ell''}. \tag{6.32}$$

In our analysis, we are only interested in the overall radiation intensity fluctuations — i.e. the statistical properties of $\tilde{\delta}^{00}_{f_{\mathrm{LL}}}$, or equivalently $\tilde{\delta}_{\Gamma}$. Therefore we need to consider only the $m = 0$ component of Eq. (6.31) since different ms do not couple to each other.

The next step is to solve the inversion (6.31) numerically. For these purposes the hierarchy must be truncated at finite ℓ_{max}, so that we solve a $\ell_{\mathrm{max}} \times \ell_{\mathrm{max}}$ matrix inversion for

[1] This freedom is available because we will ultimately consider only scalar quantities such as the ionisation rate and HI density. Statistical isotropy will then ensure the choice of $\hat{\vec{k}}$ direction in the analysis is irrelevant. Note that our special coordinate system in this section is independent of the temporary special coordinate system temporarily adopted in the early parts of Sec. 6.2.

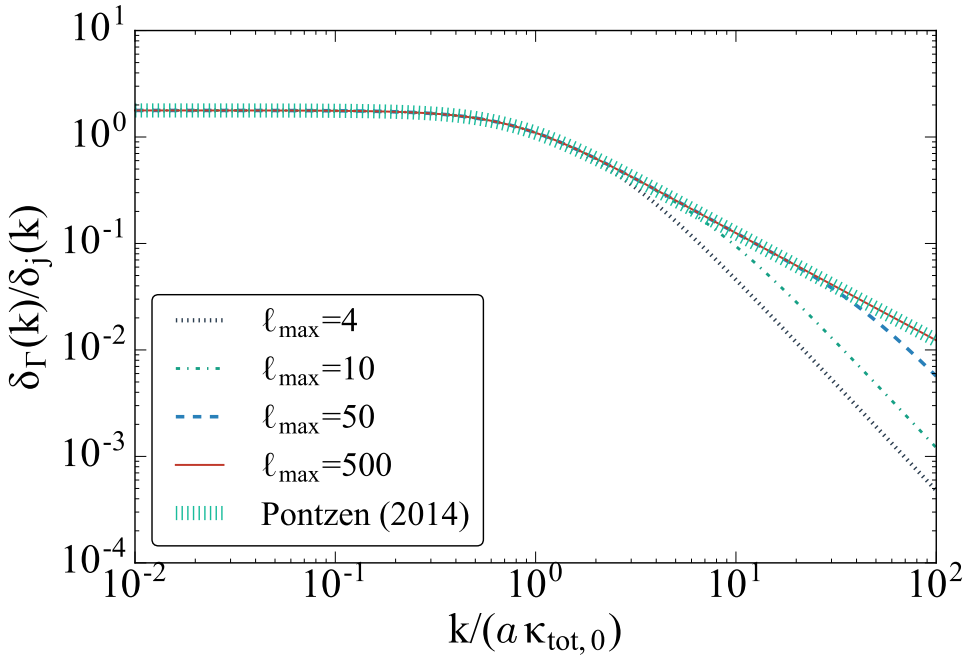

Figure 6.2: Demonstration of convergence of the numerical solution for shotnoise-induced ionisation rate fluctuations $\tilde{\delta}_{\Gamma,\mathrm{SN}}(\vec{k})$ as a fraction of the underlying source fluctuations $\tilde{\delta}_{j,\mathrm{SN}}(\vec{k})$. We choose an isotropic emission case where a closed-form analytic solution (shown by the shading) is known from Pontzen (2014). As ℓ_{max} increases for test values from 4 to 500, our numerical hierarchy converges to this solution.

each k. In practice choosing ℓ_{max} requires a convergence test to ensure that any results are insensitive to the finite truncation.

In the case of an isotropically radiating source, the solution for $\tilde{\delta}_\Gamma$ was written in closed form by Eq. (30) of P14, which can be rearranged (see Appendix A.1) to provide a test case that is illustrated in Fig. 6.2. Specialising our Eq. (6.31) to the isotropic case corresponds to setting $\tilde{\delta}_j^{\ell m}$ to zero for $\ell \neq 0$ and $m \neq 0$. The result for $\delta_\Gamma = \delta^{00}_{f_{\mathrm{LL}}}/\sqrt{4\pi}$ is shown in Fig. 6.2 as a function of $k/(a\,\kappa_{\mathrm{tot},0})$.

Consider first the closed-form solution from P14, shown by the shaded band. The function shows how ionisation rate fluctuations trace emissivity fluctuations on large scales (small k) – the function converges to a fixed, order unity value. On small scales (large k) the fluctuations in the ionisation rate are suppressed: even a point source of radiation can ionise extended regions of space, so the small-scale ionisation rate fluctuations are damped. The transition scale between these behaviours is set by the effective mean free

path $(a\,\kappa_{\rm tot,0})^{-1}$.

As $\ell_{\rm max}$ increases, our new hierarchy solution correctly converges to the closed-form solution (dotted, dash-dotted, dashed and solid lines respectively for $\ell_{\rm max} = 4$, 10, 50 and 500). The long wavelength limit (small k) is completely insensitive to $\ell_{\rm max}$, while the highest k modes are most sensitive. Note that while in this test case the emission is isotropic, the actual radiation field is not; there is a net flux of photons away from the plane wave peaks which defines a preferred direction. This accounts for the sensitivity to $\ell_{\rm max}$; as k becomes large the spacing between peaks becomes small compared to the mean free path of a photon. The true photon distribution is sharply peaked in the $\hat{\vec{k}}$ direction and such sharp directionality requires a high $\ell_{\rm max}$ for an adequate representation.

In the remainder of this paper we set $\ell_{\rm max} = 500$; we verified that increasing $\ell_{\rm max}$ to 1000 did not change our results.

6.4 Results for ionisation rate and HI power spectra

We now have everything required to consider the power spectrum of radiation fluctuations for different source beaming parameters. Again considering only the shot-noise component, we can write

$$P_{\Gamma,\rm SN}(k) = \frac{(1-\beta_{\rm HI}\beta_r)^2}{4\pi}\sum_\ell (M^{-1}_{00\ell}(k))^2 P_{j,{\rm SN},\ell}(k), \tag{6.33}$$

where $P_{j,{\rm SN},\ell}(k)$ is given by Eq. (6.24) and is in fact independent of k.

Figure 6.3 plots $\bar{n}\,P_{\Gamma,SN}(k)$ against the wavenumber for different values of the beam width $\theta_1 = \pi/2, \pi/10$ and $\pi/100$. These correspond to opening angles of $180°$, $36°$ and $3.6°$ respectively; the last of these is exceptionally narrow compared to observational estimates of $\gtrsim 30°$ (Trainor & Steidel, 2013) and should be regarded as an extreme upper limit on the magnitude of the correction.

Because $P_{j,{\rm SN},\ell}(k)$ scales inversely proportionally to the source density $\bar{n}$, the product $\bar{n}\,P_{\Gamma,\rm SN}(k)$ is independent of $\bar{n}$ and a function only of the beam shape. Inspecting this product allows us to isolate and understand the effect of the beaming.

The first case, $\theta_1 = \pi/2$, is plotted with a solid line and recovers the isotropic-emission solution (as previously illustrated by Fig. 6.2). As θ_1 decreases (dashed and dash-dotted lines respectively), the radiation emission is increasingly tightly collimated. The effect of the beaming on $\bar{n}\,P_{\Gamma,\rm SN}(k)$ is, however, confined to large k. At low k, where the mean-free-path $(a\kappa_{\rm tot})^{-1}$ is small compared to the wave under consideration, beaming has no effect

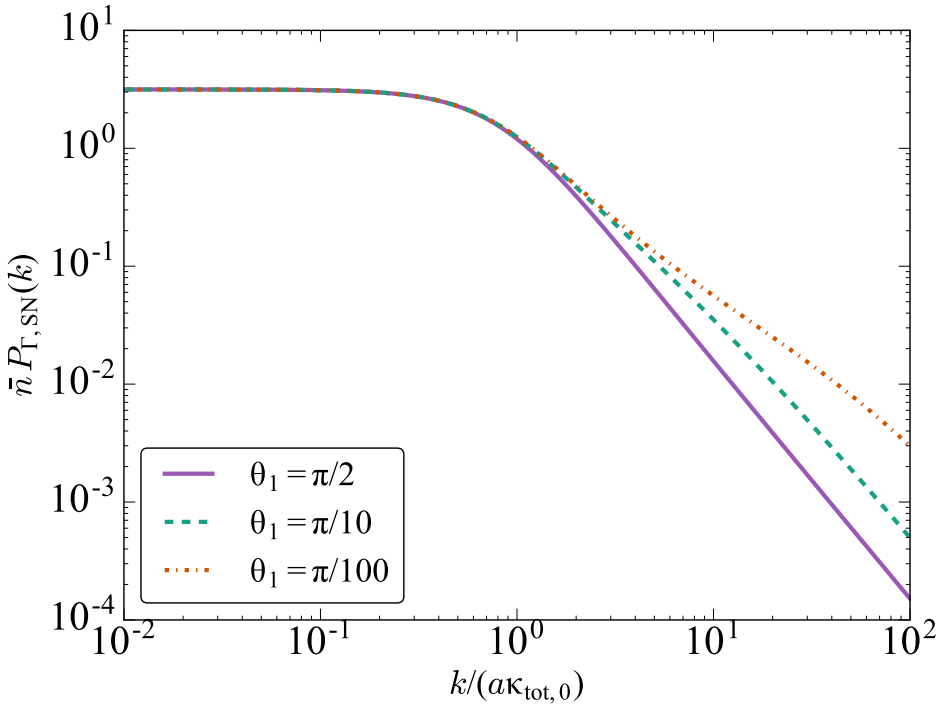

Figure 6.3: Shot noise power spectrum for radiation fluctuations $P_{\Gamma,\mathrm{SN}}(k)$, multiplied by the overall density of sources $\bar{n}$ (which removes the only dependence on $\bar{n}$). For the solid, dashed, and dash-dotted lines the opening angle for the radiation sources is $\pi/2$, $\pi/10$ and $\pi/100$ respectively. The low k radiation fluctuations are independent of the beam angle while at high k the amplitude of fluctuations are increased for narrow beams.

because the local ionising rate scales proportionally to the total photon output of sources. For smaller wavelengths (higher k), narrow beams lead to higher-amplitude fluctuations in the ionising photon field.

Until now we have considered only the shot-noise contribution, but to draw overall conclusions we need to put our revised radiation shot-noise estimates back into the full calculation from P14. Because the shot-noise is uncorrelated with the cosmological fluctuations in the first-order analysis, the power spectra add linearly:

$$\mathrm{P_{HI}}(k) = b_{\mathrm{HI}}^2(k)\mathrm{P}_\rho(k) + \mathrm{P_{HI,SN}}(k), \tag{6.34}$$

where $P_\rho(k)$ is the dark matter density power spectrum and b_{HI} is the linear relationship between HI density and the total density as a function of scale, which is unchanged from P14. Finally, because $\delta_{n_{\mathrm{HI}},\mathrm{SN}} = -\delta_{\Gamma,\mathrm{SN}}$, the shot-noise power spectra for HI and Γ are

equal and we have

$$\mathrm{P_{HI}}(k) = b_{\mathrm{HI}}^2 \mathrm{P}_\rho(\vec{k}) + \mathrm{P}_{\Gamma,\mathrm{SN}}(\vec{k}), \tag{6.35}$$

which allows us to use the result obtained in Eq. (6.33) for our beamed shot-noise estimates.

Figure 6.4 shows the total power spectrum for the three values of θ_1 previously adopted and a fixed density of observed sources $\bar{n}_{\mathrm{obs}} = 1 \times 10^{-4}\ h^3\ \mathrm{Mpc}^{-3}$, a value adopted directly from P14. Note that, for our present investigation, we assume that all sources have the same opening angle (in particular ignoring the distinction between quasars and galaxies in this respect). Even if galaxies contribute comparable or larger number of photons to the overall background, the shot-noise is still strongly dominated by quasars (P14) and so this approximation is likely valid.

As in P14, radiation can be approximated as near-uniform for the power spectrum on scales below the mean-free-path (for $k \gg 0.01\,h/\mathrm{Mpc}$); consequently the corrections from the fluctuating ionisation always increase towards large scales. On very large scales ($k < 0.01\,h/\mathrm{Mpc}$), radiation fluctuations actually dominate over H density fluctuations in the HI power spectrum. At the transition scale, there is a characteristic dip where the radiation and H density fluctuations approximately cancel. These basic features are preserved when beaming is included.

As the source beams narrow, the results in Fig. 6.4 show that the primary effect is to reduce the amplitude of shot-noise fluctuations in the very large scale regime ($k \ll 0.01\,h/\mathrm{Mpc}$) through the renormalisation discussed in Sec. 6.2.1. Unlike the direct effect of the beam, this observational correction to the inferred number densities applies equally over all scales, making it extremely significant in the low-k regime where shot-noise dominates. However note that the constraining effect of current and future surveys is quite poor on such extreme scales (Pontzen et al., 2014; Bautista et al., 2017). At scales $k \sim 0.04\,h/\mathrm{Mpc}$, where reasonable observational precision can be expected in future pipelines, the effects of beaming are considerably more modest constituting a $\lesssim 5\,\%$ correction. In this regime, the decreased power from the source density renormalization is partially cancelled by the increased power from the beaming itself (Figure 6.3).

Because the effects are so strongly scale-dependent, and survey sensitivities are also a steep function of scale, the observability of beaming will be strongly dependent on details of observing strategy and pipelines.

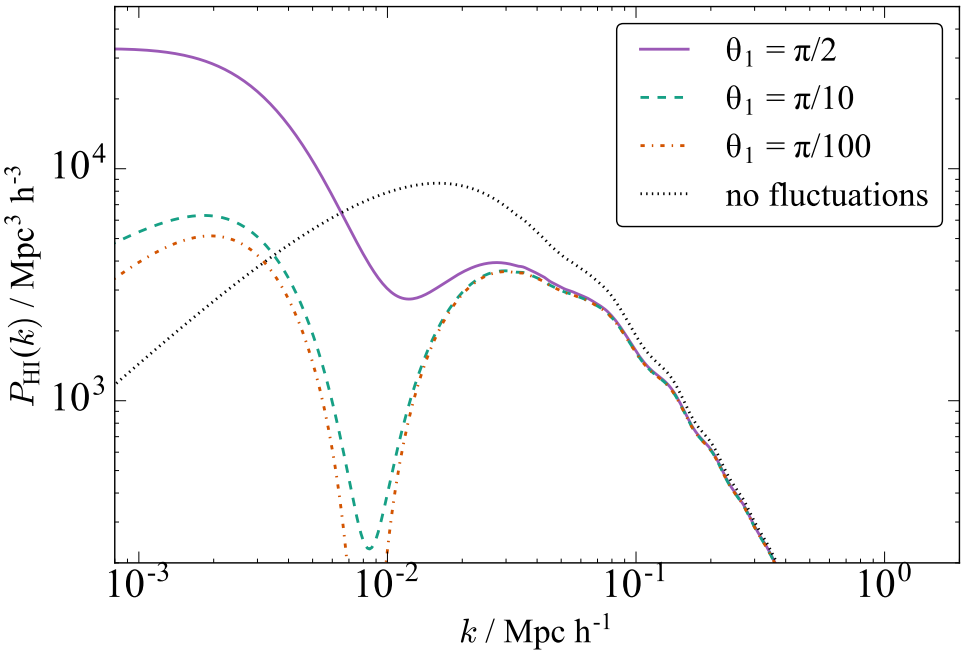

Figure 6.4: Power spectrum of the HI fluctuations defined by Eq. (6.35), evaluated at redshift $z \simeq 2.3$ for a fixed observed source density of $\bar{n}_{\rm obs} = 10^{-4}\ h^3\ {\rm Mpc}^{-3}$, and for the same range of beam widths θ_1 adopted in Fig. 6.3. All other parameters are set to the defaults from Pontzen (2014). The dominant effect of changing θ_1 arises from the rescaling of $\bar{n}$ to match $\bar{n}_{\rm obs}$; this can be seen on the largest scales (small k) where shot-noise effects dominate. The dotted line shows, for reference, the HI power spectrum in the unphysical limit where there are no UV fluctuations.

6.5 Summary and discussion

UV background fluctuations can significantly impact the Ly-α forest, being one important contributor of large-scale power. In this paper, three physical effects have been taken into account: the finite number of the ionising sources, their inhomogeneous distribution, and the radiative transfer through neutral gas in the IGM.

The effects of large-scale inhomogeneities used to be considered negligible based on results from simulations that compared the effects of non-uniform and uniform ionising radiation background in the synthetic Lyman-α forest at high redshifts (Croft et al., 1999; Gnedin & Hamilton, 2002).

Later on, both particle-mesh (PM) and large-scale N-body simulations of the Lyman α forest showed that the background fluctuations increase the large-scale power (Meiksin & White, 2004; White et al., 2010) and suppress the power at intermediate scales, as much as 15 per cent at $k = 0.05 - 1$ h Mpc^1 e.g., Croft (2004). Additionally, these simulations showed that the large-scale power seems to grow rapidly at higher redshifts, suggesting a quasar-dominated UV background, rather than having more abundant sources such as galaxies (McDonald et al., 2005).

In this work we have constructed an analytical model to treat fluctuations in the cosmological UV background taking into account, for the first time, anisotropy due to phenomena such as quasar beaming. To do that, we built upon the monochromatic, equilibrium, large-scale description presented in Pontzen (2014) but included angle-dependent emission terms.

We first introduced a correction for the observational bias that individual quasars are less likely to be detected if they are tightly beamed. This renormalises the underlying density of quasars in the Universe. We then derived the emissivity shot-noise power spectrum corresponding to a distribution of quasars each pointing in a randomised direction. This required adopting an underlying beaming model; for simplicity we used a hard-edged beam of fixed opening angle $2\theta_1$ for the entire population (Fig. 6.1). Finally, we rederived the radiative transfer for the shot-noise taking into account the new angle-dependence. These results are most naturally expressed in terms of a hierarchy of spherical harmonic coefficients; because we are only interested in the overall radiation intensity fluctuations we ultimately took the $\ell = 0$, $m = 0$ component.

We solved the new hierarchy numerically and showed that, for sufficiently large $\ell_{\max}$,

the method converges to the known isotropic-emission case when $\theta_1 = \pi/2$ (see Fig. 6.2) demonstrating the accuracy of the method. Then, we explored the effects of the quasar beam width on the shot-noise (Fig. 6.3).

The shot-noise power spectrum of radiation fluctuations $P_{\Gamma,\mathrm{SN}}$ in Fig. 6.3 shows that the fluctuations are not sensitive to the beam angle at low k. Fluctuation amplitudes do increase at high k for narrower beams; however the effect is modest even for extreme values of the beam width θ_1.

When combining the new shot-noise solution with the cosmological density fluctuations (Fig. 6.4), we found that the primary effect of beaming is in fact the first and simplest one: the observational renormalisation of the underlying density of bright sources. This affects all k-modes equally (scaling up and down the overall contribution of shot-noise) and therefore is highly significant on large scales (small k) where the shot-noise potentially dominates over the cosmological signal.

Radiative transfer through a filamentary IGM has been found, using numerical simulations, to significantly contribute to the fluctuations in the UV background (Maselli & Ferrara, 2005), which are tightly correlated to the density field.

This paper has focussed on clarifying one area where the effects of radiative transfer on the Lyman-alpha forest were not known. If future pipelines lead to constraints on the magnitude of this effect (e.g. Pontzen et al., 2014; Bautista et al., 2017), there are a number of other possible influences that still require to be understood. For example, time variability of sources and the effects of patchy heating (Greig et al., 2015) still need to be incorporated in a coherent framework and will be tackled in future work.

Including thermal fluctuations in our modelling could help the study of the thermal impact of HeII reionisation at $z \sim 2.5$ and constrain models for the sources of the ionising background (McQuinn et al., 2011) with forthcoming surveys (e.g. BOSS). Spectroscopic data at higher redshifts could potentially detect the thermal imprint of hydrogen reionisation.

Chapter 7

Conclusions & future work

7.1 Summary

Galactic winds are observed in star-forming galaxies at all redshifts (e.g. Bordoloi et al., 2014; von Glasow et al., 2013). The relations between physical properties such as gas and metal content evolve with redshift. The multi-phase nature of the gas in the CGM makes modelling necessary to understand the mechanisms behind these components. It is well established from observations that galaxies expel star-forming gas, but, is not very clear how far they can travel. The presence of cool gas far from the galactic centre leaves the question of how this material travelled so far without being disrupted.

Using two-dimensional hydrodynamical simulations, we explored the possibility that cool gas is formed by in situ radiative cooling (Suarez et al., 2016). We studied the evolution of hot gas from the galactic disk traversing the halo without simulating the disk. To ensure the effects are a result of outflows, we tested equilibrium inflows as shown in Eqs. (4.7) – (4.9). We adopted a suitable cooling function ($\dot{Q}_{\rm cool}$) for primordial gas, giving a lower bound on realistic cooling rates.

We found that the characteristics of outflows are strongly parameter dependent. In particular, we varied the overall star formation cycle length, $t_{\rm cyc}$, and the fraction of that time spent pumping gas into the CGM, $f_{\rm cyc}$, while keeping the total energy injection and mass loading constant. We found a connection between these two parameters and the nature of the outflow. Our simulations are able to produce cool gas ($T < 5 \times 10^4\,{\rm K}$). This cooler fraction is able to form as a result of cooling shocks propagating outwards. Shocks are disrupted when new material is injected behind the shock. Overall, we are able to identify two regimes: small $f_{\rm cyc}$ corresponding to rapid SFR fluctuation in combination with large $t_{\rm cyc}$ (greater than few hundred Myr) triggers waves of effective cooling

that travel through the halo; and, long time periods $\gtrsim 1$ Gyr (corresponding to large $f_{\rm cyc}$) form a turbulent halo. Our results suggest that steady flow solutions with cooling set a lower bound on the amount of in situ cooling to be expected in realistic galaxies with time-varying feedback. The results from these parameter sampling in two dimensions would be useful to interpret the CGM around galaxies in cosmological simulations. This two-dimensional analysis is rather simplistic to be able to compare directly with observations. A three-dimensional analysis would be the next step to study the sample parameterisation presented in this work. Detailed behaviour in three dimensions could differ significantly. More realistic simulations are far more complex. These would include metal enrichment, effects of thermal conductions and magnetic fields. I expand on these aspects in the next Sec. 7.2.

The transition of the neutral hydrogen ground state forms the most abundant features in the spectra of background QSOs in the rest-frame ultraviolet, making it the best way to detect clouds of gas along the line-of-sight. The second project of this thesis focused on one of the effects that radiative transfer (RT) has on the Lyman α forest. In Chapter 6 (Suarez & Pontzen, 2017) a model to treat fluctuations in the UV background is presented as an extension of the large-scale description of Pontzen (2014). The new model includes angle-dependent emission terms that takes the probability of a quasar to be observationally detected into account. This is reflected as a renormalisation of the underlying density of quasars together with an updated radiative transfer model. We derived the shot-noise power spectrum for a random distribution of quasars. We adopted a hard-edged beaming model for the entire population. The equation results in a hierarchy in terms of spherical harmonics with solutions $\ell = 0, ..., \ell_{\rm max}$, $m = 0$. We verified that the method converges for sufficiently large $\ell_{\rm max}$, directly. We studied the effects of quasar beam width and found that radiation fluctuations are not sensitive to the beam angle at low frequencies k, as shown in Fig. 6.3. The model, however, is sensitive at high k where the fluctuation amplitude increase for narrower beams. Moreover, the observational renormalisation strongly affects all scales.

We then calculated the total power spectrum of the HI fluctuations, considering the shot-noise solution mentioned above in the cosmological density fluctuations. The effect of beaming affects all k-modes being highly significant on large scales (small k), where the shot-noise dominates over the cosmological signal.

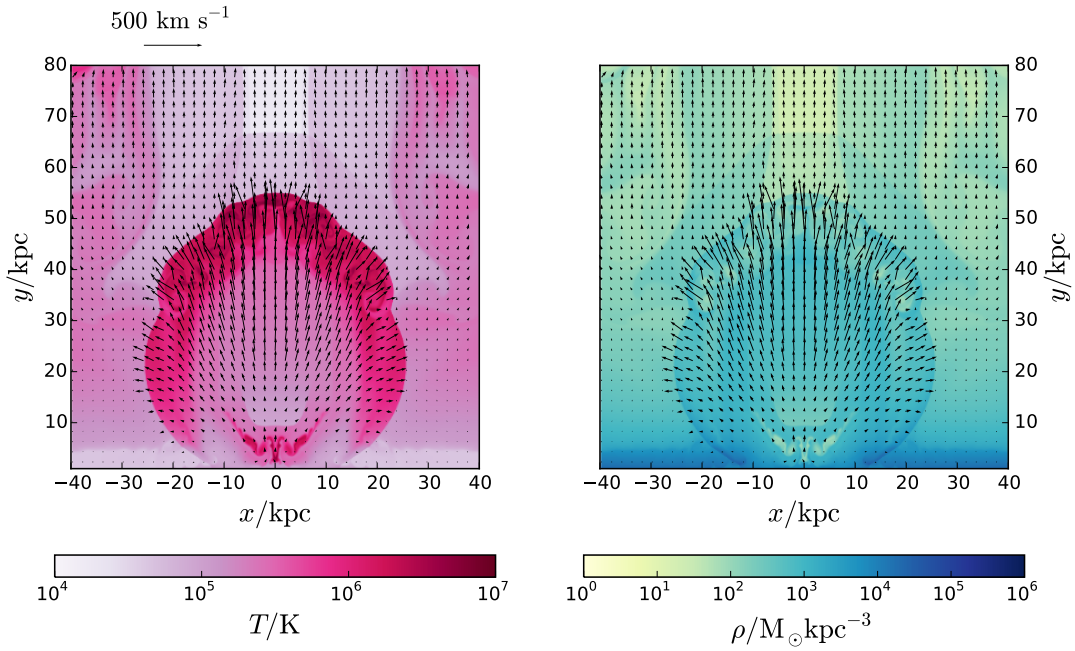

Figure 7.1: An example of a simulated outflow with double resolution than the simulations presented in Chap. 4. The snapshot shows the temperature (left) and density (right) of a shock-type outflow. Black arrows denote velocity vectors.

7.2 Proposals for future work

In this section I present possible extension of my work. I start by presenting potential improvements to the hydrodynamical simulations present in Chap. 4 in order to produce more realistic models for outflows. Then, I briefly discuss some possible extensions to the work in Chap. 6.

7.2.1 Higher resolution and three dimensional simulations

When performing 3D simulations, the results are expected to differ from the two dimensional analysis because turbulence is crucial for the gas mixing, which cannot be properly addressed in two dimensions (Quilis et al., 2001). My two-dimensional simulations can be extended to a study of solutions in three dimensions. Although 3D simulations are relatively slow to run, by choosing a subset of the wide parameter space in 2D, I would systematically compare 2D and 3D results. I hope extending this work to a three dimensional space to be useful to interpret cosmological galaxy formation simulations.

7.2.2 Magnetic fields and metal enrichment

In this section, I expand on possible effects such as magnetic fields and metal enrichment that might affect galaxy outflows.

Thermal conduction and magnetic fields

The formation and lifetime of clouds of gas in galactic environments are strongly affected by electron thermal conduction and magnetic fields. RAMSES can be compiled with a magnetohydrodynamic (MHD) solver. Initially, uniform magnetic fields could be implemented in my idealised simulations: a magnetic field parallel to the shock velocity or to model a field perpendicular to the velocity. This study is of particular interest because the presence of magnetic fields can prevent the destruction of the cloud. I can extend the idealised simulations using RAMSES allowing MHD treatment of the shocks. Estimations of the magnetic field in the plasma of the intra-cluster medium (ICM) are in the range of 0.1-10 μG for temperatures between $10^7 - 10^8$ K and densities in $10^{-3} - 10^{-1}$ cm^{-3} (Parrish et al., 2009). I would intend to compare the crushing and fragmentation times in the clouds of these simulations with the field-free case performed with the pure hydro solver. Some authors discuss the nature of magnetic fields and the importance of MHD simulations (Scannapieco & Brüggen, 2015). Including magnetic fields in my simulations will help to better understand the evolution of cold gas clouds.

Metal enrichment

Ejected gas is likely to be strongly metal-enriched. In future I would like to carry out simulations to study the effects of metals on the cooling processes by repeating my simulations with solar composition and study how things differ.

While metallicity in outflows tends to be subsolar as $Z \lesssim Z_\odot$ (Erb et al., 2006) my new simulations would set up upper limits on the importance of metals. The implementation of these important aspects to the idealised simulations will allow me to overcome some of the limitations that the study of outflows in cosmological runs have. Due to resolution limitations, cosmological simulations usually have poor performance regarding the metal mixing. This leads to overestimate densities, which could result in an overcooling problem (Schaye et al., 2015). Cosmological simulations usually have low resolution affecting the total metal masses. It has been proved that increasing the resolution has an important impact in the estimation of metal mass (Wiersma et al., 2009). Idealised hydrodynamical simulations provide higher resolution and the flexibility of tackle each of the problems above separately, and so by making my simulations more realistic I would be

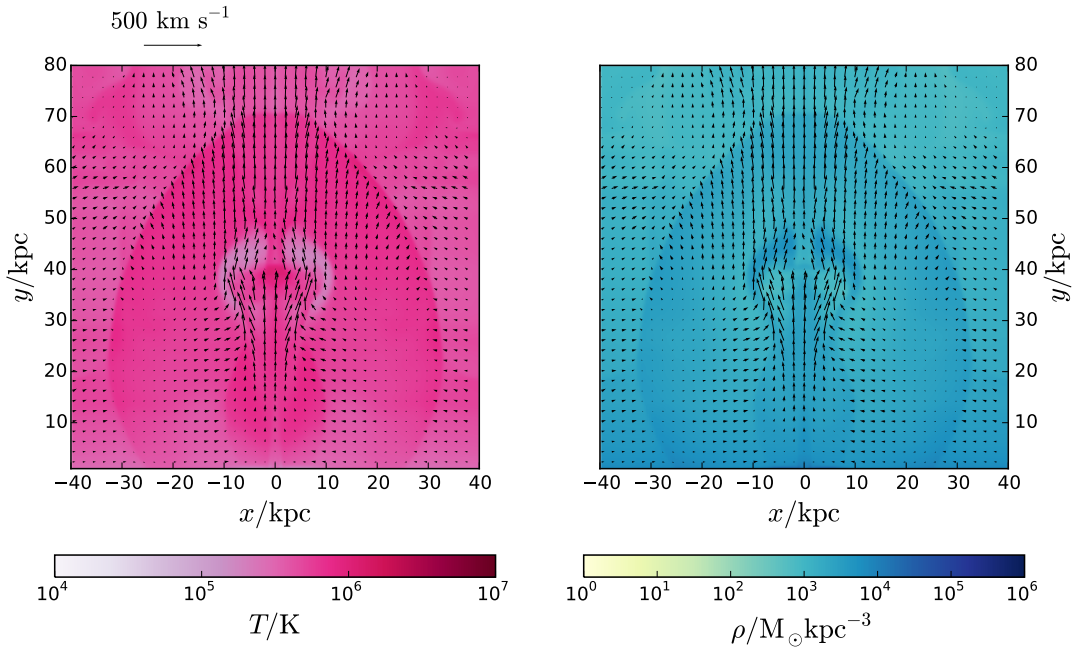

Figure 7.2: An example of a simulated outflow extending to three dimensions in Chap. 4. The snapshot shows a 2D cut of a shock-type outflow using the same initial conditions than Fig. (7.1), showing morphological differences between the 2D and 3D solutions.

able to help interpret current and future observations.

7.2.3 Cosmological simulations

I would nonetheless also like to study whether the cooling effects seen in my idealised runs can be reproduced in a full cosmological context.

Since outflows are thought to come from star-forming galaxies, it is important to study the effect of the feedback recipe in cosmological simulations. I will address the relation between the galactic outflows and the local stellar feedback. Although some improvements have been made, the efficiency of stellar feedback is still simplified and generalised in cosmological simulations e.g., Illustris (Vogelsberger et al., 2014; Sijacki et al., 2015) or EAGLE (Schaye et al., 2015). High resolution numerical simulations produce a more efficient feedback, by reducing numerical radiative losses. I would like to rerun some small portion of cosmological code, either publicly available or to develop my own code, with a different feedback to compare the general effects that steady-state star formation activity has in generating galactic winds as opposite to strong bursts. This will give me the

flexibility to vary the prescription of feedback and study their effects in the generated outflows.

7.2.4 Connecting to observations

There is significant interest in study the formation of cool gas, mechanisms to transport metals into the IGM and the role of starburst galaxies in the enrichment of the intergalactic medium (Erb, 2015). This motivation comes from observational results that show the presence of metals at large distances from the galaxy (Bordoloi et al., 2014). The final goal of the parameter study in idealised simulations and full cosmological simulations is to be able to compare with observational data. I will need to post-process my 3D simulations with equilibrium ionisation models to obtain the distribution of ions, which I can then compare to observations.

7.2.5 Extensions to the Lyman α forest

In this section I present possible extensions to the work presented in Chapter 6, where we modelled the radiative transfer to see the impact of ionisation fluctuations on the statistics of the Lyman alpha forest when considering beamed sources.

Lyman-α multi-broadband

I introduced corrections to estimate the effects of anisotropy in the photon emission from quasar beaming. These calculations have been performed under a monochromatic approximation. I am interested in studying the effects of radiative transfer on the Ly-α forest extending the formulation of anisotropy (described above), in a broadband context. The main goal would be to study how thermal fluctuations change the large-scale signal by incorporating multi-wavelength radiative transfer to my existent framework.

Lyman-α cross-correlation with cosmological simulations

In Chap. 6 I modelled the radiative transfer to see the impact of ionisation fluctuations on the statistics of the Lyman-α forest when considering beamed sources. Those analytical models can be useful when exploring systematic effect with mock spectra. Examples for such type of effects are the continuum from the quasar itself or the distribution of

quasars. I would like to explore the impact of the UV background fluctuations on the three point correlation function (3PCF) in the Lyman α forest.

A fluctuation in the Lymanα forest is defined by Eq. (5.11), and, can be expanded in the linear regime as

$$\delta_\alpha = b_m \delta_m + b_\Gamma \delta_\Gamma, \tag{7.1}$$

where b_Γ is the bias of the photoionisation rate and δ_Γ is a fluctuation in the radiation. Both b_m and b_Γ can be modelled as shown in Pontzen (2014) or Gontcho A Gontcho et al. (2014), or any other approach. Studying the impact of fluctuations in the UV ionising background imply the study of how b_m and b_Γ affect the 3PCF of Lyman-α, including all the three point correlation functions involving quasars and Lyman-α. If the UV background fluctuation is ignored, $b_\Gamma = 0$, then only the matter fluctuation survives. If current (cosmological) simulations already implement the UV background, it should be relatively straight forward to modify the models for b_Γ and δ_Γ.

7.3 Forthcoming surveys

As mentioned in Chap. (1), Lyα and metal absorption lines and Lyα probe the matter content in the high-redshift Universe. Observations from the spectra of quasars have advanced our knowledge of the relationship between ionised species and kinematics of material in the CGM. Most of the analysis and modelling presented in this work was motivated by observational results provided by surveys such as BOSS from SDSS. In addition, the HST/COS surveys have been a key ingredient for our current understanding of the dynamics of the CGM. Observations from COS have been essential for the diagnosis of the CGM, which is composed by a multiphase gas and it is associated to galaxies with diverse masses, providing insight in the CGM multiphase structure. The relationship between the CGM with its host galaxies can be improved with data taken with further instrumentation such as COS.

Future optical and infrared surveys will increase the number of known high-redshift quasars. For instance, James Webb Space Telescope (JWST) will be able to search for faint galaxies near quasars (Stiavelli, 2007). Also, X-ray observations from the mission Advanced Telescope for High Energy Astrophysics (ATHENA) will focus on the cosmic evolution of hot gas in the IGM and CGM.

Fainter sources and more distant sources will also be accessible with future ground-

based surveys (e.g. eBOSS, Comparat et al., 2016). The forthcoming WEAVE-QSO survey (Pieri et al., 2016) will start operation in 2018, mapping the Ly-α forest at redshifts $z > 2$. The data from WEAVE aims to explore the acceleration in the expansion of the Universe, provide constraints on the neutrino masses and warm dark matter. Moreover, with regard to galaxy formation, WEAVE will supply data to study the properties (such as density, temperature, UV radiation, metallicity and abundance pattern) of large-scale inflowing/outflowing gas associated with galaxies, under a cosmological context.

High precision measurements using the Lyα forest technique will probe the large-scale structure of the universe with high accuracy. Given the upgraded facilities and data in the near future, constraints from the Lyα forest will require careful simulation (McDonald et al., 2005) and assessment from forecast is necessary (DESI Collaboration et al., 2016). One of the utilities of such modelling is to understand the uncertainties and error estimations obtainable by surveys.

Appendix A

Derivation of the Boltzmann equation

A.1 Derivation of the radiative transfer hierarchy for anisotropic emission

In this Appendix we present a derivation of our equilibrium hierarchy, Eq. (6.29), starting from the Boltzmann equation (6.26) which itself was previously derived in P14. As stated in the main text, we choose a coordinate system in which the wavevector $\vec{k}$ lies along the $\hat{z}$ axis, allowing us to rewrite $\vec{n} \cdot \vec{k}$ in terms of Y_1^0; see Eq. (6.28).

To extract the spherical harmonic hierarchy, we expand all angular dependences; for any function F one has

$$F(\vec{x}, \vec{n}) = \sum_{\ell', m'} F^{\ell' m'}(\vec{x}) Y_{\ell' m'}(\vec{n}), \tag{A.1}$$

which is the inverse of the defining relation (6.7). We then multiply both sides of Eq. (6.29) by $Y^*_{\ell' m'}(\vec{n})$ and integrate over all angles $\vec{n}$. The left-hand-side becomes

$$\begin{aligned} \mathrm{LHS} = \frac{ik}{a\kappa_{\mathrm{tot},0}} \sqrt{\frac{4\pi}{3}} \iint \mathrm{d}^2\vec{n} \sum_{\ell', m'} \tilde{\delta}^{\ell' m'}_{f_{\mathrm{LL}}}(\mathbf{k}) Y_{\ell' m'}(\vec{n}) Y_{1,0}(\vec{n}) Y^*_{\ell m}(\vec{n}) \\ + \delta^{\ell m}_{f_{\mathrm{LL}}}(\mathbf{k}), \end{aligned} \tag{A.2}$$

where to obtain the last term we have applied the orthogonality relation between spherical harmonics. The first term can be simplified by applying a special case of the Wigner $3j$-symbol (Varshalovich et al., 1988):

$$\iint \mathrm{d}^2\vec{n}\, Y_L^M(\vec{n}) Y_1^0(\vec{n}) Y^{*M}_{L+1}(\vec{n}) = \sqrt{\frac{3(L+M+1)(L-M+1)}{4\pi(2L+1)(2L+3)}}. \tag{A.3}$$

This identity can be used to calculate the integral for two values of ℓ' in the sum given by (A.2), namely $\ell' = \ell \pm 1$. The $\ell' = \ell + 1$ case is obtained by a relabelling of the indices whereas the $\ell' = \ell - 1$ case is obtained by taking the complex conjugate of Eq. (A.3). By

the triangle condition, integrals for any other value of ℓ' vanish. Consequently we may write the LHS of our expression as

$$\begin{aligned}\text{LHS} =& \frac{ik}{a\,\kappa_{\text{tot},0}}\left\{\sqrt{\frac{(\ell+m)(\ell-m)}{(2\ell-1)(2\ell+1)}}\tilde{\delta}_{f_{LL}}^{\ell-1,m}(\vec{k})\right. \\ &\left. + \sqrt{\frac{(\ell+m+1)(\ell-m+1)}{(2\ell+1)(2\ell+3)}}\tilde{\delta}_{f_{LL}}^{\ell+1,m}(\vec{k})\right\} + \tilde{\delta}_{f_{LL}}^{\ell m}(\mathbf{k}).\end{aligned} \tag{A.4}$$

We now turn to the right-hand-side of Eq. (6.29), again multiplying by $Y^*_{\ell m}(\vec{n})$ and integrating over all angles $\vec{n}$. Only $\tilde{\delta}_j$ has any angular dependence on the RHS; the orthogonality of the spherical harmonics picks out the coefficients $\tilde{\delta}_j^{\ell m}$ for this term. For all other terms, only the $\ell = 0$, $m = 0$ case survives the integration. The result is that

$$\begin{aligned}\text{RHS} =& (1-\beta_{\text{HI}}\beta_r)\tilde{\delta}_j^{\ell m}(\mathbf{k}) \\ &+ \frac{\delta_{\ell 0}\delta_{m0}}{\sqrt{4\pi}}\left[\beta_{\text{HI}}\beta_r\left(\tilde{\delta}_{n_{\text{HI}}}(\vec{k}) + \tilde{\delta}_\Gamma(\vec{k})\right) - \tilde{\delta}_{\kappa_{\text{tot}}}(\vec{k})\right].\end{aligned} \tag{A.5}$$

As expressed by Eq. (6.27), we wish to separate the radiation fluctuations that are correlated with the cosmological density field δ_ρ from those that are caused by shot-noise. To do so, we need to transform some of the terms on the RHS which mix the two types of fluctuation as follows.

The terms $\tilde{\delta}_{n_{\text{HI}}}$ and $\tilde{\delta}_\Gamma$ do not have an angular dependence and their relationships are therefore unchanged compared to P14:

$$\tilde{\delta}_{n_{\text{HI}}} = \tilde{\delta}_{n_{\text{HI},u}} - \tilde{\delta}_\Gamma; \quad \tilde{\delta}_{\kappa_{\text{tot}}} = \beta_{\text{HI}}\tilde{\delta}_{n_{\text{HI}}} + \beta_{\text{clump}}\tilde{\delta}_{\kappa_{\text{clump}}}\,. \tag{A.6}$$

The first of these relations arises from the fact that n_{HI} is inversely proportional to the ionisation rate per HI atom, recovering the completely uniform ionising background in the absence of any radiative fluctuations, $\tilde{\delta}_{\text{n}_{\text{HI,u}}}$. The effective opacity fluctuations $\delta_{\kappa_{\text{tot}}}$ definition is a linear combination of the intergalactic medium absorption fluctuations and the self-shielded clump opacity fluctuations.

We can use these relations to rewrite Eq. (A.5) in terms of $\tilde{\delta}_\Gamma$, $\tilde{\delta}_{n_{\text{HI},u}}$ and $\tilde{\delta}_{\kappa_{\text{clump}}}$. The ionisation rate fluctuations $\tilde{\delta}_\Gamma$ are defined by the fluctuations in the photon density $\tilde{\delta}_{f_{\text{LL}}}$ via the relation

$$\delta_\Gamma = \frac{1}{4\pi}\int \text{d}^2n\,\tilde{\delta}_{f_{LL}}(\vec{k},\vec{n}) = \frac{1}{\sqrt{4\pi}}\tilde{\delta}^{00}_{f_{\text{LL}}}(\vec{k}). \tag{A.7}$$

Consequently $\tilde{\delta}_\Gamma$ can be split into a correlated and shot-noise component, with $\tilde{\delta}_{\Gamma,\text{SN}} \equiv \delta^{00}_{f_{\text{LL}},\text{SN}}/\sqrt{4\pi}$.

Using the above transformations, we find the RHS can be written

$$\begin{aligned}\text{RHS} = (1-\beta_{\rm HI}\beta_r)\tilde{\delta}_j^{\ell m}(\vec{k}) + \beta_{\rm HI}\delta_{\ell 0}\delta_{m0}\tilde{\delta}^{00}_{f_{\rm LL}}(\vec{k}) \\ + \left(\beta_{\rm HI}\left(\beta_r - 1\right)\tilde{\delta}_{n_{{\rm HI},u}}(\vec{k}) - \beta_{\rm clump}\tilde{\delta}_{\kappa_{\rm clump}}\right)\delta_{\ell 0}\delta_{m0}.\end{aligned} \tag{A.8}$$

We now apply the decomposition into cosmological and shot-noise components for $\tilde{\delta}_j$ and $\tilde{\delta}_{f_{\rm LL}}$ keeping only the shot-noise contributions. (By linearity, the two types of contribution can be treated independently and the cosmological terms are unchanged from P14.) In particular, the terms $\delta_{n_{{\rm HI},u}}$ and $\delta_{\kappa_{\rm clump}}$ are independent of radiation fluctuations; consequently they have no shot-noise component and drop out entirely. Combining Eqs. (A.4) and (A.8) one reaches the final equation:

$$\begin{aligned}\tilde{\delta}^{\ell m}_{f_{\rm LL},{\rm SN}}(\vec{k}) - \beta_{\rm HI}\delta^{00}_{f_{\rm LL},{\rm SN}}(\vec{k})\delta_{0\ell}\delta_{0m} \\ + \frac{ik}{a\,\kappa_{{\rm tot},0}} \times \Bigg\{\sqrt{\frac{(\ell+m)(\ell-m)}{(2\ell-1)(2\ell+1)}}\tilde{\delta}^{\ell-1,m}_{f_{\rm LL},{\rm SN}}(\vec{k}) \\ + \sqrt{\frac{(\ell+m+1)(\ell-m+1)}{(2\ell+1)(2\ell+3)}}\tilde{\delta}^{\ell+1,m}_{f_{\rm LL},{\rm SN}}(\vec{k})\Bigg\} \\ = (1-\beta_{\rm HI}\beta_{\rm r})\tilde{\delta}^{\ell m}_{j,{\rm SN}}(\vec{k}),\end{aligned} \tag{A.9}$$

which agrees with the expression (6.29) provided in the main text.

In Sec. 6.3 we compared the solution to this hierarchy with the known isotropic limit. For these purposes we need to extract the shot-noise-only isotropic solution in a way that was not written in P14, although it is implicit in P14 Eq. (38). Starting from P14's Eq. (30), we apply our Eq. (A.6) and again retain only those terms which are not correlated with $\tilde{\delta}_\rho$. This yields

$$\begin{aligned}\tilde{\delta}_{\Gamma,{\rm SN,iso}}(\vec{k}) = \frac{(1-\beta_{\rm HI}\beta_{\rm r})S(k)}{1-\beta_{\rm HI}S(k)}\tilde{\delta}_{j,{\rm SN,iso}}(\vec{k}), \\ \text{where } S(k) = \frac{a\kappa_{{\rm tot},0}}{k}\arctan\frac{k}{a\kappa_{{\rm tot},0}},\end{aligned} \tag{A.10}$$

for the isotropic comparison case which is plotted as a shaded band in Fig. 6.2.

Bibliography

Aarseth S. J., Fall S. M., 1980, ApJ, 236, 43

Adelberger K. L., Steidel C. C., Pettini M., Shapley A. E., Reddy N. A., Erb D. K., 2005, ApJ, 619, 697

Ajiki M., Taniguchi Y., Murayama T., Nagao T., Veilleux S., Shioya Y., Fujita S. S., Kakazu Y. et al, 2002, ApJ, 576, L25

Altay G., Theuns T., Schaye J., Crighton N. H. M., Dalla Vecchia C., 2011, ApJ, 737, L37

Anninos P., Norman M. L., Clarke D. A., 1994, ApJ, 436, 11

Arinyo-i-Prats A., Miralda-Escudé J., Viel M., Cen R., 2015, J. Cosmology Astropart. Phys., 12, 017

Bacon R., Accardo M., Adjali L., Anwand H., Bauer S., Biswas I., Blaizot J., Boudon D., Brau-Nogue S., Brinchmann J., Caillier P., Capoani L., Carollo C. M., Contini T., Couderc P., Daguisé E., Deiries S., Delabre B., Dreizler S., Dubois J., Dupieux M., Dupuy C., Emsellem E., Fechner T., Fleischmann A., François M., Gallou G., Gharsa T., Glindemann A., Gojak D., Guiderdoni B., Hansali G., Hahn T., Jarno A., Kelz A., Koehler C., Kosmalski J., Laurent F., Le Floch M., Lilly S. J., Lizon J.-L., Loupias M., Manescau A., Monstein C., Nicklas H., Olaya J.-C., Pares L., Pasquini L., Pécontal-Rousset A., Pelló R., Petit C., Popow E., Reiss R., Remillieux A., Renault E., Roth M., Rupprecht G., Serre D., Schaye J., Soucail G., Steinmetz M., Streicher O., Stuik R., Valentin H., Vernet J., Weilbacher P., Wisotzki L., Yerle N., 2010, in Proc. SPIE, Vol. 7735, Ground-based and Airborne Instrumentation for Astronomy III, p. 773508

Bahcall J. N., Bergeron J., Boksenberg A., Hartig G. F., Jannuzi B. T., Kirhakos S., Sargent W. L. W., Savage B. D. et al, 1993, ApJS, 87, 1

Bahcall N. A., Ostriker J. P., Perlmutter S., Steinhardt P. J., 1999, Science, 284, 1481

Ballinger W. E., Peacock J. A., Heavens A. F., 1996, MNRAS, 282, 877

Bardeen J. M., Bond J. R., Kaiser N., Szalay A. S., 1986a, ApJ, 304, 15

—, 1986b, ApJ, 304, 15

Barnes J., Hut P., 1986, Nature, 324, 446

Bautista J. E., Busca N. G., Guy J., Rich J., Blomqvist M., du Mas des Bourboux H., Pieri M. M., Font-Ribera A. et al, 2017, A&A, 603, A12

Becker G. D., Bolton J. S., Haehnelt M. G., Sargent W. L. W., 2011, MNRAS, 410, 1096

Becker G. D., Bolton J. S., Lidz A., 2015, Publ. Astron. Soc. Australia, 32, 045

Berger M. J., Oliger J., 1984, Journal of Computational Physics, 53, 484

Bergeron J., Petitjean P., Sargent W. L. W., Bahcall J. N., Boksenberg A., Hartig G. F., Jannuzi B. T., Kirhakos S. et al, 1994, ApJ, 436, 33

Blanton M., Cen R., Ostriker J. P., Strauss M. A., 1999, ApJ, 522, 590

Blumenthal G. R., Faber S. M., Flores R., Primack J. R., 1986, ApJ, 301, 27

Boera E., Murphy M. T., Becker G. D., Bolton J. S., 2016, MNRAS, 456, L79

Boksenberg A., Carswell R. F., Smith M. G., Whelan J. A. J., 1978, MNRAS, 184, 773

Bolton J. S., Becker G. D., Haehnelt M. G., Viel M., 2014, MNRAS, 438, 2499

Bolton J. S., Haehnelt M. G., 2007, MNRAS, 382, 325

Bordoloi R., Tumlinson J., Werk J. K., Oppenheimer B. D., Peeples M. S., Prochaska J. X., Tripp T. M., Katz N. et al, 2014, ApJ, 796, 136

Bouchet F. R., Kandrup H. E., 1985, ApJ, 299, 1

Bregman J. N., 2007, ARA&A, 45, 221

Bryan G. L., Norman M. L., O'Shea B. W., Abel T., Wise J. H., Turk M. J., Reynolds D. R., Collins D. C. et al, 2014, ApJS, 211, 19

Burles S., Nollett K. M., Turner M. S., 2001, Phys. Rev. D, 63, 063512

Busca N. G., Delubac T., Rich J., Bailey S., Font-Ribera A., Kirkby D., Le Goff J.-M., Pieri M. M. et al, 2013, A&A, 552, A96

Bustard C., Zweibel E. G., D'Onghia E., 2016, ApJ, 819, 29

Carswell R. F., Ferland G. J., 1980, MNRAS, 191, 55

Cen R., Chisari N. E., 2011, ApJ, 731, 11

Cen R., Miralda-Escudé J., Ostriker J. P., Rauch M., 1994, ApJ, 437, L9

Cen R., Ostriker J. P., 1999, ApJ, 514, 1

—, 2006, ApJ, 650, 560

Chen S.-F. S., Simcoe R. A., Torrey P., Bañados E., Cooksey K., Cooper T., Furesz G., Matejek M. et al, 2017, ApJ, 850, 188

Chisholm J., Matsushita S., 2016, ApJ, 830, 72

Chisholm J., Tremonti C. A., Leitherer C., Chen Y., 2017, MNRAS, 469, 4831

Chisholm J., Tremonti C. A., Leitherer C., Chen Y., Wofford A., Lundgren B., 2015, ApJ, 811, 149

Chisholm J., Tremonti Christy A., Leitherer C., Chen Y., 2016, MNRAS, 463, 541

Christensen C. R., Davé R., Governato F., Pontzen A., Brooks A., Munshi F., Quinn T., Wadsley J., 2016, ApJ, 824, 57

Clarke C., Carswell B., 2014, Principles of Astrophysical Fluid Dynamics

Clowe D., Bradač M., Gonzalez A. H., Markevitch M., Randall S. W., Jones C., Zaritsky D., 2006, ApJ, 648, L109

Clowe D., Gonzalez A., Markevitch M., 2004, ApJ, 604, 596

Colberg J. M., Krughoff K. S., Connolly A. J., 2005, MNRAS, 359, 272

Cole S., Benson A., Baugh C., Lacey C., Frenk C., 2000a, in Astronomical Society of the Pacific Conference Series, Vol. 200, Clustering at High Redshift, Mazure A., Le Fèvre O., Le Brun V., eds., p. 109

Cole S., Fisher K. B., Weinberg D. H., 1994, MNRAS, 267, 785

Cole S., Lacey C. G., Baugh C. M., Frenk C. S., 2000b, MNRAS, 319, 168

Cole S., Percival W. J., Peacock J. A., Norberg P., Baugh C. M., Frenk C. S., Baldry I., Bland-Hawthorn J. et al, 2005, MNRAS, 362, 505

Coles P., 1993, MNRAS, 262, 1065

Colless M., Dalton G., Maddox S., Sutherland W., Norberg P., Cole S., Bland-Hawthorn J., Bridges T. et al, 2001, MNRAS, 328, 1039

Colless M., Peterson B. A., Jackson C., Peacock J. A., Cole S., Norberg P., Baldry I. K., Baugh C. M. et al, 2003, ArXiv Astrophysics e-prints

Comparat J., Delubac T., Jouvel S., Raichoor A., Kneib J.-P., Yèche C., Abdalla F. B., Le Cras C. et al, 2016, A&A, 592, A121

Copi C. J., Schramm D. N., Turner M. S., 1995a, ApJ, 455, L95

—, 1995b, Science, 267, 192

Crain R. A., Schaye J., Bower R. G., Furlong M., Schaller M., Theuns T., Dalla Vecchia C., Frenk C. S. et al, 2015, MNRAS, 450, 1937

Creasey P., Theuns T., Bower R. G., 2013, MNRAS, 429, 1922

—, 2015, MNRAS, 446, 2125

Croft R. A. C., 2004, ApJ, 610, 642

Croft R. A. C., Weinberg D. H., Pettini M., Hernquist L., Katz N., 1999, ApJ, 520, 1

Dalla Vecchia C., Schaye J., 2008, MNRAS, 387, 1431

Danforth C. W., Shull J. M., 2008, ApJ, 679, 194

Davé R., Finlator K., Oppenheimer B. D., 2011a, MNRAS, 416, 1354

Davé R., Oppenheimer B. D., Finlator K., 2011b, MNRAS, 415, 11

de Bernardis P., Ade P. A. R., Bock J. J., Bond J. R., Borrill J., Boscaleri A., Coble K., Contaldi C. R. et al, 2002, ApJ, 564, 559

de Graaff A., Cai Y.-C., Heymans C., Peacock J. A., 2017, ArXiv e-prints

Dekel A., Silk J., 1986, ApJ, 303, 39

DESI Collaboration, Aghamousa A., Aguilar J., Ahlen S., Alam S., Allen L. E., Allende Prieto C., Annis J. et al, 2016, ArXiv e-prints

Desjacques V., Jeong D., Schmidt F., 2016, ArXiv e-prints

Díaz C. G., Ryan-Weber E. V., Cooke J., Koyama Y., Ouchi M., 2015, MNRAS, 448, 1240

Dobrzycki A., Bechtold J., Scott J., Morita M., 2002, ApJ, 571, 654

D'Odorico V., Cupani G., Cristiani S., Maiolino R., Molaro P., Nonino M., Centurión M., Cimatti A. et al, 2013, MNRAS, 435, 1198

Doux C., Schaan E., Aubourg E., Ganga K., Lee K.-G., Spergel D. N., Tréguer J., 2016, Phys. Rev. D, 94, 103506

Efstathiou G., 2000, MNRAS, 317, 697

Efstathiou G., Davis M., White S. D. M., Frenk C. S., 1985, ApJS, 57, 241

Erb D. K., 2015, Nature, 523, 169

Erb D. K., Steidel C. C., Shapley A. E., Pettini M., Reddy N. A., Adelberger K. L., 2006, ApJ, 646, 107

Faber S. M., Gallagher J. S., 1979, ARA&A, 17, 135

Finlator K., Davé R., 2008, MNRAS, 385, 2181

Font-Ribera A., Kirkby D., Busca N., Miralda-Escudé J., Ross N. P., Slosar A., Rich J., Aubourg É. et al, 2014, J. Cosmology Astropart. Phys., 5, 027

Fox A., Richter P., 2016, A&A, 588, A94

Fraternali F., 2017, in Astrophysics and Space Science Library, Vol. 430, Astrophysics and Space Science Library, Fox A., Davé R., eds., p. 323

Fry J. N., Gaztanaga E., 1993, ApJ, 413, 447

Fujita A., Martin C. L., Mac Low M.-M., New K. C. B., Weaver R., 2009, ApJ, 698, 693

Gao L., White S. D. M., Jenkins A., Frenk C. S., Springel V., 2005, MNRAS, 363, 379

Genzel R., Tacconi L. J., Gracia-Carpio J., Sternberg A., Cooper M. C., Shapiro K., Bolatto A., Bouché N. et al, 2010, MNRAS, 407, 2091

George R. D., Ivison R. J., Smail I., Swinbank A. M., Hopwood R., Stanley F., Swinyard B. M., Valtchanov I. et al, 2014, MNRAS, 442, 1877

Giallongo E., D'Odorico S., Fontana A., McMahon R. G., Savaglio S., Cristiani S., Molaro P., Trevese D., 1994, ApJ, 425, L1

Gingold R. A., Monaghan J. J., 1977, MNRAS, 181, 375

Giodini S., Pierini D., Finoguenov A., Pratt G. W., Boehringer H., Leauthaud A., Guzzo L., Aussel H. et al, 2009, ApJ, 703, 982

Gnedin N. Y., Hamilton A. J. S., 2002, MNRAS, 334, 107

Gontcho A Gontcho S., Miralda-Escudé J., Busca N. G., 2014, MNRAS, 442, 187

Governato F., Brook C., Mayer L., Brooks A., Rhee G., Wadsley J., Jonsson P., Willman B. et al, 2010, Nature, 463, 203

Greig B., Bolton J. S., Wyithe J. S. B., 2015, MNRAS, 447, 2503

Gunn J. E., Peterson B. A., 1965, ApJ, 142, 1633

Gurvich A., Burkhart B., Bird S., 2017, ApJ, 835, 175

Haardt F., Madau P., 1996, ApJ, 461, 20

—, 2012, ApJ, 746, 125

Haehnelt M. G., Madau P., Kudritzki R., Haardt F., 2001, ApJ, 549, L151

Hamilton A. J. S., 1998, in Astrophysics and Space Science Library, Vol. 231, The Evolving Universe, Hamilton D., ed., p. 185

Heckman T. M., Borthakur S., Overzier R., Kauffmann G., Basu-Zych A., Leitherer C., Sembach K., Martin D. C. et al, 2011, ApJ, 730, 5

Heckman T. M., Thompson T. A., 2017, ArXiv e-prints

Hernquist L., Katz N., 1989, ApJS, 70, 419

Hirata C. M., 2017, ArXiv e-prints

Hopkins P. F., Kereš D., Oñorbe J., Faucher-Giguère C.-A., Quataert E., Murray N., Bullock J. S., 2014, MNRAS, 445, 581

Hopkins P. F., Quataert E., Murray N., 2011, MNRAS, 417, 950

—, 2012, MNRAS, 421, 3522

Hoyle F., Tayler R. J., 1964, Nature, 203, 1108

Hu E. M., Kim T.-S., Cowie L. L., Songaila A., Rauch M., 1995, AJ, 110, 1526

Hu W., Dodelson S., 2002, ARA&A, 40, 171

Hu W., Eisenstein D. J., Tegmark M., White M., 1999, Phys. Rev. D, 59, 023512

Hui L., Gnedin N. Y., Zhang Y., 1997, ApJ, 486, 599

Iliev I. T., Scannapieco E., Martel H., Shapiro P. R., 2003, MNRAS, 341, 81

Iršič V., Viel M., Haehnelt M. G., Bolton J. S., Cristiani S., Becker G. D., D'Odorico V., Cupani G. et al, 2017, Phys. Rev. D, 96, 023522

Jannuzi B. T., Bahcall J. N., Bergeron J., Boksenberg A., Hartig G. F., Kirhakos S., Sargent W. L. W., Savage B. D. et al, 1998, ApJS, 118, 1

Jose C., Lacey C. G., Baugh C. M., 2016, MNRAS, 463, 270

Kaiser N., 1987, MNRAS, 227, 1

Kang H., Ryu D., Cen R., Song D., 2005, ApJ, 620, 21

Kaplinghat M., Turner M. S., 2001, Physical Review Letters, 86, 385

Katz N., Weinberg D. H., Hernquist L., 1996, ApJS, 105, 19

Keller B. W., Wadsley J., Benincasa S. M., Couchman H. M. P., 2014, MNRAS, 442, 3013

Keller B. W., Wadsley J., Couchman H. M. P., 2015, MNRAS, 453, 3499

Kim T.-S., Carswell R. F., Cristiani S., D'Odorico S., Giallongo E., 2002, MNRAS, 335, 555

Kim T.-S., Cristiani S., D'Odorico S., 2001, A&A, 373, 757

Kim T.-S., Hu E. M., Cowie L. L., Songaila A., 1997, AJ, 114, 1

Kimm T., Cen R., Devriendt J., Dubois Y., Slyz A., 2015, MNRAS, 451, 2900

Kobayashi C., 2004, MNRAS, 347, 740

Kollmeier J. A., Weinberg D. H., Oppenheimer B. D., Haardt F., Katz N., Davé R., Fardal M., Madau P. et al, 2014, ApJ, 789, L32

Krause M., Diehl R., Böhringer H., Freyberg M., Lubos D., 2014, A&A, 566, A94

Lara J. F., 2005, Phys. Rev. D, 72, 023509

Le Bret T., Pontzen A., Cooper A. P., Frenk C., Zolotov A., Brooks A. M., Governato F., Parry O. H., 2015, ArXiv e-prints

Lee K.-G., Suzuki N., Spergel D. N., 2012, AJ, 143, 51

Lehnert M. D., Heckman T. M., Weaver K. A., 1999, ApJ, 523, 575

Leroy A. K., Walter F., Brinks E., Bigiel F., de Blok W. J. G., Madore B., Thornley M. D., 2008, AJ, 136, 2782

Leroy A. K., Walter F., Martini P., Roussel H., Sandstrom K., Ott J., Weiss A., Bolatto A. D. et al, 2015, ApJ, 814, 83

Lumsden S. L., Heavens A. F., Peacock J. A., 1989, MNRAS, 238, 293

Lyman T., 1906, ApJ, 23, 181

Lynds R., 1971, ApJ, 164, L73

Mac Low M.-M., Ferrara A., 1999, ApJ, 513, 142

Macciò A. V., Dutton A. A., van den Bosch F. C., Moore B., Potter D., Stadel J., 2007, MNRAS, 378, 55

Machacek M. E., Bryan G. L., Meiksin A., Anninos P., Thayer D., Norman M., Zhang Y., 2000, ApJ, 532, 118

Madau P., Haardt F., Rees M. J., 1999, ApJ, 514, 648

Mannucci F., Cresci G., Maiolino R., Marconi A., Gnerucci A., 2010, MNRAS, 408, 2115

Mannucci F., Cresci G., Maiolino R., Marconi A., Pastorini G., Pozzetti L., Gnerucci A., Risaliti G. et al, 2009, MNRAS, 398, 1915

Martin C. L., 1999, ApJ, 513, 156

—, 2005, ApJ, 621, 227

Martin C. L., Dijkstra M., Henry A., Soto K. T., Danforth C. W., Wong J., 2015, ApJ, 803, 6

Martin C. L., Shapley A. E., Coil A. L., Kornei K. A., Bundy K., Weiner B. J., Noeske K. G., Schiminovich D., 2012, ApJ, 760, 127

Maselli A., Ferrara A., 2005, MNRAS, 364, 1429

McCarthy I. G., Bower R. G., Balogh M. L., 2007, MNRAS, 377, 1457

McDonald P., 2003, ApJ, 585, 34

—, 2006, Phys. Rev. D, 74, 103512

McDonald P., Seljak U., Burles S., Schlegel D. J., Weinberg D. H., Cen R., Shih D., Schaye J. et al, 2006, ApJS, 163, 80

McDonald P., Seljak U., Cen R., Bode P., Ostriker J. P., 2005, MNRAS, 360, 1471

McQuinn M., 2016, ARA&A, 54, 313

McQuinn M., Hernquist L., Lidz A., Zaldarriaga M., 2011, MNRAS, 415, 977

Meiksin A., Bolton J. S., Tittley E. R., 2014, MNRAS, 445, 2462

Meiksin A., White M., 2004, MNRAS, 350, 1107

Mihos C., Hernquist L., 1994, ArXiv Astrophysics e-prints

Mo H., van den Bosch F. C., White S., 2010, Galaxy Formation and Evolution

Murray N., Quataert E., Thompson T. A., 2005, ApJ, 618, 569

Nasir F., Bolton J. S., Becker G. D., 2016, MNRAS, 463, 2335

Nasir F., Bolton J. S., Viel M., Kim T.-S., Haehnelt M. G., Puchwein E., Sijacki D., 2017, MNRAS, 471, 1056

Navarro J. F., Frenk C. S., White S. D. M., 1996, ApJ, 462, 563

Nelson D., Pillepich A., Genel S., Vogelsberger M., Springel V., Torrey P., Rodriguez-Gomez V., Sijacki D. et al, 2015, Astronomy and Computing, 13, 12

Nesvadba N. P. H., Lehnert M. D., De Breuck C., Gilbert A. M., van Breugel W., 2008, A&A, 491, 407

Netterfield C. B., Ade P. A. R., Bock J. J., Bond J. R., Borrill J., Boscaleri A., Coble K., Contaldi C. R. et al, 2002, ApJ, 571, 604

Nielsen N. M., Churchill C. W., Kacprzak G. G., Murphy M. T., 2013, ApJ, 776, 114

Norman M. L., Paschos P., Harkness R., 2009, in Journal of Physics Conference Series, Vol. 180, Journal of Physics Conference Series, p. 012021

Noterdaeme P., Petitjean P., Ledoux C., Srianand R., 2009, A&A, 505, 1087

Oñorbe J., Boylan-Kolchin M., Bullock J. S., Hopkins P. F., Kereš D., Faucher-Giguère C.-A., Quataert E., Murray N., 2015, MNRAS, 454, 2092

O'Meara J. M., Prochaska J. X., Burles S., Prochter G., Bernstein R. A., Burgess K. M., 2007, ApJ, 656, 666

Oppenheimer B. D., Davé R., 2006, MNRAS, 373, 1265

—, 2008, MNRAS, 387, 577

Oppenheimer B. D., Davé R., Kereš D., Fardal M., Katz N., Kollmeier J. A., Weinberg D. H., 2010, MNRAS, 406, 2325

Palanque-Delabrouille N., Yèche C., Baur J., Magneville C., Rossi G., Lesgourgues J., Borde A., Burtin E. et al, 2015, J. Cosmology Astropart. Phys., 11, 011

Parrish I. J., Quataert E., Sharma P., 2009, ApJ, 703, 96

Peebles P. J. E., 1980, The large-scale structure of the universe

Peeples M. S., Werk J. K., Tumlinson J., Oppenheimer B. D., Prochaska J. X., Katz N., Weinberg D. H., 2014, ApJ, 786, 54

Penton S. V., Stocke J. T., Shull J. M., 2004, ApJS, 152, 29

Percival W. J., Burkey D., Heavens A., Taylor A., Cole S., Peacock J. A., Baugh C. M., Bland-Hawthorn J. et al, 2004, MNRAS, 353, 1201

Perlmutter S. A., Deustua S., Gabi S., Goldhaber G., Groom D., Hook I., Kim A., Kim M., Lee J., Pain R., Pennypacker C., Small I., Goobar A., Ellis R., Mcmahon R., Boyle B., Bunclark P., Carter D., Glazebrook K., Irwin M., Newberg H., Filippenko A. V., Matheson T., Dopita M., Mould J., Couch W., 1997, in NATO Advanced Science Institutes (ASI) Series C, Vol. 486, NATO Advanced Science Institutes (ASI) Series C, Ruiz-Lapuente P., Canal R., Isern J., eds., p. 749

Péroux C., Dessauges-Zavadsky M., D'Odorico S., Sun Kim T., McMahon R. G., 2005, MNRAS, 363, 479

Pieri M. M., Bonoli S., Chaves-Montero J., Pâris I., Fumagalli M., Bolton J. S., Viel M., Noterdaeme P., Miralda-Escudé J., Busca N. G., Rahmani H., Peroux C., Font-Ribera A., Trager S. C., 2016, in SF2A-2016: Proceedings of the Annual meeting of the French Society of Astronomy and Astrophysics, Reylé C., Richard J., Cambrésy L., Deleuil M., Pécontal E., Tresse L., Vauglin I., eds., pp. 259–266

Planck Collaboration, Ade P. A. R., Aghanim N., Arnaud M., Arroja F., Ashdown M., Aumont J., Baccigalupi C. et al, 2016a, A&A, 594, A20

Planck Collaboration, Ade P. A. R., Aghanim N., Arnaud M., Ashdown M., Aumont J., Baccigalupi C., Banday A. J. et al, 2016b, A&A, 594, A13

Pontzen A., 2014, Phys. Rev. D, 89, 083010

Pontzen A., Bird S., Peiris H., Verde L., 2014, ApJ, 792, L34

Pontzen A., Governato F., 2012, MNRAS, 421, 3464

—, 2014, Nature, 506, 171

Pontzen A., Read J. I., Teyssier R., Governato F., Gualandris A., Roth N., Devriendt J., 2015, MNRAS, 451, 1366

Prochaska J. X., Kasen D., Rubin K., 2011, ApJ, 734, 24

Prochaska J. X., O'Meara J. M., Worseck G., 2010, ApJ, 718, 392

Prochaska J. X., Weiner B. J., Chen H.-W., Mulchaey J. S., 2006, ApJ, 643, 680

Quilis V., Bower R. G., Balogh M. L., 2001, MNRAS, 328, 1091

Rauch M., 1998, ARA&A, 36, 267

Rauch M., Haehnelt M. G., Steinmetz M., 1997, ApJ, 481, 601

Recchi S., Hensler G., 2013, A&A, 551, A41

Rees M., 1997, Nature, 385, 786

Rees M. J., Ostriker J. P., 1977, MNRAS, 179, 541

Richardson M. L. A., Scannapieco E., Devriendt J., Slyz A., Thacker R. J., Dubois Y., Wurster J., Silk J., 2016, ApJ, 825, 83

Rorai A., Becker G. D., Haehnelt M. G., Carswell R. F., Bolton J. S., Cristiani S., D'Odorico V., Cupani G. et al, 2017, MNRAS, 466, 2690

Rorai A., Hennawi J. F., White M., 2013, ApJ, 775, 81

Rubin K. H. R., Prochaska J. X., Koo D. C., Phillips A. C., 2012, ApJ, 747, L26

Rubin K. H. R., Weiner B. J., Koo D. C., Martin C. L., Prochaska J. X., Coil A. L., Newman J. A., 2010, ApJ, 719, 1503

Rubin V. C., Thonnard N. T., Ford Jr. W. K., 1982, AJ, 87, 477

Rudie G. C., Steidel C. C., Trainor R. F., Rakic O., Bogosavljević M., Pettini M., Reddy N., Shapley A. E. et al, 2012, ApJ, 750, 67

Rupke D. S., Veilleux S., Sanders D. B., 2005, ApJS, 160, 115

Sakai S., Madore B. F., 1999, ApJ, 526, 599

Sargent W. L. W., Young P. J., Boksenberg A., Tytler D., 1980, ApJS, 42, 41

Scannapieco C., Tissera P. B., White S. D. M., Springel V., 2005, MNRAS, 364, 552

Scannapieco C., Wadepuhl M., Parry O. H., Navarro J. F., Jenkins A., Springel V., Teyssier R., Carlson E. et al, 2012, MNRAS, 423, 1726

Scannapieco E., Brüggen M., 2010, MNRAS, 405, 1634

—, 2015, ApJ, 805, 158

Schaye J., Crain R. A., Bower R. G., Furlong M., Schaller M., Theuns T., Dalla Vecchia C., Frenk C. S. et al, 2015, MNRAS, 446, 521

Scoccimarro R., 2004, Phys. Rev. D, 70, 083007

Scott J., Bechtold J., Dobrzycki A., Kulkarni V. P., 2000, ApJS, 130, 67

Seljak U., 2012, J. Cosmology Astropart. Phys., 3, 004

Sell P. H., Tremonti C. A., Hickox R. C., Diamond-Stanic A. M., Moustakas J., Coil A., Williams A., Rudnick G. et al, 2014, MNRAS, 441, 3417

Shopbell P. L., Bland-Hawthorn J., 1998, ApJ, 493, 129

Shull J. M., 2003, in Astrophysics and Space Science Library, Vol. 281, The IGM/Galaxy Connection. The Distribution of Baryons at z=0, Rosenberg J. L., Putman M. E., eds., p. 1

Shull J. M., Smith B. D., Danforth C. W., 2012, ApJ, 759, 23

Sijacki D., Vogelsberger M., Genel S., Springel V., Torrey P., Snyder G. F., Nelson D., Hernquist L., 2015, MNRAS, 452, 575

Simcoe R. A., 2006, ApJ, 653, 977

Singh V., Lahiri J., Bhowmick D., Basu D. N., 2017, ArXiv e-prints

Slosar A., Font-Ribera A., Pieri M. M., Rich J., Le Goff J.-M., Aubourg É., Brinkmann J., Busca N. et al, 2011, J. Cosmology Astropart. Phys., 9, 001

Slosar A., Ho S., White M., Louis T., 2009, J. Cosmology Astropart. Phys., 10, 019

Somerville R. S., Davé R., 2015, ARA&A, 53, 51

Spergel D. N., Bean R., Doré O., Nolta M. R., Bennett C. L., Dunkley J., Hinshaw G., Jarosik N. et al, 2007, ApJS, 170, 377

Springel V., 2005, MNRAS, 364, 1105

—, 2010, MNRAS, 401, 791

Springel V., Di Matteo T., Hernquist L., 2005, MNRAS, 361, 776

Springel V., Frenk C. S., White S. D. M., 2006, Nature, 440, 1137

Springel V., Hernquist L., 2003, MNRAS, 339, 289

Steidel C. C., Erb D. K., Shapley A. E., Pettini M., Reddy N., Bogosavljević M., Rudie G. C., Rakic O., 2010, ApJ, 717, 289

Stewart K. R., Kaufmann T., Bullock J. S., Barton E. J., Maller A. H., Diemand J., Wadsley J., 2011, ApJ, 738, 39

Stiavelli M., 2007, ArXiv e-prints

Stoughton C., Lupton R. H., Bernardi M., Blanton M. R., Burles S., Castander F. J., Connolly A. J., Eisenstein D. J. et al, 2002, AJ, 123, 485

Strickland D., 2002, in Astronomical Society of the Pacific Conference Series, Vol. 253, Chemical Enrichment of Intracluster and Intergalactic Medium, Fusco-Femiano R., Matteucci F., eds., p. 387

Strickland D. K., Heckman T. M., 2009, ApJ, 697, 2030

Strickland D. K., Heckman T. M., Colbert E. J. M., Hoopes C. G., Weaver K. A., 2004, ApJS, 151, 193

Strickland D. K., Stevens I. R., 2000, MNRAS, 314, 511

Suarez T., Pontzen A., 2017, MNRAS, 472, 2643

Suarez T., Pontzen A., Peiris H. V., Slyz A., Devriendt J., 2016, MNRAS, 462, 994

Suginohara T., Suto Y., 1991, ApJ, 371, 470

Sunyaev R. A., Zeldovich I. B., 1980, ARA&A, 18, 537

Sur S., Scannapieco E., Ostriker E. C., 2016, ApJ, 818, 28

Tanimura H., Hinshaw G., McCarthy I. G., Van Waerbeke L., Ma Y.-Z., Mead A., Hojjati A., Tröster T., 2017, ArXiv e-prints

Tegmark M., Strauss M. A., Blanton M. R., Abazajian K., Dodelson S., Sandvik H., Wang X., Weinberg D. H. et al, 2004, Phys. Rev. D, 69, 103501

Teyssier R., 2002, A&A, 385, 337

Theuns T., Leonard A., Efstathiou G., Pearce F. R., Thomas P. A., 1998, MNRAS, 301, 478

Theuns T., Zaroubi S., Kim T.-S., 2001, ArXiv Astrophysics e-prints

Thompson T. A., Quataert E., Zhang D., Weinberg D. H., 2016, MNRAS, 455, 1830

Toro E. F., Spruce M., Speares W., 1994, Shock Waves, 4, 25

Torrey P., Snyder G. F., Vogelsberger M., Hayward C. C., Genel S., Sijacki D., Springel V., Hernquist L. et al, 2015, MNRAS, 447, 2753

Torrey P., Vogelsberger M., Genel S., Sijacki D., Springel V., Hernquist L., 2014, MNRAS, 438, 1985

Trainor R., Steidel C. C., 2013, ApJ, 775, L3

Tumlinson J., Thom C., Werk J. K., Prochaska J. X., Tripp T. M., Katz N., Davé R., Oppenheimer B. D. et al, 2013, ApJ, 777, 59

Tumlinson J., Thom C., Werk J. K., Prochaska J. X., Tripp T. M., Weinberg D. H., Peeples M. S., O'Meara J. M. et al, 2011, Science, 334, 948

Turner M. S., 1991, Physica Scripta Volume T, 36, 167

—, 2002, ApJ, 576, L101

van de Voort F., Schaye J., Booth C. M., Dalla Vecchia C., 2011a, MNRAS, 415, 2782

van de Voort F., Schaye J., Booth C. M., Haas M. R., Dalla Vecchia C., 2011b, MNRAS, 414, 2458

Varshalovich D. A., Moskalev A. N., Khersonskii V. K., 1988, Quantum Theory of Angular Momentum. World Scientific Publishing Co

Veilleux S., Cecil G., Bland-Hawthorn J., 2005, ARA&A, 43, 769

Viel M., Becker G. D., Bolton J. S., Haehnelt M. G., 2013, Phys. Rev. D, 88, 043502

Viel M., Lesgourgues J., Haehnelt M. G., Matarrese S., Riotto A., 2005, Phys. Rev. D, 71, 063534

Viel M., Matarrese S., Mo H. J., Theuns T., Haehnelt M. G., 2002, MNRAS, 336, 685

Viel M., Matarrese S., Theuns T., Munshi D., Wang Y., 2003, MNRAS, 340, L47

Vogelsberger M., Genel S., Springel V., Torrey P., Sijacki D., Xu D., Snyder G., Nelson D. et al, 2014, MNRAS, 444, 1518

Vogt S. S., Allen S. L., Bigelow B. C., Bresee L., Brown B., Cantrall T., Conrad A., Couture M., Delaney C., Epps H. W., Hilyard D., Hilyard D. F., Horn E., Jern N., Kanto D., Keane M. J., Kibrick R. I., Lewis J. W., Osborne J., Pardeilhan G. H., Pfister T., Ricketts T., Robinson L. B., Stover R. J., Tucker D., Ward J., Wei M. Z., 1994, in Proc. SPIE, Vol. 2198, Instrumentation in Astronomy VIII, Crawford D. L., Craine E. R., eds., p. 362

von Glasow W., Krause M. G. H., Sommer-Larsen J., Burkert A., 2013, MNRAS, 434, 1151

Walter F., Weiss A., Scoville N., 2002, ApJ, 580, L21

Walther M., Hennawi J., Hiss H., Oñorbe J., Lee K.-G., Rorai A., O'Meara J. M. J., 2018, ApJ, 852, 22

Weinberg D. H., Hernquist L., Katz N., 1997, ApJ, 477, 8

Weinberg S., 2008, Cosmology. Oxford University Press

Werk J. K., Prochaska J. X., Thom C., Tumlinson J., Tripp T. M., O'Meara J. M., Peeples M. S., 2013, ApJS, 204, 17

Werk J. K., Prochaska J. X., Tumlinson J., Peeples M. S., Tripp T. M., Fox A. J., Lehner N., Thom C. et al, 2014, ApJ, 792, 8

Weymann R. J., Carswell R. F., Smith M. G., 1981, ARA&A, 19, 41

White M., Pope A., Carlson J., Heitmann K., Habib S., Fasel P., Daniel D., Lukic Z., 2010, ApJ, 713, 383

Wiersma R. P. C., Schaye J., Theuns T., Dalla Vecchia C., Tornatore L., 2009, MNRAS, 399, 574

Wolfe A. M., Turnshek D. A., Lanzetta K. M., Lu L., 1993, ApJ, 404, 480

Yun M. S., Ho P. T. P., Lo K. Y., 1993, ApJ, 411, L17

Zaldarriaga M., Scoccimarro R., Hui L., 2003, ApJ, 590, 1

Zaldarriaga M., Seljak U., Hui L., 2001, ApJ, 551, 48

Zhang D., Thompson T. A., Murray N., Quataert E., 2014, ApJ, 784, 93

Zhang D., Thompson T. A., Quataert E., Murray N., 2017, MNRAS, 468, 4801